Fall 2018

# Diamond Intracrystalline Stable Isotope Chemical Image Analysis by Time-of-Flight Secondary Ionization Mass Spectrometery

Tyler J. Sundell
*Missouri State University*, Sundell127@live.missouristate.edu

# DIAMOND INTRACRYSTALLINE STABLE ISOTOPE CHEMICAL IMAGE ANALYSIS BY TIME-OF-FLIGHT SECONDARY IONIZATION MASS SPECTROMETERY

A Master's Thesis

Presented to

The Graduate College of

Missouri State University

In Partial Fulfillment

Of the Requirements for the Degree

Master of Science, Geospatial Sciences

By

Tyler James Sundell

December 2018

**DIAMOND INTRACRYSTALLINE STABLE ISOTOPE CHEMICAL IMAGE ANALYSIS BY TIME-OF-FLIGHT SECONDARY IONIZATION MASS SPECTROMETERY**

Geography, Geology, and Planning

Missouri State University, December 2018

Master of Science

Tyler James Sundell

## ABSTRACT

The chemical resistance of diamond allows in-situ study of the diamond source regions. For a majority of gem quality diamonds, this source region is the sublithospheric mantle keel of a cratonic nuclei. Through analysis of stable isotopes, radiogenic isotopes and trace elements, diamond geochemical analyses can define chemical fluxes in the mantle keel. However, such studies require multiple methodologies for each chemical suite, high spatial resolution and analytical precision. Here, I evaluate Time-of-Flight Secondary Ionization Mass Spectrometer (ToF-SIMS) as an alternative method for diamond geochemical analyses. ToF-SIMS analysis can perform in cation and anion mode to measure the entire periodic table of an analyte. Establishing a quantitative ToF-SIMS methodology would dramatically increase the accessibility of diamond geochemical analyses. I determine the feasibility of developing such a ToF-SIMS diamond geochemical methodology. For ToF-SIMS to be considered a plausible method, ToF-SIMS needs to replicate established instrumentation spatial resolution and analytical precision. I determine that ToF-SIMS is able to replicate established spatial resolutions with single pixels in our element maps being $< 2$ $\mu m^2$.Through measurements of $^{13}C$ and $^{12}C$, I show that ToF-SIMS is unable to replicate the analytical precision necessary for $\delta^{13}C$ values. I conclude by establishing a framework for future ToF-SIMS studies to the end of obtaining the necessary analytical precision for quantifying isotopic variation and improved mass resolution.

**KEYWORDS**: method development, chemical image analysis, ToF-SIMS, diamond geochemistry, stable isotope geochemistry

**DIAMOND INTRACRYSTALLINE STABLE ISOTOPE CHEMICAL IMAGE ANALYSIS BY TIME-OF-FLIGHT SECONDARY IONIZATION MASS SPECTROMETERY**

By

Tyler James Sundell

A Master's Thesis
Submitted to the Graduate College
Of Missouri State University
In Partial Fulfillment of the Requirements
For the Degree of Master of Science, Geospatial Science

December 2018

Approved:

Gary Michelfelder, Ph.D., Thesis Committee Chair

Kevin Mickus, Ph.D., Committee Member

Melida Gutierrez, Ph.D., Committee Member

Julie Masterson, Ph.D., Dean of the Graduate College

## TABLE OF CONTENTS

## LIST OF TABLES

## LIST OF FIGURES

# INTRODUCTION

Diamond chemical and thermodynamic stability make them an ideal mineral to study the interior of the Earth including the sublithospheric mantle and deep mantle (<660 km; Stachel et al., 2000a; 2000b). Through diamond inclusion and chemical variability, insight into the pressure, temperature, timescale and chemical (P-T-t-X) changes in the sublithospheric mantle and mantle are elucidated (Kaminsky et al., 2009; Palot et al., 2009; Sobolev et al., 2009). Over the past 30 years geochemical study of diamonds and their inclusions have constrained the temporal evolution of the lithosphere and mantle, but these studies face a series of difficulties (Shirey et al., 2002). Diamond host rocks such as kimberlites and lamproites usually contain mixed populations of diamond each with a unique P-T-t-X history. These histories include diamonds traveling through hundreds of kilometers of the mantle, exposer to extreme chemical environments of kimberlite magmas and metastability for millions to billions of years at surface conditions or residence within the mantle. Of all gem quality diamonds, an estimated 80% go through these trials and crystallize within the Diamond Stability Field (DSF) from 120 to 260 km depth (Harte, 2010). Within the DSF, carbon super saturation occurs in metasomatic fluids causing crystallization of diamond in interstitial grain boundaries from highly incompatible mantle fluids (Shirey and Shigley, 2013; Logvinova et al., 2015). Thus, models and constraints of diamond genesis and evolution require focused studies of different populations to characterize and constrain growth conditions (Thomassot et al., 2007).

Analysis of stable and radiogenic isotope ratios and trace element concentrations within diamonds, fluid inclusions, mineral inclusions, or elemental impurities allow for the constraint of diamond evolution and classification of diamond populations. Diamond growth zones record

equilibrium conditions of mantle fluids as growth, residence, and exhumation occur. Analysis of multiple growth zones within diamond allows the measurement of fluxes within mantle fluids. Whereas mantle xenoliths are exposed to open system mantle melting and subject to metasomatism and local-scale re-equilibration during mantle residence as well as alteration during and after kimberlite eruption (Viljoen et al., 2004). Diamond growth zones and inclusions remain closed with negligible diffusion between the host magma and diamond. Therefore, characterization of fluid sources and the history of diamonds can be determined by studies of growth zones, inclusions and multiple generations of inclusions. Such studies provide insight into the evolutionary history of cratons (Cartigny et al., 2009; Richardson et al., 2009; Stachel et al., 2009; Timmerman et al., 2017).

Radiogenic isotope studies are primarily restricted to inclusions and are relatively straight forward. Stable isotope studies of host diamond growth zones, however, require high analytical precision and minimal destruction of the sample. The precision and accuracy required for high spatial resolution studies have only recently been established. Prior isotopic studies of diamonds required destruction of the sample through whole combustion of fractured diamond shards within a pure oxygen environment (Deines et al., 1984; McCandless et al., 1991). Current methodologies include Secondary Ionization Mass Spectrometry (SIMS) for carbon isotope values and laser ablation inductively coupled plasma mass spectrometry (LA-ICP-MS) or Electron Microprobe for trace element concentrations (Kaminsky et al., 2015; Van Rythoven, 2012). Each of these methods have spot sizes and ablation pits on the order of tens of micrometers in diameter with minimal sample destruction. With the development of these methodologies, questions such as what role does subduction play in the carbon cycle or how carbon reservoirs have changed in the mantle through time are possible to address.

The primary issue with the instruments mentioned above are the cost and limited access to facilities. This study explores the viability of Time-of-Flight SIMS (ToF-SIMS) for measuring intracrystalline stable isotope variability of carbon within diamonds. ToF-SIMS is a useful method for in situ microanalysis of solids because of the spatial resolution, low detection limits and rapid analysis time compared to dissolution methods. During analysis a wide range of elements can be measured including carbon, oxygen, nitrogen and various cations while not requiring elaborate sample preparation or destroying the sample.

Calculation of stable isotope values from ToF-SIMS analysis compares the diamond composition to the composition of carbon based multi-element internal standards of carbonatite hosted calcite crystals. Such an approach is needed for analytical modeling of the ToF-SIMS data. The outcome of this project is to establish a frame work for a potential methodology for diamond analysis that is relatively cost effective while maintaining the spatial precision of more costly methods. As well as characterizing the stable isotope values of carbon and oxygen in the Magnetite Cove carbonatite.

## BACKGROUND

Diamond crystallization can occur at any depth on Earth. Meteorite impacts have been known to produce micro-diamonds in carbon-rich strata (Popigai Crater, Russia - Koeberl et al., 1997), ultrahigh pressure metamorphic belts have produced sub-gem to gem quality diamonds within the shallow to mid lithosphere (Kokchetav Massif, Kazakhstan - Schertl and Sobolev, 2013) and diamond crystallization from fluids can theoretically occur from 120 km to the core (Bundy, 1989). The latter population of diamonds is volumetrically the largest and the primary source of active mines. Independent of the crystallization environment, once diamonds form, they are indefinitely metastable at surface conditions or within the DSF.

Diamonds are subdivided based on mineral inclusions rather than chemistry or host deposit. Peridotitic (P-type) and eclogitic (E-type) diamonds refer to the type of mineral inclusions found within the stones (Harte, 2010). Ultra-deep (U-type) diamond types have been identified with mineral inclusions such as perovskite or carbides (Stachel et al., 2005). Sulfide inclusions have been observed in all diamond types. P-type show silica undersaturated inclusions such as olivine, ringwoodite, and wadsleyite. While E-type stones are silica enriched with inclusions such as clinopyroxene and majorite garnet. Diamond type is associated with the contiguous mantle rock that diamonds crystallize within. P-type reflect diamonds growing in relation to depleted mantle residue within the diamond stability field (DSF) and E-type diamonds grow in relation to subducted oceanic crust (Walter et al., 2011). P and E-type diamonds can mutually occur within the DSF.

The bonding structure of diamond restricts substitution of most elements on the periodic table. Nitrogen and boron are the only elements that significantly substitute carbon in the

diamond lattice. Of these elements, nitrogen is the only element that has been studied in detail. However, in rare blue diamonds, boron concentrations have been measured in the hundreds of parts per million (ppm) (Eaton-Magaña et al., 2018). Nitrogen content in ppm is the only criteria used to subdivide diamonds by chemistry into Type I and Type II diamonds. Type I diamonds have $N \geq 20$ ppm and Type II diamonds have $N < 20$ ppm (Shirey et al., 2013). Type I diamonds are the most common for mantle derived diamonds (Cartigny et al., 2009). Diamonds crystallized within kimberlite melts or in metamorphic environments commonly have high N concentrations $\geq 200$ ppm (Cartigny, 2005). Concentration of nitrogen in the diamond lattice is dependent on temperature, residence time and fluids crystallizing diamonds (Cartigny, 2005; Koga et al., 2003). Nitrogen impurities can diffuse in the lattice and form aggregation states aA, aB, and b. In type IaA diamonds, the nitrogen is present in concentrations $\geq 20$ ppm as paired atoms. Type IaB diamonds, the nitrogen is present in concentrations $\geq 20$ ppm as clusters of four atoms. Type Ib diamonds, the nitrogen is present in concentrations $\geq 20$ ppm as single atoms. Nitrogen aggregation state is measured via Fourier-transform Infrared Spectroscopy (FTIR) and presented as a percent between states. For example, a type I diamond may have an aggregation state as 30% aA. Where 30% of nitrogen present in the structure are pairs of nitrogen. Aggregation state has been suggested as a measure of residence time within the mantle (Shirey et al., 2013). With Type Ib diamonds being under mantle conditions for shorter periods of time and IaB being the longest. However, the diffusivity of nitrogen within the structure changes as higher order aggregations occur and the kinetics of aggregation slow considerably at higher states (Koga et al., 2003).

**Mineral Properties**

This study focuses on diamonds crystallized or which resided within a sublithospheric mantle keel. Pressure and temperature conditions of these environments often surpass the minimum crystallization conditions for diamond at 2 GPa and 1100 K (Bundy, 1989). Crystallization within high temperature and pressure regimes and subsequent relaxation during residence and exhumation demonstrate the unique robust nature of the diamond mineral lattice.

The mineral is a face-centered cubic crystal with tetrahedral bonds. The most common crystal habit of diamond is octahedral or cubic. Resorption during transit within kimberlitic magma may form more complicated habits such as rhombicosidodecahedron or a rounding of octahedral habit. Within kimberlitic magma crystallization of diamond in the form of fibrous coatings may also occur. Natural diamonds that have experienced chemical etching during kimberlitic eruption show trigons.

Carbon bonds in tetrahedral coordination with four adjacent carbon atoms with the ideal bond angle for C-C-C of 109.5°. These carbon atoms have hybridized $sp^3$ orbitals with covalent bond lengths of 1.5 Å (Hazen et al., 2013). The combination of carbon atoms in diamond having the ideal bond angle and hybridized electron exchange in the covalent bond allows for the extreme refractory capacity and stability/metastability in multiple chemical environments (Cherniak, 2010). Diffusivity of carbon within the diamond structure is also among the lowest diffusivities modeled (Koga et al., 2003). Koga et al. (2003) modeled heterogeneity of carbon isotopes between growth zones as preserved at 1.6 μm wavelength after one billion years of 1300 to 1400 K. These properties explain why diamond is the premier target for in situ mantle chemistry studies. The resistance characteristic of diamond means that the chemical bonds in the lattice or impurities and inclusions remain in a closed system during residence, exhumation, and surface exposure. While migration of atoms within these structures is minimal.

**Residence and Exhumation**

While most diamondiferous mines target gems originating within the mantle, diamonds must be transported to the base of the lithosphere and reside there for millions of years before exhumation (Helmstaedt, 1993; Stern et al., 2016). At the base of the lithosphere, diamonds reside within the mantle keel attached to the crust. Within the mantle keel, diamond residence is firmly within the DSF and diamonds exist at an indefinite state of equilibrium (Hazen et al., 2013). However, within the lattice, nitrogen migration into different aggregation states and diffusivity between growth zones occurs. As such, diamonds crystalized at greater depth will have lower resolution of growth zones and may transition from type I to II due to the increase in diffusivity of carbon and nitrogen loss as time under temperature increases (Koga et al., 2003). Once diamond is exhumed from the DSF, the lattice exists indefinitely as a metastable phase (Hazen et al., 2013).

In order for diamonds to be liberated, low percent melts derived from the extreme pressures at the base of cratonic nuceli mantle keels need to occur (Tainton and McKenzie, 1994). These melts occur within the DSF or deeper and are the medium for diamond exhumation (Stern et al., 2016). The relationship between cratonic nuclei and diamondiferous kimberlites is known as Clifford's Rule (Clifford, 1966). Residence of diamonds outside of a cratonic mantle keel are likely to slowly graphitize and/or resorb before exhumation (Shirey and Shigley, 2013). Rocks derived from these kimberlitic eruptions are the only known source of diamonds from the mantle (Shirey and Shigley, 2013; Stern et al., 2016). Kimberlite volcanism includes three rocks: kimberlite, lamproite, and lamprophyre. Each rock type is ultramafic and ultrapotassic with high abundances of volatile phases such as carbon dioxide and water. The distinction between each

type is that kimberlites tend to be concentrated in potassium and have abundant phenocrysts of olivine. While lamproite has phenocrysts of diopside and phlogopite with less olivine. Lamprophyre is absent of olivine. The primary source region of each is thought to be within or below the DSF (Sparks, 2013). These distinctions are often difficult due to 59.7% of global kimberlitic volcanism occurring during the Mesozoic (Stern et al., 2016) and the rapid erosion/alteration of ultramafic material. During transport of magma to the surface, alteration due to changes in temperature and resorption of entrained materials also changes the chemistry of the magma making original chemistry difficult to elucidate (Sparks, 2013). Changes occurring within the ascending magma due to these changes may also cause serpentinization (Hausel, 1998).

Within the primary source region of kimberlitic magmas, diamond entrainment occurs. Kimberlitic melts destabilize silicate grains and entrain diamondiferous xenoliths or xenocrysts (Shirey and Shigley, 2013). This disequilibrium of silicate phases is a factor of the extreme partitioning of incompatible and volatile elements to kimberlite magmas (Sparks, 2013). However, Russell et al. (2012) proposed that during ascent of kimberlite magmas, xenoliths or xenocrysts of mantle material will resorb and cause carbon dioxide to disseminate from theorized original carbonatite composition. This increase in gaseous phases effect on the rate of ascension or propagation is highly debated (Lensky et al., 2006; Wilson and Head, 2007; Menand and Tait, 2001). Lensky et al. (2006) and Wilson and Head (2007) hypothesized the increase of volatile components have a proportional effect on ascension rate and predicts the rate of ascent being in the tens of meters per second. This rate of ascent for kimberlite magmas is thought to be the distinguishing factor for diamondiferous kimberlites and diamond free basalts (Shirey and

Shigley, 2013). Without the rapid ascent, diamond resorption or graphitization occurs before eruption.

**Stable Isotopes**

Within the DSF, carbon supersaturation conditions are an enigma. During the Haden magma ocean, researchers have hypothesized that volatile elements such as H, C, N, and S are removed from the mantle to the early atmosphere (Yuan et al., 2016). What volatile elements remained in the mantle after a siliceous crust had formed are isotopically homogenized (Dasgupta, 2013). The homogenized mantle is standardly referred to by many as the primordial reservoir.

Of all stable carbon on Earth, 97.93% is Carbon-12 and 1.1% is Carbon-13. Isotopes of lighter elements are easily fractionated at surface temperature and pressure regimes. This phenomenon is a result of the change in behavior of a molecule with variant isotopic composition due to quantum mechanical operations. Bonds of molecules have been generalized in multiple models such as harmonic and anharmonic oscillation. Within a molecule, atoms bound together will constantly vibrate further and closer apart. This vibrational frequency is a function of mass, bond length and the vibrational state of the molecule. Generally, bonds with isotopically lighter compositions will have higher vibrational frequencies and are less stable. While bonds with isotopically heavier compositions have lower vibrational frequencies and are more stable. Changes to preferred isotopic composition in bonds are due to the inverse relationship between isotopic weight and vibrational frequency. However, if the molecule is not in the ground vibrational state, then isotopic influence on bond stability is mitigated. Changes to

the vibrational state of a molecule are a function of ambient conditions such as temperature and pressure. Chacko et al. (2001) derives the physical chemistry summarized here.

Diamonds are made of C, N, B and impurities. Carbon, nitrogen and boron isotopes are expressed using delta notation. For these isotopic systems, $^{13}C/^{12}C$, $^{15}N/^{14}N$, and $^{11}B/^{10}B$ ratios are measured. For carbon, the ratio of $^{13}C/^{12}C$ is weighted relative to Vienne Pee Dee Belemnite (VPDB) and expressed as a per mille (‰) value.

$$\text{Equation 1} \quad \delta^{13}C = \left( \frac{^{13}C/_{12}C_{Sample}}{^{13}C/_{12}C_{Standard}} - 1 \right) * 1000$$

In equation 1, $^{13}C/^{12}C$ sample is the analyte and $^{13}C/^{12}C$ standard is the internationally accepted ratio of VPDB from Verkouteren and Klinedinst (2004). Delta notation for nitrogen and boron are similar to equation 1 though with different standard mediums. Nitrogen in diamond analyses are measured for concentration and used to classify diamond types (Deines et al., 1993). Part per million concentrations of boron have been observed in some localities, but no systematic studies have been conducted on boron isotopes or concentrations in diamond (Cartigny, 2005).

Diffusivity of carbon and nitrogen in the diamond structure are similar at mantle conditions. According to experimental modeling by Koga et al. (2003), heterogeneity of carbon isotopes between growth zones are preserved at a 1.6 µm resolution after one billion years of 1300 to 1400 K. Nitrogen diffusivity changes after one million years at similar conditions due to changes in the aggregation state. With relatively faster diffusivity of nitrogen in Type Ib states compared to Type IaA. Nitrogen isotopic heterogeneity after one billion years of 1300 to 1400 K are preserved at 0.1 µm resolution for aggregation states IaA and IaB.

**Carbon Isotopes.** Diamonds worldwide show $\delta^{13}C$ values in two major populations, $\delta^{13}C$ values of -5 ± 1‰ and < -10 ‰ VPDB (Cartigny, 2005; Shirey et al., 2013; Shirey and Shigley,

2013). The first $\delta^{13}C$ value is equal to the average mantle. While the deviation from the average mantle shown in the second value is an active research question. This variation may be explained by mixing surficial carbon reservoir(s) with the primordial reservoir, isotopic fractionation of carbon at mantle conditions, or heterogeneities within the primordial reservoir. The different carbon source model argues for the mixing of carbon from materials in the subducted oceanic slab with the primordial mantle (Kirkley et al., 1991). Stable isotopes readily fractionate at lower temperature and pressure; increasing these conditions causes a change in the bonding habit of isotopes. This change may be marked by crystallization of diamond from different carbon phases such as methane or carbon dioxide. Deines (1980) modeled the isotopic fractionation of crystallizing diamond from methane and carbon dioxide. These models showed that crystallization from carbon dioxide results in diamond showing the primordial value. While starting with methane results in carbon values heavier, more negative, than the primordial value. Heterogeneity of the primordial reservoir argues that mantle convection did not fully mix the mantle once the crust had formed. Evidence of primordial heterogeneity of carbon values is attributed to the variances in carbon values in meteorites.

The different carbon source model has been growing in popularity (Logvinova et al., 2015; Shirey and Richardson, 2011; Walter et al., 2011). Using data compiled by Cartigny et al. (2009) regions such as Guaniamo and Argyle have E-type diamond populations with average values of -16 and -11 ‰ and P-type average values of -6.3 and -6.8 ‰ VPDB, respectively (Figure 1). However, E-type diamonds from New South Wales have an average value of 0.4 ‰ and P-type have an average value of -3.5 ‰ VPDB (Figure 2). Some mines in Africa plot within error of the primordial reservoir (Figure 2). Mass balancing of fractionated carbon sources from the surface with the primordial mantle could explain each regions deviation from the primordial

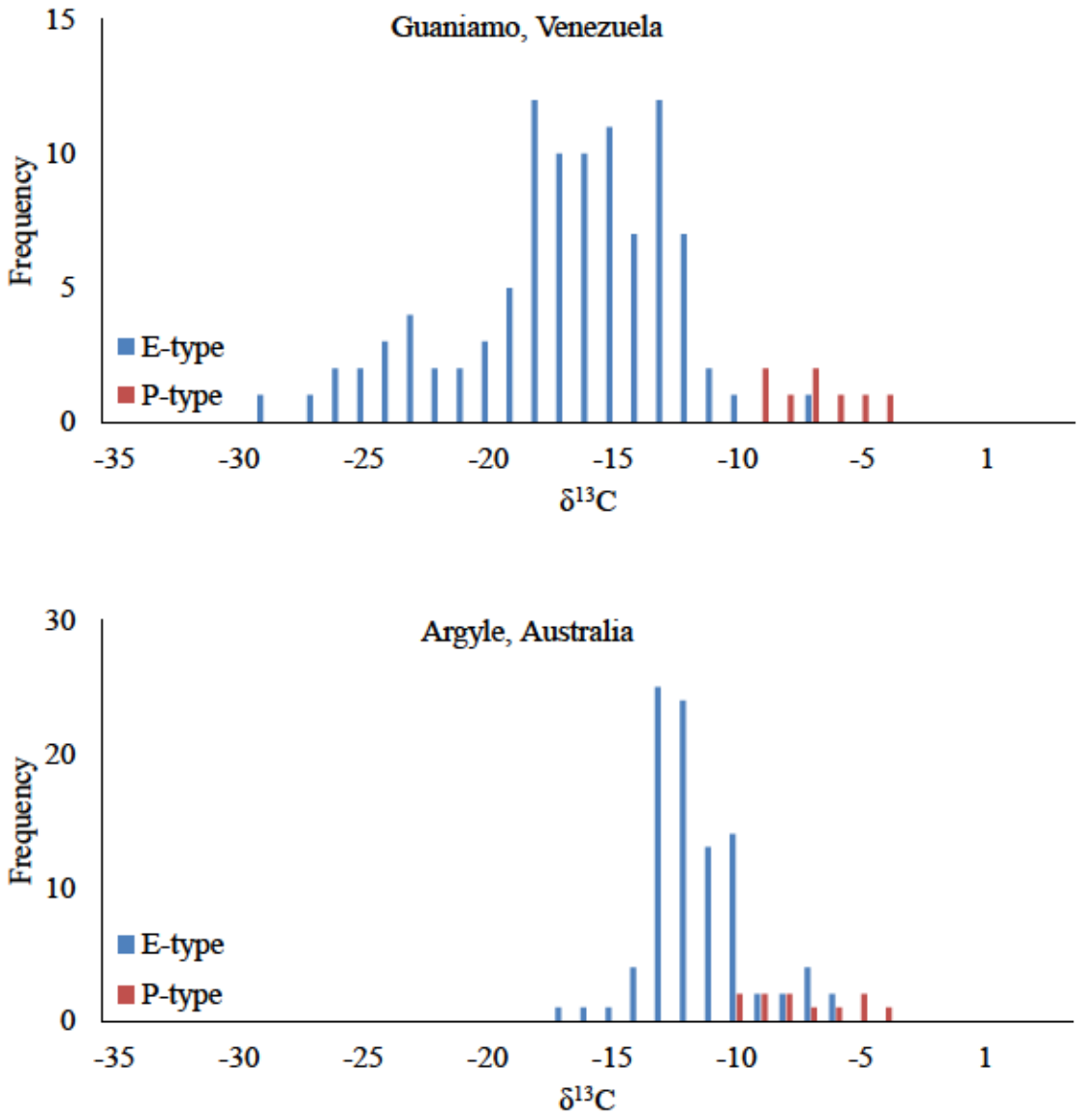


Figure 1. Frequency plots of diamonds from the Guaniamo mine in Venezuela and Argyle mine in Australia. Data for the Venezuela plot is from Kaminsky et al. (2000) and Galimov et al. (1999). Data for the Australia plot is from Jaques et al. (1986). Cartginy et al. (2009) compiled data from these sources.

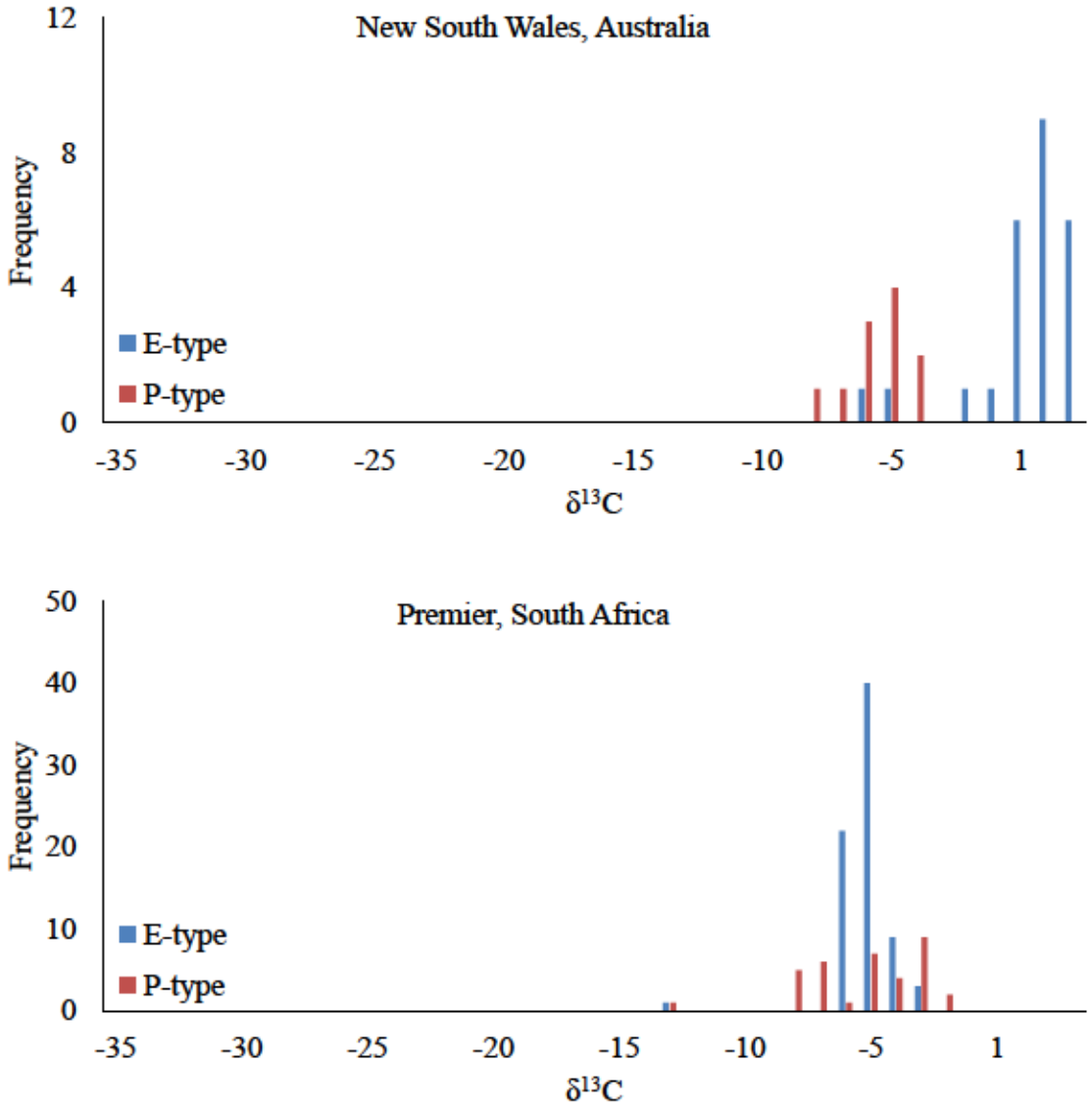


Figure 2. Frequency plots of diamonds from New South Wales, Australia and Premier mine in South Africa. Data for the Australia plot is from Davies et al. (1999, 2002, and 2003). Data for the South Africa plot is from Deines et al. (1989). Cartginy et al. (2009) compiled data from these sources.

mantle. For example, in New South Wales, the primordial mantle may have mixed with carbon derived from carbonate rocks. Carbonate rocks have an average $\delta^{13}C$ value of 1 ± 2 ‰ VPDB. While the more negative carbon values of Guaniamo and Argyle could be from mixing of organic material with the primordial source. Organic material such as benthic or algae have an average $\delta^{13}C$ value of -20 ± 2 ‰ VPDB. However, fractionation of carbon isotopes during diamond crystallization at mantle conditions have achieved similar $\delta^{13}C$ values by precipitating diamond from gases such as methane for isotopically lighter values or carbon dioxide for replicating the primordial reservoir (Deines, 1980). Due to the inconclusive nature of analyzing carbon isotopes in diamond, nitrogen studies need to be done in tandem.

**Nitrogen Contents.** Nitrogen in diamonds is the most common exchange. For sublithospheric mantle diamonds, nitrogen concentration are on average > 300 ppm. While diamonds formed in metamorphic environments range from hundreds to thousands of ppm (Deines et al., 1993). Diamonds from the transition zone or shallow mantle are more likely Type II with worldwide average values < 50 ppm (Cartigny, 2005). The aggregation state of nitrogen in the diamond structure is a measure of time under lithospheric or sublithospheric conditions (Shirey et al., 2013). In type Ib diamonds, single nitrogen atoms have similar diffusivities as carbon. However, at mantle conditions the energy for type IaA, N-N bonds, aggregations are easily achieved. Once IaA aggregation occurs, the diffusivity of nitrogen drops to the point that heterogeneity of nitrogen concentrations across growth zones are preserved for at least 1 billon years at mantle conditions (Koga et al., 2003). Thus, Type Ib diamonds spend less time than Type IaA and Type IaB spend the most time at lithospheric or sublithospheric conditions. Stark contrasts in nitrogen concentrations have been observed in natural diamonds by FTIR

(Mendelsohn and Milledge, 1995). With dramatic changes being interpreted as different generations of fluids.

**Nitrogen Isotopes.** Nitrogen isotopes show similar variation as carbon in diamond. The average value of $\delta^{15}N$ in diamond is -5 ± 3‰ relative to air. With the global dataset of diamonds ranging from -25 to +15 ‰ relative to air. The mixing model hypothesis for explaining isotopically lighter carbon values is applied to nitrogen values. Metasediment nitrogen isotope values are all isotopically heavy or positive relative to air. Nitrogen isotope values, due to the fractionation of $^{15}N$ during subduction, contradict the mixing model (Haendel et al., 1986). The mixing of carbon sources predicts that E-type diamonds are genetically related to organic material volatizing from the subducted slab. This relationship would predict that fractionation of $^{15}N$ to the subducted slab should cause E-type diamonds to have isotopically heavier $\delta^{15}N$ values. However, E-type diamonds show 70% of analyses have isotopically lighter nitrogen values (Cartigny, 2005).

**Time of Flight Secondary Ionization Mass Spectrometry**

Secondary Ionization Mass Spectrometry (SIMS) methods are relatively new (Siljeström, 2011). These analysis methodologies are necessary for spatially restricted or low analyte questions. These questions include diffusion between/along growth zones or between phases, geochronology of individual growth zones, and geochemical analyses of inclusions. In the case of diamond geochemistry, SIMS methodologies are well suited for measuring stable isotope geochemistry between growth zones or geochemical/geochron analysis of inclusions.

SIMS analyses all operate in a similar fashion. The ion source bombards a polished sample surface of analyte with an ion beam(s) generating secondary ions (Stern, 2009). This

beam transfers kinetic energy and changes electron state in the bonded analyte lattice. Kinetic exchanges sputter minor pits relative to other mass spectrometry methods. For example, laser ablation mass spectrometry generate 50 μm wide and ≥ 20 μm depth pits. While SIMS methods can be as minimal as 10 μm wide and ≤ 5 μm depth pits. Sputtered material can be ionized due to the excitation/exchange of electrons. The ionization efficiency in SIMS analysis is low. With ≈ 1 % of sputtered material being ionized (Stephan, 2001).

While a minimum portion of analyte is ionized, the process by which these ions are generated occurs after the material is liberated from the analyte surface (Stephan, 2001). Leading up to this moment, the matrix effect is the dominant phenomena for which atoms are sputtered from the lattice (Stephan, 2001). The matrix effect is most generically summarized as the probabilistic influence on which ionic sites are liberated during ion gun impacts (Stephan, 2001). As a primary ion hits the crystal lattice, some ionic sites in the structure are more likely to be removed while other sites are more robust. The matrix effect is assumed to be normalized in the use of a standard mineral that is crystallographically as similar as possible to the unknown mineral (Stephan, 2001). Such a standard in theory would have the same matrix effect fractionations as an unknown mineral and thus what effect if any can be normalized.

Time of Flight Secondary Ionization Mass Spectrometry (ToF-SIMS) instruments operate by firing two ion beams in pulses. These ion beams fire every nanosecond and impact the analysis material. The cesium sputter beam is fired and implants $Cs^+$ ions. This process improves ionization efficiencies of secondary ions during analysis beam operation. The analysis beam is a $Bi^+$ ion beam. This beam generates secondary ions by transferring kinetic energy into the sample and overcoming the dissociation energy of bonds. Stephan (2001) has described the quantum mechanical operations taking place during secondary ion generation. Secondary ions from the

surface are accelerated through a potential field toward lenses, correction filter(s) and finally a detector. These filters account for the different velocity of ionized phases due to different masses.

$$\text{Equation 2} \quad v = \sqrt{2qV/m}$$

Equation 2 shows the inverse relationship between velocity (v) and mass (m) accounting for charge (q) and the potential field (V). To correct for velocity differences, the accelerated ion phases are directed into a magnetic dampening field with induced currents antiparallel to the primary vector of secondary ions. Ions of different masses penetrate the dampening field as they are accelerated along the new V. This filter generates a gap between ions due to different mass. This gap closes as both phases travel to the detector. The detector on some ToF-SIMS works by measuring the time from ions hitting the first focusing leans and secondary ion detection. However, other ToF-SIMS instruments allow secondary ions to drift in a neutral tube after being accelerated through a potential field toward the detector.

$$\text{Equation 3} \quad t = L\sqrt{m/2qV}$$

In equation 3, L is length that ion species travel. Detectors are only able to detect ions every 10s of microseconds due to the flight time of ions. Since the detectors operate in a kinetic sense, ToF-SIMS is able to resolve all mass spectra during analysis. Compared to other SIMS methods where mass spectrometer detect specific mass-to-charge ratios.

## METHODS

This study includes chemical imaging and isotope ratio mass spectrometry. A Time-of-Flight Secondary Ionization Mass Spectrometer (ToF-SIMS) chemically imaged six diamonds from Canada and United States and three calcite crystals from the Magnet Cove carbonatite in Arkansas, USA. ToF-SIMS element maps transect from core-to-rim of crystals. Element maps of $^{12}C$, $^{13}C/^{12}C$, and $^{16}O$ were used to characterize intracrystalline variation. Eleven drill bores of calcite were analyzed for $\delta^{13}C$ and $\delta^{18}O$ values. Reported stable isotope values of calcite are used as an internal standard for ToF-SIMS analysis. This standard was used to calculate stable isotope values for carbon in diamond and test if the ToF-SIMS could replicate carbonatite isotope values.

### Internal Standard

Calcite crystals of Magnet Cove carbonatite from Malvern, AR were used as an internal standard. Eleven drill bores from regions of pure calcite were cleaned and milled into a powder using a micro drill at Missouri State University. Each sample yielded 1 to 10 mg of powdered calcite and were brushed into vials. Powders were analyzed for $\delta^{13}C$ and $\delta^{18}O$ values at the Stable Isotope Laboratory at University of Missouri - Columbia by Isotope Ratio Mass Spectrometry (IRMS). $\delta^{13}C$ and $\delta^{18}O$ values reported as per mille (‰) relative to VPDB. Analysis methodology follows Bassett et al. (2007). Average $\delta^{13}C$ and $\delta^{18}O$ values with $2\sigma$ error of the eleven bores was $-5.51 \pm 0.16$ and $-22.6 \pm 1.5$ VPDB, respectively.

### Sample Preparation

Diamonds for this study originate from a kimberlite in the Slave Province of the Northwest Territories of Canada and a lamproite in Murfreesboro, Arkansas. The diamonds from the Slave Province originated from the Diavik pipe. This pipe intruded the Slave Province craton between 45 to 140 Ma from a depleted mantle keel (MacKenzie and Canil, 1998). The diamond from Murfreesboro, Arkansas is from the Prairie Creek lamproite. This lamproite intruded a shallow marine environment along the southern margin of Laurentia 100 Ma from an enriched section of sublithospheric mantle (Howard and Hanson, 2008).

This study used five diamonds from the Northwest Territories of Canada and one diamond from Murfreesboro, Arkansas. These diamonds will be referred to as SL-1, SL-2, SL-3, SL-4, and SL-5 for the Northwest Territory diamonds and AR for the Arkansas diamond. Diamonds from the Diavik pipe were selected because of recent stable isotope characterization by Van Rythoven (2012) and diamond accessibility. Van Rythoven (2012) analyzed core and rim of diamonds with intracrystalline $\delta^{13}C$ variability outside analytical error. Van Rythoven (2012) carbon isotope values of diamonds from the Diavik mine were used to determine the accuracy of ToF-SIMS analyzing diamonds from the same mine. The diamond from Arkansas was selected because there are no known high spatial resolution isotope data sets. The Magnet Cove carbonatite selected for our internal standard represents rock related to the diamondiferous host of the Arkansas diamond.

Using a standard stereo microscope with camera, morphologic descriptions of each diamond were made for cutting instructions. Each diamond was marked with a line parallel to their longest dimension. Diamonds were sent to the Gemological Institute of America Research Lab in New York City for laser cutting and polishing. Diamonds were cut along this marked line and intersected the center of each diamond to expose the greatest internal surface area. Polished

diamond halves and Magnet Cove carbonatite crystals were pressed with the polished side up into indium metal with an Arbor Press. Indium pucks with mounted crystals are in one-inch diameter hollow aluminum pucks standing a quarter of one-inch. The three pucks contain a combination of diamonds and carbonatite calcite crystals. Puck one contains the diamonds SL-3 and SL-4 with one standard. Puck two contains the diamonds SL-2, AR, and SL-5 with one standard. Puck three contains SL-1 with two standards. Puck four only contains four standards.

**ToF-SIMS Analysis**

One inch round pucks with the mounted diamond and carbonatite where transported to Oak Ridge National Labs Center for Nanophase Material Science. The Atomic Force Microscope ToF-SIMS was operated with a $Bi^+$ primary analysis beam at a voltage of 30 keV and a $Cs^+$ sputter beam at a voltage of 2 keV. The primary beam operational voltage was progressively increased to 30 keV to improve counts received. This $Bi^+$ primary beam is used to generate secondary ions for analysis. While the $Cs^+$ sputter beam is used to clean the surface and implant into the crystal for greater ionization potential during primary beam operation. The analysis window for Canadian diamonds and carbonatite samples was 500 x 500 µm with 700 x 700 µm sputter window. The Arkansas diamond had three analysis windows of 500 x 500 µm and 700 x 700 µm sputter window and one analysis window of 300 x 300 µm with 500 x 500 µm sputter window. The Arkansas diamond had different analysis dimensions to maximize how much of the diamonds polished surface was analyzed. The instrument operated in random raster mode, dividing the analysis window into 256 x 256 pixels with each pixel being 1.95 x 1.95 µm for 500 x 500 µm and 1.12 x 1.12 µm for 300 x 300 µm analysis windows. All Canadian diamond analyses were transects of core-to-rim. The Arkansas diamond had analysis windows

covering the polished surface. Each analysis window is separated by 400 μm to ensure that the edges of the sputter window are not in the analysis window. Ridges formed at the edge of the sputter window can cause topologic errors if included in the analysis window.

During analysis, each pixel in a window is randomly analyzed twice with the detector capable of measuring an ion species every picosecond. The average time of anion analysis for Canadian diamonds was 31 minutes for each window. The average analysis time for Arkansas diamond windows was 41 minutes. The anion species presented here are $^{12}C$, $^{13}C$, and $^{16}O$. However, the ToF-SIMS gave spectral data for all ionized anions. Cation analyses were done on diamonds AR and SL-2. These cation analyses included Al, Ca, Fe, Mg and Si. Anion analyses are reported as unmodified spectral counts. Element maps and ASCII files were created for each anion and cation species per analysis window. ASCII files are organized as a matrix to retain spatial information of the analyzed pixels with the intensity of each pixel being that species count. Data sets were reduced and processed in Microsoft Excel.

ASCII files of analysis windows were used to create image transects and spectral intensity conversion models. Two of the five Canadian diamonds, SL-3 and SL-5, had topologic errors that made ToF-SIMS analysis trivial. Errors observed in these diamonds included extensive cracking throughout SL-5 and parallel surficial lineations in SL-3 potentially from the polishing or mounting procedure. For all other diamonds, three vertical and horizontal transects were created for the $^{12}C$ species in each analysis window. Transects are at the quarter, half, and three quarters length in the vertical and horizontal dimension. Raw transects are reduced to $4^{th}$ order polynomial best fit lines to determine variation in $^{12}C$ counts. This reduction was done due to the amount of points per transect making evaluation computationally expensive.

The Arkansas diamond and one Canadian diamond were selected for further anion image analysis. The Arkansas diamond was used to test the viability of imaging $^{12}C$ or $^{13}C/^{12}C$ variability in a gem quality homogenous diamond. The Canadian diamond selected, SL-2, has a subhedral mineral inclusion showing intracrystalline zonation of $^{12}C$. Additional image analysis included transects of $^{13}C/^{12}C$ for AR along the same $^{12}C$ transects and $^{12}C$, $^{13}C/^{12}C$ and $^{16}O$ along tighter intervals for the SL-2 mineral inclusion.

**Signal Intensity Conversion**

ToF-SIMS analysis potentially generates Signal Intensities (SI) of all atoms present in the analyte. However, the instrument can not directly convert SI to stable isotope values. The isotope values for carbonatite were used as a conversion standard of SI in carbonatite.

$$\text{Equation 4} \quad \left[E/E_0\right]\text{Sample} = \frac{\left[SI(E)/SI(E_0)\right]_{\text{Sample}}}{\left[SI(E)/SI(E_0)\right]_{\text{Standard}}} * \left[E/E_0\right]\text{Standard}$$

Stephan (2001) uses equation 4 as a general conversion of SI to isotope ratios. Using equation 4 and equation 1 gives isotopic values. These values show error percentages of 500 to 32000% for carbonatite and have calculated values -2000 to +100 ‰ VPDB for carbon values in diamond.

## RESULTS

To determine whether Time of Flight Secondary Ionization Mass Spectrometry (ToF-SIMS) is a viable stable isotope methodology for diamond, I tested if our data could replicate published data from other instrument methods and if chemical spatial characterization is possible. This replication process included the establishment of an internal standard by Isotope Ratio Mass Spectrometry (IRMS) and chemical image transects of ToF-SIMS analysis windows. The internal standard was established with 11 drill bores of optically pure calcite from the Magnet Cove carbonatite. These calcite powders were analyzed by IRMS for $\delta^{13}C$ and $\delta^{16}O$ values. Calcite crystals were also mounted with diamond and analyzed by ToF-SIMS. Chemical image evaluation of four diamonds included 24 analysis windows and 150 $^{12}C$, 30 $^{13}C/^{12}C$, and six $^{16}O$ transects. These transects included 44,493 data points, 0.94% of the total anion dataset for elemental carbon and oxygen isotopes in diamond.

IRMS analysis characterized the Magnet Cove carbonatite carbon and oxygen stable isotope values. In equation 4 (Stephan, 2001), E is an element, $E_0$ is an isotope of the same element and SI is signal intensity. IRMS values were used as the standard isotopic ratio $\left[{}^{E}/_{E_0}\right]$ to convert SI to isotopic values. Results of these conversions and the associated errors are presented.

All chemical image transects of $^{12}C$ are described for four diamonds. Additional image analysis for AR includes six $^{13}C/^{12}C$ transects for four windows. Additional image analysis for SL-2 includes six transects of $^{12}C$, $^{13}C/^{12}C$ and $^{16}O$ for an inclusion in window-28. Surficial errors are presented for SL-3 and SL-5.

**Carbonatite Stable Isotopes**

Carbon and oxygen stable isotope values for Magnet Cove carbonatite presented are the first known stable isotope values. IRMS analysis of calcite millings from carbonatite yielded isotopic values for $\delta^{13}C$ and $\delta^{18}O$ with ranges of -5.36 to -5.70 and -20.90 to -23.11‰ VPDB, respectively (Table 1). Average values for $\delta^{13}C$ and $\delta^{18}O$ with 2σ error are -5.51 ± 0.16 and -22.6 ± 1.5‰ VPDB. The average value of $\delta^{13}C$ was converted to an isotopic ratio for use in ToF-SIMS SI to value conversions. Standard VPDB $^{13}C/^{12}C$ ratio used was 0.0112372 (Verkouteren and Klinedinst, 2004). Solving equation 1 for $^{13}C/^{12}C$ sample, the range for $^{13}C/^{12}C$ in calcite bores was 0.011174467 to 0.011176969 with a 2σ error of $1.8e^{-6}$ (Table 1).

**ToF-SIMS Signal Intensity Conversion**

Four crystals of calcite were mounted in indium with diamonds for ToF-SIMS analysis. Each calcite was analyzed for $^{12}C$ and $^{13}C$ for a minimum of two analysis windows. Using a calcite crystal with three analysis windows as the $\left[{}^{SI(E)}/_{SI(E_0)}\right]$ standard. SI to $\delta^{13}C$ conversion of the remaining three calcite crystals and diamonds AR and SL-1 were calculated using equation 4 and the average $^{13}C/^{12}C$ ratio from Table 1. Table 2 contains all of these calculated $^{13}C/^{12}C$ ratios and $\delta^{13}C$ values. Calculated values are then compared to known $\delta^{13}C$ values of calcite from IRMS, the Diavik mine (Van Rythoven, 2012) for SL-1 and Murfreesboro, AR (McCandless et al., 1991) for AR.

**Diamond ToF-SIMS Analysis**

Morphology of diamonds in this study range from industrial quality borts to resorbed octahedral sub-gem to gem quality stones. AR is a sub-gem to gem quality homogenous yellow

Table 1. Isotope Ratio Mass Spectrometry carbon and oxygen stable isotope data of Magnetite Cove carbonatite millings. $\delta^{13}C$ and $\delta^{18}O$ values are per mille relative to Vienna Pee Dee Belemnite.

| | $\delta^{13}C$ | $^{13}C/^{12}C$ Ratio | $\delta^{18}O$ |
|---|---|---|---|
| msu-1.0 | -5.46 | 0.011175793 | -22.95 |
| msu-1.1 | -5.47 | 0.011175694 | -22.96 |
| msu-2 | -5.46 | 0.011175803 | -22.95 |
| msu-3 | -5.47 | 0.011175704 | -21.34 |
| msu-4 | -5.58 | 0.011174467 | -23.06 |
| msu-5 | -5.54 | 0.011174964 | -23.11 |
| msu-6 | -5.36 | 0.011176969 | -20.90 |
| msu-7 | -5.50 | 0.011175422 | -22.87 |
| msu-8 | -5.54 | 0.01117499 | -22.82 |
| msu-9 | -5.49 | 0.011175555 | -23.01 |
| msu-10 | -5.70 | 0.011173197 | -22.63 |
| average | -5.51 | 0.011175324 | -22.60 |
| 2σ error | 0.160973512 | 1.80889e-06 | 1.500 |

Table 2. Signal Intensity (SI) conversion of Magnet Cove carbonatite crystals and diamonds SL-1 and AR. SI conversion follows equation 4 (Stephan, 2001). Calcite-2 was used as the SI (standard) value. Percent errors of calcite crystals are relative to Isotope Ratio Mass Spectrometry values from eleven drill bores of the same calcite material (Table 1). Percent errors for SL-1 are relative to an average $\delta^{13}C$ value from six diamonds from the Diavik mine (Van Rythoven, 2012). Percent errors for AR are relative to an average $\delta^{13}C$ value from twenty diamonds from Murfreesboro, AR (McCandless et al., 1991).

| Crystal | Window | $^{12}C$ counts | $^{13}C$ counts | SI(sam) | SI(sam)/SI(std) | $^{13}C/^{12}C$ | $\delta^{13}C$ | $\delta^{13}C$ average | 2σ error | % error |
|---|---|---|---|---|---|---|---|---|---|---|
| STD (Calcite-2) | 1 | 8714 | 50 | 0.005738 | | | | | | |
| | 2 | 7422 | 51 | 0.006871 | | | | | | |
| | 3 | 5548 | 60 | 0.010815 | | | | | | |
| Calcite-1 | 0 | 179459 | 475 | 0.002647 | 0.3389904 | 0.0037883 | -662.876 | 558.4702942 | 2442.693064 | 11930 |
| | 1 | 373974 | 8162 | 0.021825 | 2.7952083 | 0.0312374 | 1779.817 | | | 32402 |
| Calcite-3 | 2 | 5960 | 75 | 0.012584 | 1.6116622 | 0.0180108 | 602.7877 | | | 11040 |
| | 3 | 7494 | 34 | 0.004537 | 0.5810644 | 0.0064936 | -422.135 | 2292.047 | 6283.383795 | 7561 |
| | 4 | 1622 | 98 | 0.060419 | 7.7380981 | 0.0864757 | 6695.489 | | | 121615 |
| Calcite-4 | 1 | 1975 | 37 | 0.018734 | 2.3993501 | 0.0268135 | 1386.138 | 675.8242 | 1420.628236 | 25257 |
| | 2 | 8047 | 61 | 0.00758 | 0.9708560 | 0.0108496 | -34.4899 | | | 526 |
| SL-1 | 0 | 3147277 | 12803 | 0.004068 | 0.5209977 | 0.0058223 | -481.871 | -148.311788 | 285.5850204 | 14958 |
| | 1 | 3460034 | 26765 | 0.007735 | 0.9907085 | 0.0110715 | -14.7467 | | | 361 |
| | 2 | 2676031 | 18192 | 0.006798 | 0.8706594 | 0.0097299 | -134.135 | | | 4092 |
| | 3 | 2496842 | 17094 | 0.006846 | 0.8768224 | 0.0097988 | -128.006 | | | 3900 |
| | 4 | 2704496 | 20253 | 0.007489 | 0.9590959 | 0.0107182 | -46.1853 | | | 1343 |
| | 5 | 2226361 | 15145 | 0.006803 | 0.8712297 | 0.0097363 | -133.568 | | | 4074 |
| | 6 | 2413029 | 17057 | 0.007069 | 0.9053137 | 0.0101172 | -99.6713 | | | 3015 |
| AR | 1 | 1296875 | 9455 | 0.007291 | 0.9337324 | 0.0104348 | -71.4091 | -28.5986803 | 122.8289078 | 1256 |
| | 2 | 1096498 | 7887 | 0.007193 | 0.9212192 | 0.0102949 | -83.8534 | | | 1492 |
| | 3 | 1348896 | 10257 | 0.007604 | 0.9738698 | 0.0108833 | -31.4927 | | | 498 |
| | 7 | 836523 | 7043 | 0.008419 | 1.0782980 | 0.0120503 | 72.36048 | | | 1474 |

to orange octahedral stone 2.5 mm wide. SL-1, SL-2, SL-3, SL-4 and SL-5 are equant borts ranging in size from 3.8 to 5.1 mm with cloudy to clear clarity and some visible mineral inclusions. SL-1 has an octahedral habit and SL-3 has a cubic habit all other diamonds from the Slave province are clusters.

Six diamonds were chemically imaged by ToF-SIMS at Oak Ridge National Labs. Diamonds SL-1 and SL-2 have seven anion analysis windows. SL-4 has six anion analysis windows. AR has four anion analysis windows. AR has cation for all analysis windows. SL-2 has cation for all windows except window-28. SL-4 has cation for window 4. Diamonds SL-3 and SL-5 have surficial errors that made ToF-SIMS analyses trivial. Presentation of ToF-SIMS chemical image transects will include Row (R) and Column (C) transects that will be referred to as R or C and the pixel for which that transects was ran.

**AR.** ToF-SIMS analysis of diamond AR included four windows: window-1, window-2 and window-7 with analysis windows 500 $\mu m^2$ and window-3 with an analysis window of 250 $\mu m^2$. Anion and cation analyses were ran in the same analysis region for each window. Anion analysis on average took 41 minutes and cation analyses on average took 6.3 minutes. Total anions received ranged from 5.3 to 8.2 million counts per window. Total cations received ranged from 11.8 to 49.2 million counts per window.

Window-1. $^{12}C$ within window-1 shows gradational and systematic SI increase with a linear feature void of $^{12}C$ (Figure 3a and 3b). This gradational increase is shown by a 30% average increase in $^{12}C$ SI from left to right within all analysis transects (Figure 3a). This gradational increase is apparent in R128 with the $4^{th}$ degree polynomial (Figure 3c) and moving average (Figure 3d) polylines. The linear feature is measured by R192 (Figure 3a) with the moving average showing a 65% decrease in SI over 41 µm.

Window-2. $^{12}C$ within window-2 shows gradational and systematic SI response and a homogenous diamond crystal. This gradational increase roughly follows from the NW to SE within the analysis window (Figure 4b). This trend is shown by variable change in R and C transects. R64 shows a 7 to 10% increase in SI from left to right. R128 shows a 4 to 8% increase in SI from left to right. R192 shows a 10 to 12% increase in SI form left to right (Figure 4a). C64 shows little to no average change from top to bottom. C128 show minor change <2% in SI from top to bottom. C192 shows a 5 to 7% increase in SI from top to bottom (Figure 4a).

Window-3. $^{12}C$ within window-3 shows homogenous $^{12}C$ SI response (Figure 5b). Minor systematic increase from left to right is shown in the $^{12}C$ element map (Figure 5b), however this trend is difficult to see in the moving average polylines for transects (Figure 5a). In Figure 5c, the 4$^{th}$ order polynomial best fit line of R128 shows a 20% increase from left to right. While the moving average plot of R128 (Figure 5d) shows the SI response to have sporadic increases and decreases back to an average base level that increases from left to right by 10 to 15%.

Window-7. $^{12}C$ within window-7 shows a concave down shape with lower SI in the corners and higher SI towards the center of $^{12}C$ element map (Figure 6b). Moving average polylines of C64 and C192 (Figure 6a) show this trend with their maximum occurring within the center of each transect and minimum values toward the start and end of each transect.

**SL-1.** ToF-SIMS analysis of diamond SL-1 included seven anion windows: window-0, window-1, window-2, window-3, window-4, window-5 and window-6 with analysis windows of 500 $\mu m^2$. Anion analysis of each window on average took 30.7 minutes. Total anions received ranged from 9.2 to 14 million counts per window. Analysis window-1 includes an example figure for other anion phases used to identify linear features and inclusion minerals (Figure 7).

Window-0. $^{12}C$ within window-0 shows homogenous $^{12}C$ SI response (Figure 8b). This homogenous response observed in the $^{12}C$ element map is also present in the 4$^{th}$ order

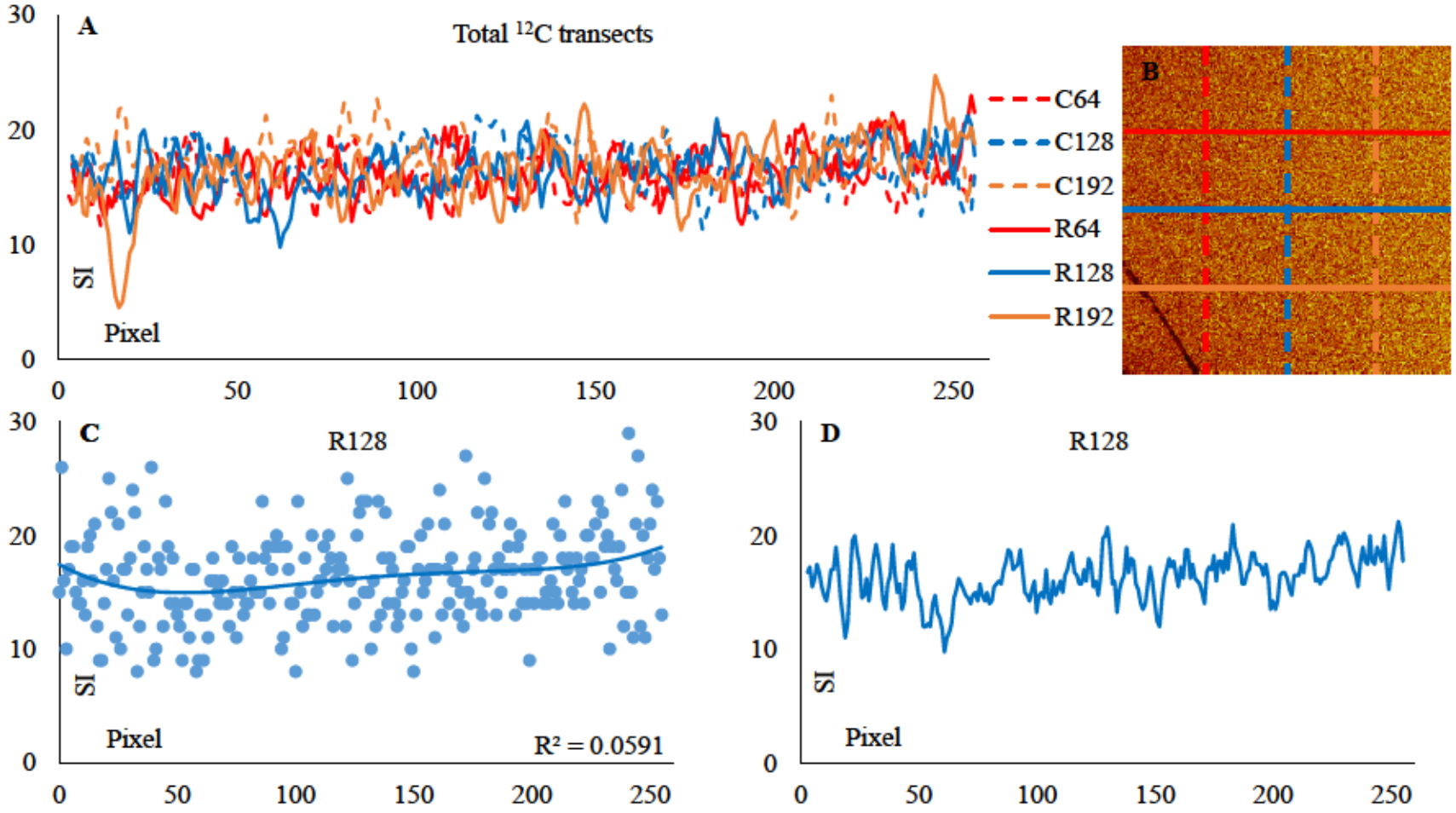


Figure 3. Diamond AR window-1 $^{12}$C analysis. A shows 4$^{th}$ order moving average polylines of row and column transects. B shows the $^{12}$C element map with transects. C shows the raw data of R128 transect with a 4$^{th}$ order polynomial best fit line and $R^2$ value. D shows the moving average polyline of data from row 128. Y-axis is Signal Intensity (SI).

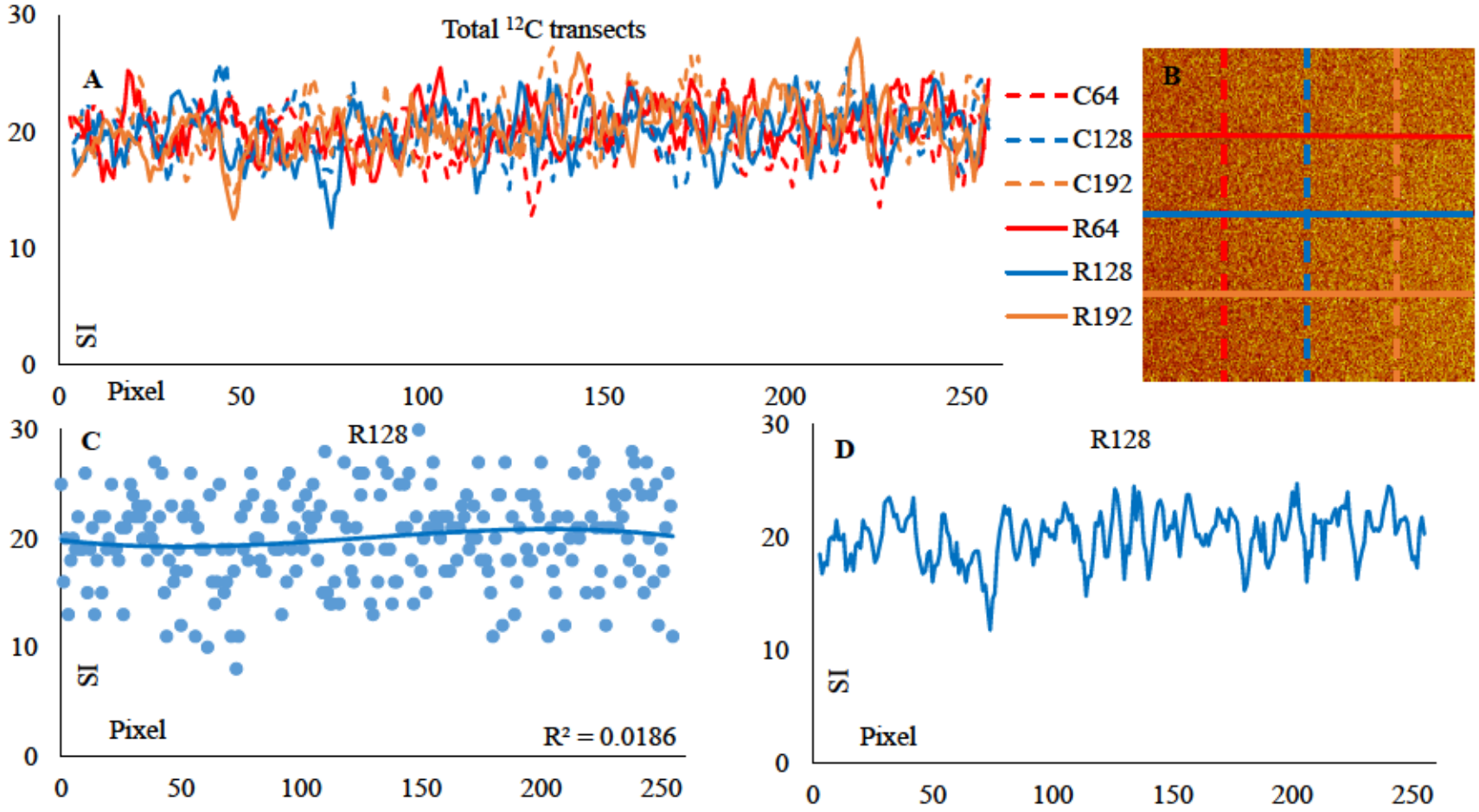


Figure 4. Diamond AR window-2 $^{12}C$ analysis. A shows 4$^{th}$ order moving average polylines of row and column transects. B shows the $^{12}C$ element map with transects. C shows the raw data of row 128 transect with a 4$^{th}$ order polynomial best fit line and $R^2$ value. D shows the moving average polyline of data from row 128. Y-axis is Signal Intensity (SI).

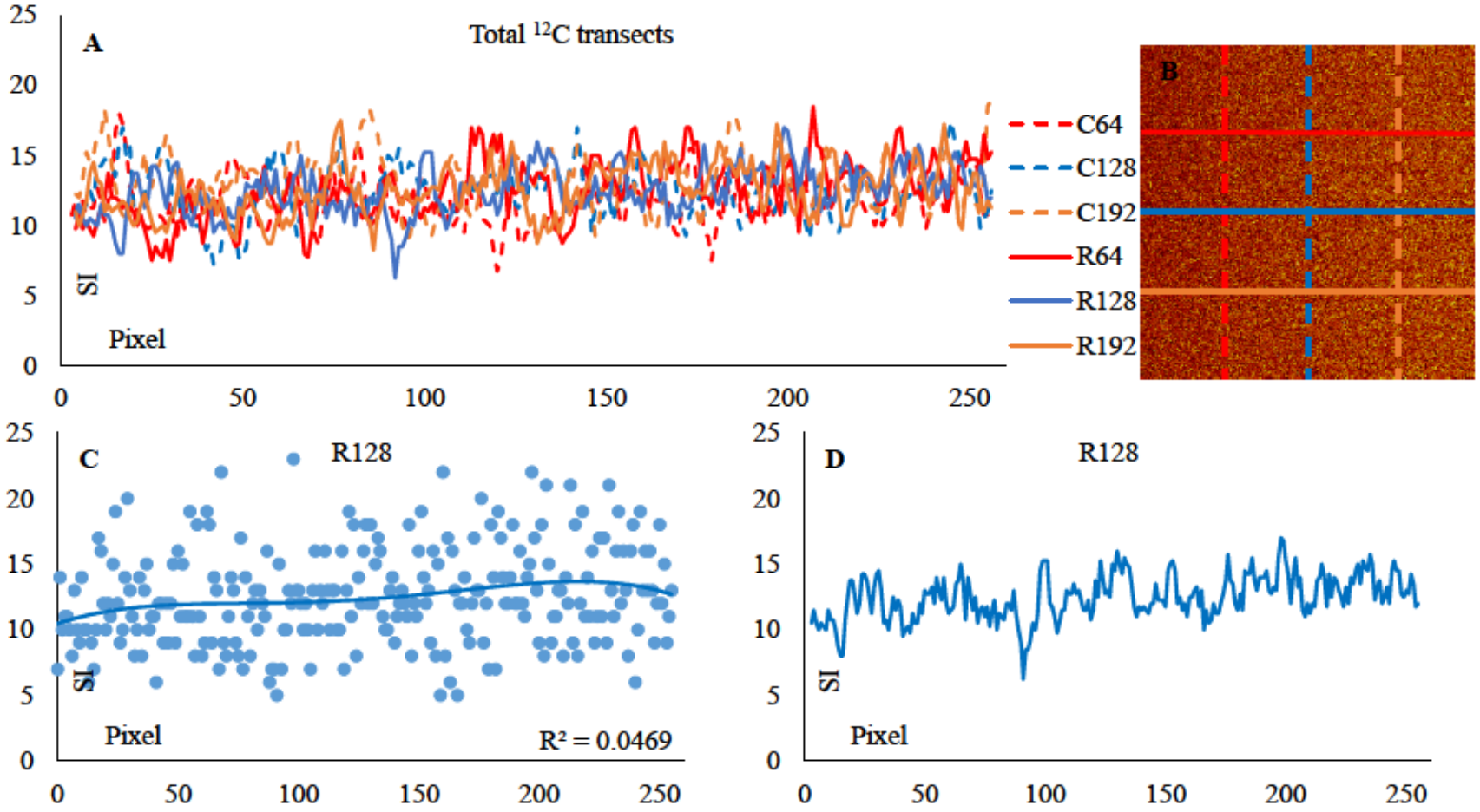


Figure 5. Diamond AR window-3 $^{12}C$ analysis. A shows 4$^{th}$ order moving average polylines of row and column transects. B shows the $^{12}C$ element map with transects. C shows the raw data of row 128 transect with a 4$^{th}$ order polynomial best fit line and $R^2$ value. D shows the moving average polyline of data from row 128. Y-axis is Signal Intensity (SI).

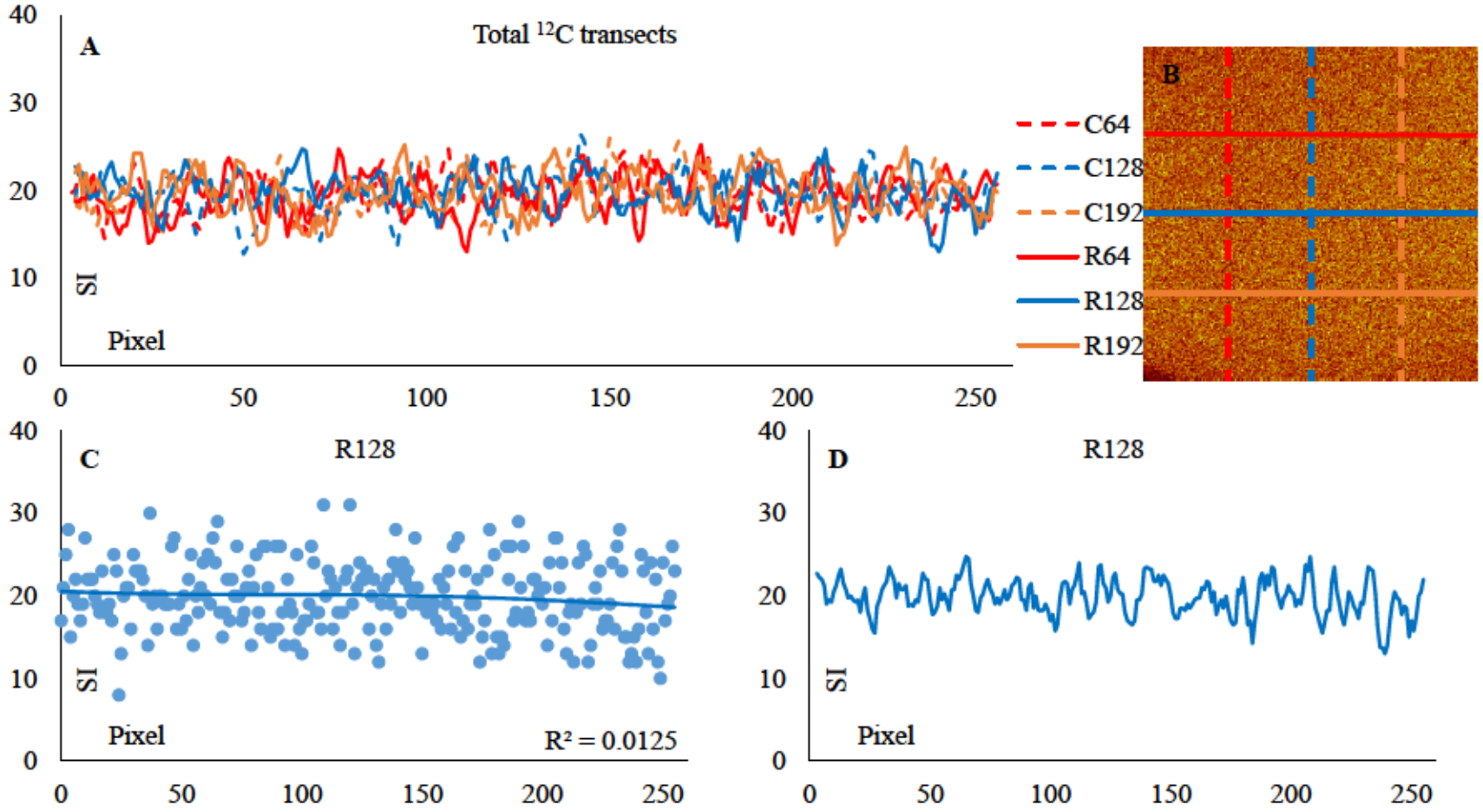


Figure 6. Diamond AR window-7 $^{12}$C analysis. A shows 4$^{th}$ order moving average polylines of row and column transects. B shows the $^{12}$C element map with transects. C shows the raw data of row 128 transect with a 4$^{th}$ order polynomial best fit line and $R^2$ value. D shows the moving average polyline of data from row 128. Y-axis is Signal Intensity (SI).

polynomial best fit and 4th order moving average plots of R128 (Figure 8c and 8d). The SI response shown with the moving average plot of R128 (Figure 8d) shows the greatest variance in SI with ranges between peaks and troughs ≥10. SI of all transects in window-0 (Figure 8a) are within a 2σ error of 31 ± 4.

Window-1. $^{12}C$ of window-1 shows multiple equant mineral inclusions and structures resembling cracks. Features that appear similar to cracks are in the top half of the $^{12}C$ element map marked by minor increases in SI of $^{1}H$ (Figure 7e). This decrease in $^{12}C$ was only present in C64 (Figure 9a). Mineral inclusion phases are identified by dramatic decreases in $^{12}C$ and increases in $^{16}O$ (Figure 7c). In R64 and C192, mineral inclusions show a SI drop from 48 to 0 counts over 3.9 μm (Figure 9a). The SI within these transects remains at 0 for 6 μm before transitioning back to homogenous SI. Diamond contiguous to mineral inclusions show slight perturbation in $^{12}C$ SI (Figure 9b). This perturbation is marked by small halos around each mineral inclusion with higher and/or lower SI of $^{12}C$ relative to the body of diamond.

Window-2. $^{12}C$ of window-2 has a dendritic feature in the right half of the element map (Figure 10b) with diffuse mineral inclusions. $^{12}C$ SI throughout the transects shows a homogenous response (Figure 10a). Inclusions are identified by increases in SI response of $^{16}O$ (Figure 7d). Dendritic feature is defined by increased $^{1}H$ SI (Figure 7f).

Window-3. $^{12}C$ of window-3 shows homogenous SI response with systematic decrease from SW to NE (Figure 11b). This change is shown in R64 and R128 as gradual decrease in SI from left to right and in C192 as gradual increase from top to bottom (Figure 11a and 11d). These changes are marked by 5 to 8% increases in C transects and 2 to 4% decreases in R transects.

Window-4. $^{12}C$ of window-4 has linear features from the NW through SW and SE quadrants. Anhedral minerals less than 4 μm are associated with these linear features (Figure 12b). R128 is the only transect to have intersected a mineral inclusion measuring a 67% decrease in $^{12}C$ SI over 2 μm (Figure 12c). Main body of the $^{12}C$ element map is homogenous with gradual decreases trending from the center of the element map to the NE and SW corners.

Window-5. $^{12}C$ of window-5 has a linear feature spanning the top half of the element map. Two to four mineral inclusions between 1 and 3 μm are present adjacent to this linear feature (Figure 13b). R64 intercepts this linear feature measuring an 87% decrease in $^{12}C$ SI over 11.7 μm (Figure 13a). The main body of the $^{12}C$ element map show a homogenous response (Figure 13c and 13d).

Window-6. $^{12}C$ of window-6 show stepwise increases from left to right in R transects and homogenous in C transects (Figure 14a). This trend is shown in all R transects with higher slope from 0 to 64 pixels, mild slope from 64 to 130 pixels and moderate slope from 130 to 255 pixels. This trend is best shown in R128 4$^{th}$ order polynomial best-fit line (Figure 14c). Within this polynomial, pixel 0 to 26 measured a slope of 0.35 $^{SI}/_{pixel}$, pixel 74 to 133 measured a slope of 0.061 $^{SI}/_{pixel}$ and pixel 167 to 255 measured a slope of 0.068 $^{SI}/_{pixel}$.

**SL-2.** ToF-SIMS analysis of diamond SL-2 included seven anion windows: window-26, window-28, window-29, window-30, window-31, window-32 and window-33 with analysis windows of 500 μm$^2$. All analysis windows were also ran in cation mode except window-28. Window-28 was not ran in cation mode due to potential topological errors in the SE section. Cation analyses showed multiple populations of inclusions. Anion analysis of each window on average took 32.8 minutes with cation analysis taking an average of 10.4 minutes. Total counts

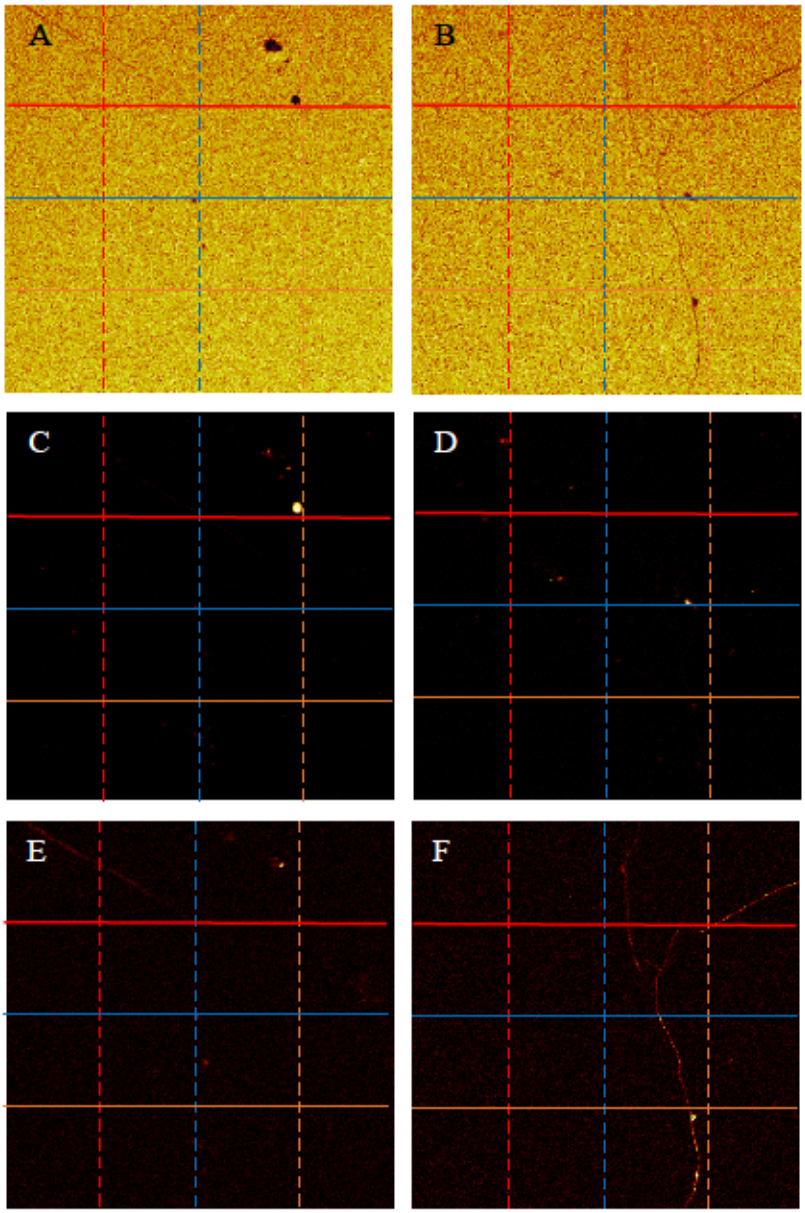


Figure 7. Element maps of $^{12}C$, $^{16}O$ and $^{1}H$ from SL-1. A, C and E are from window-1. B, D and F are from window-2. Element maps A and B are $^{12}C$. Element maps C and D are $^{16}O$. Element maps E and F are $^{1}H$. Element maps show the variable distribution of elements in mineral inclusions or dendritic/linear features. Color of pixels in each element map corresponds to SI with black being equal to 0 and red/yellow being high SI.

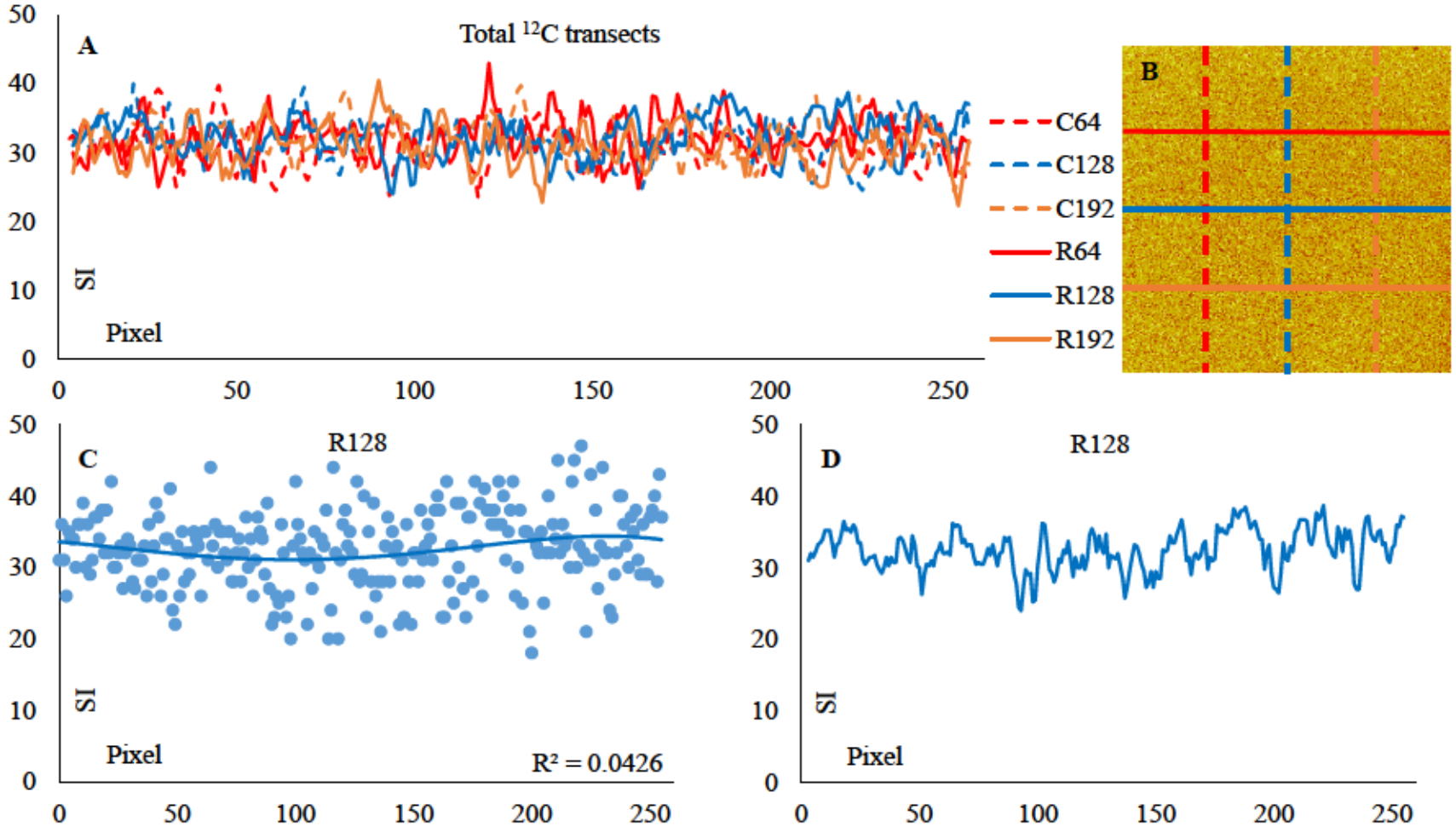


Figure 8. Diamond SL-1 window-0 $^{12}$C analysis. A shows 4$^{th}$ order moving average polylines of row and column transects. B shows the $^{12}$C element map with transects. C shows the raw data of row 128 transect with a 4$^{th}$ order polynomial best fit line and $R^2$ value. D shows the moving average polyline of data from row 128. Y-axis is Signal Intensity (SI).

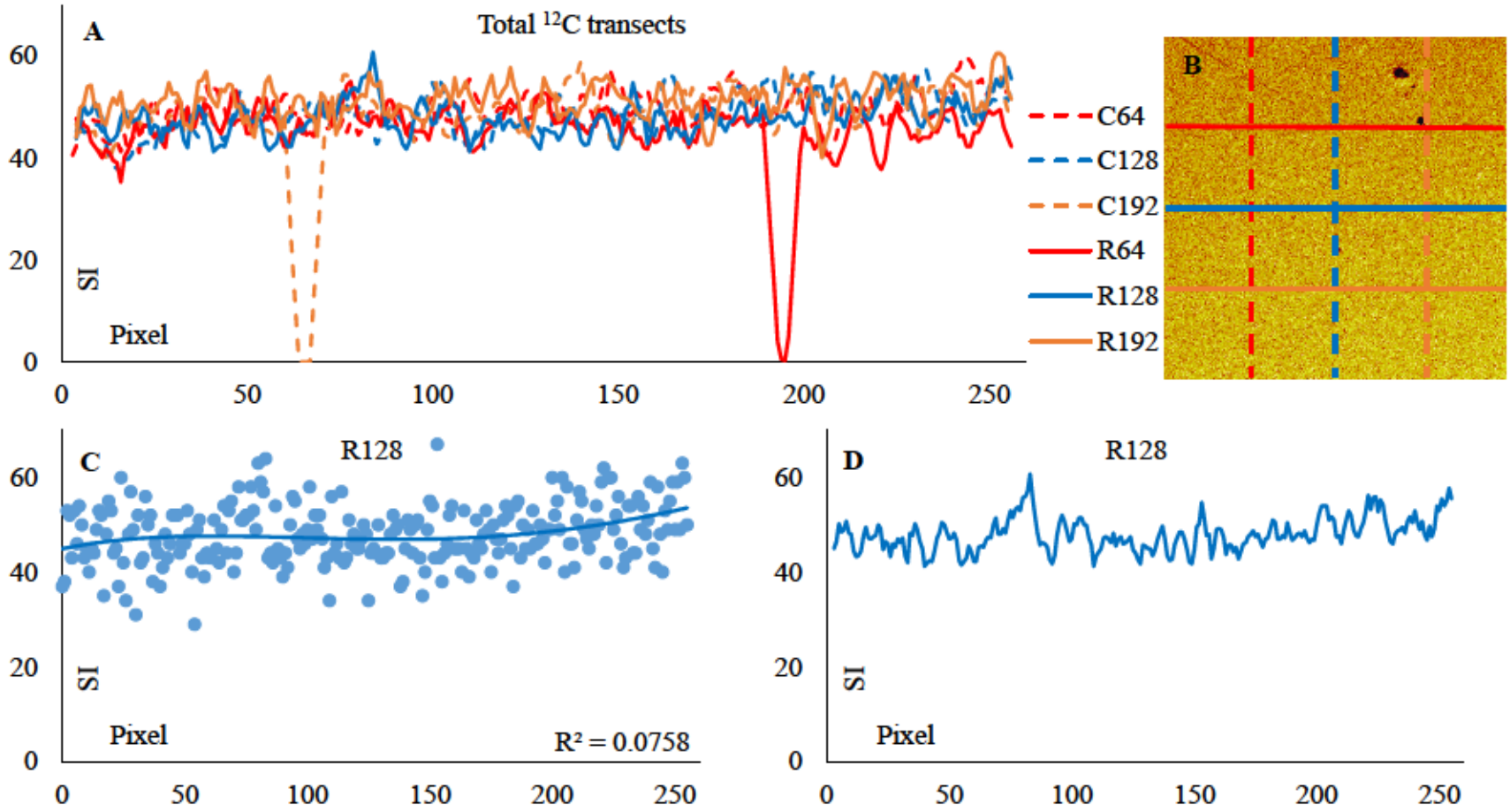


Figure 9. Diamond SL-1 window-1 $^{12}$C analysis. A shows 4$^{th}$ order moving average polylines of row and column transects. B shows the $^{12}$C element map with transects. C shows the raw data of row 128 transect with a 4$^{th}$ order polynomial best fit line and $R^2$ value. D shows the moving average polyline of data from row 128. Y-axis is Signal Intensity (SI).

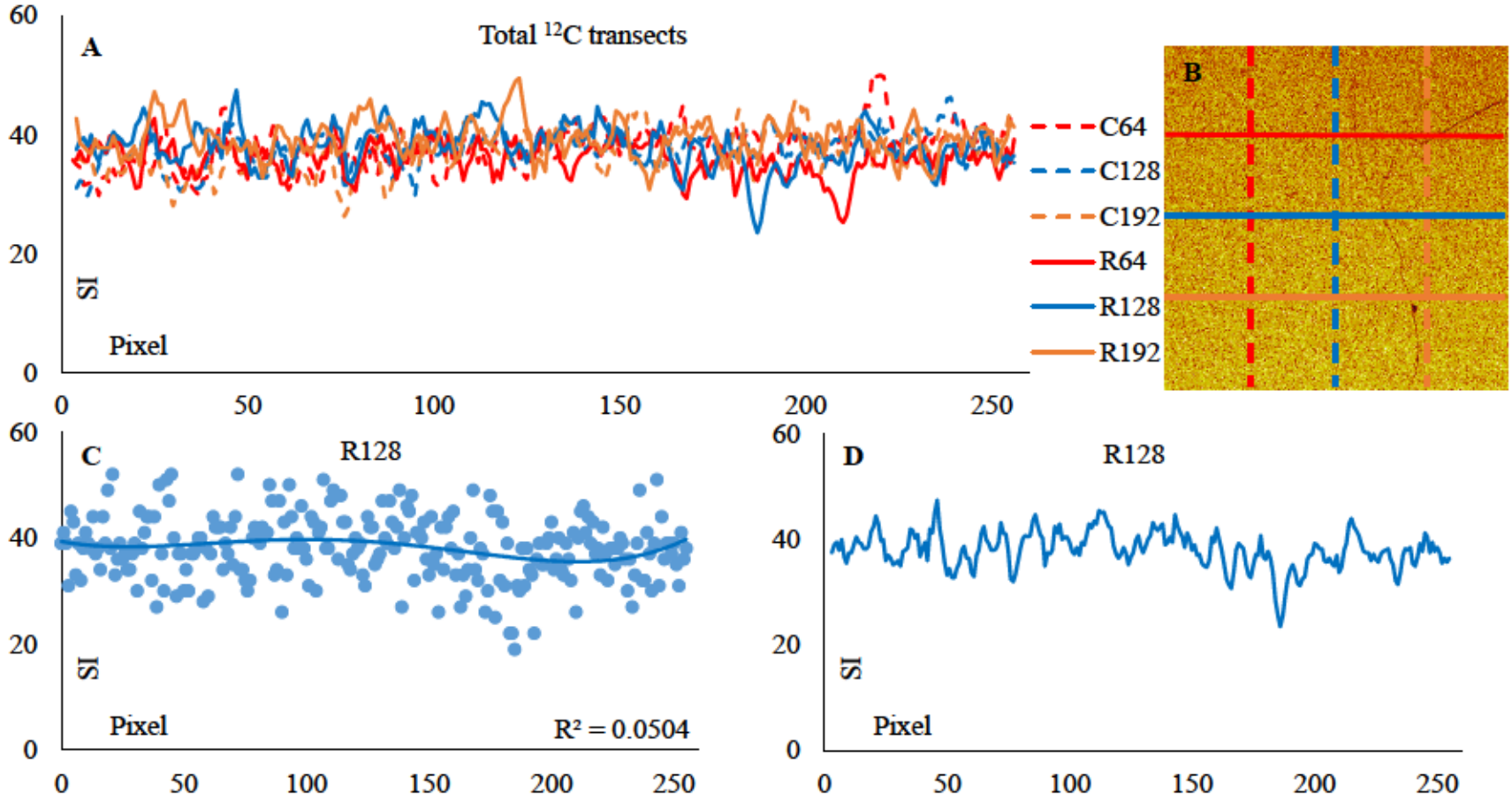


Figure 10. Diamond SL-1 window-2 $^{12}$C analysis. A shows 4$^{th}$ order moving average polylines of row and column transects. B shows the $^{12}$C element map with transects. C shows the raw data of row 128 transect with a 4$^{th}$ order polynomial best fit line and $R^2$ value. D shows the moving average polyline of data from row 128. Y-axis is Signal Intensity (SI).

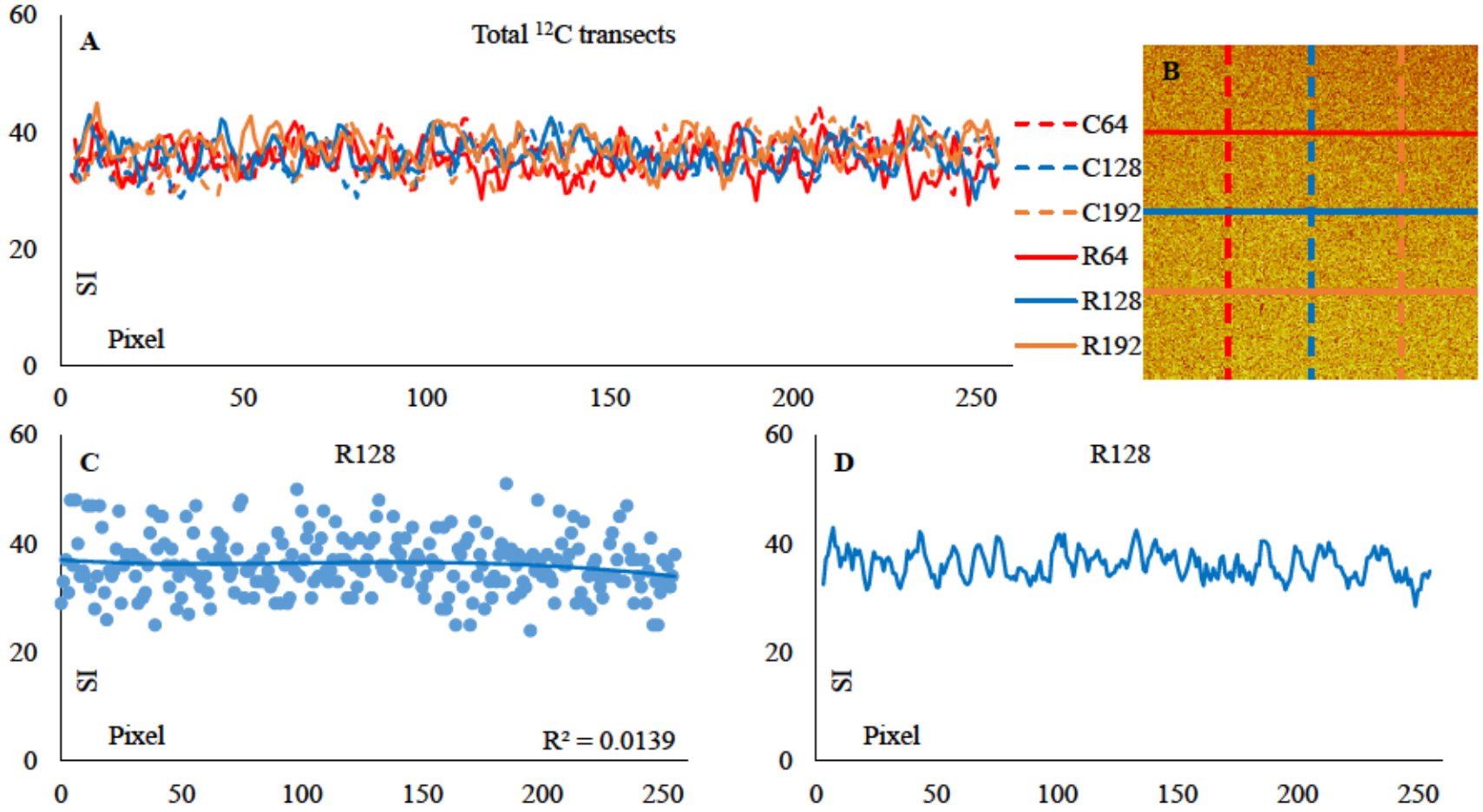


Figure 11. Diamond SL-1 window-3 $^{12}C$ analysis. A shows 4$^{th}$ order moving average polylines of row and column transects. B shows the $^{12}C$ element map with transects. C shows the raw data of row 128 transect with a 4$^{th}$ order polynomial best fit line and $R^2$ value. D shows the moving average polyline of data from row 128. Y-axis is Signal Intensity (SI).

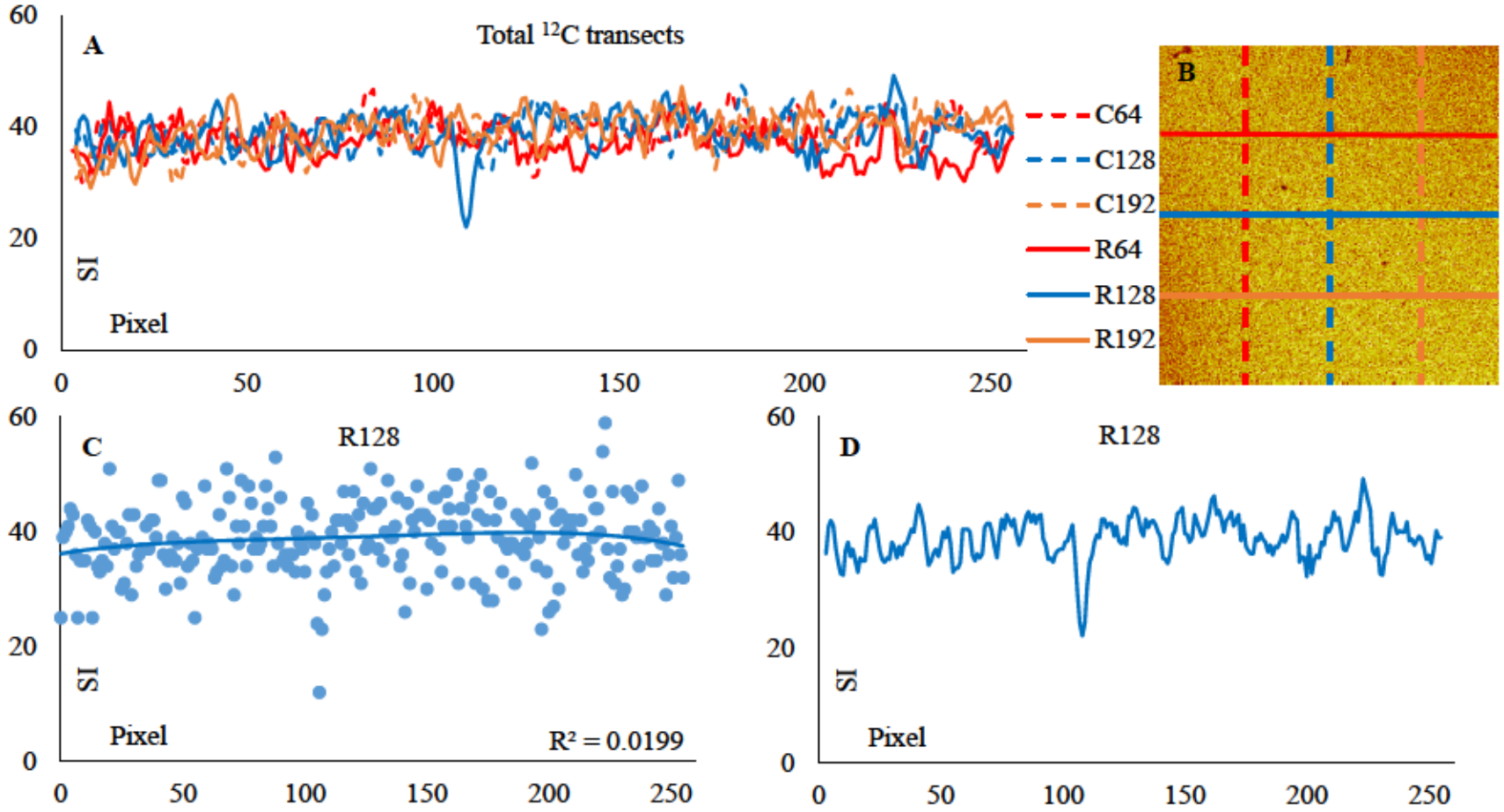


Figure 12. Diamond SL-1 window-4 $^{12}$C analysis. A shows 4$^{th}$ order moving average polylines of row and column transects. B shows the $^{12}$C element map with transects. C shows the raw data of row 128 transect with a 4$^{th}$ order polynomial best fit line and $R^2$ value. D shows the moving average polyline of data from row 128. Y-axis is Signal Intensity (SI).

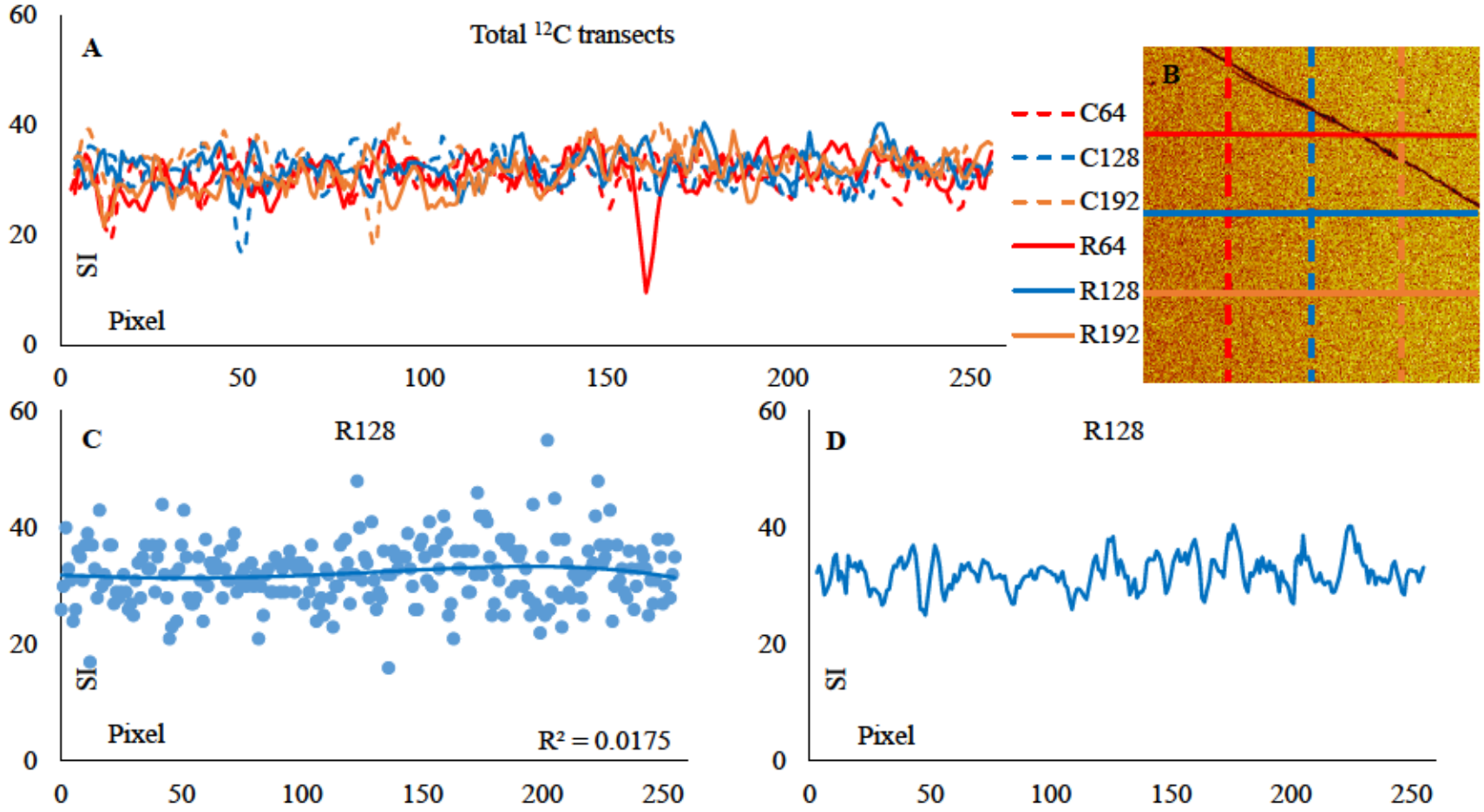


Figure 13. Diamond SL-1 window-5 $^{12}C$ analysis. A shows 4$^{th}$ order moving average polylines of row and column transects. B shows the $^{12}C$ element map with transects. C shows the raw data of row 128 transect with a 4$^{th}$ order polynomial best fit line and $R^2$ value. D shows the moving average polyline of data from row 128. Y-axis is Signal Intensity (SI).

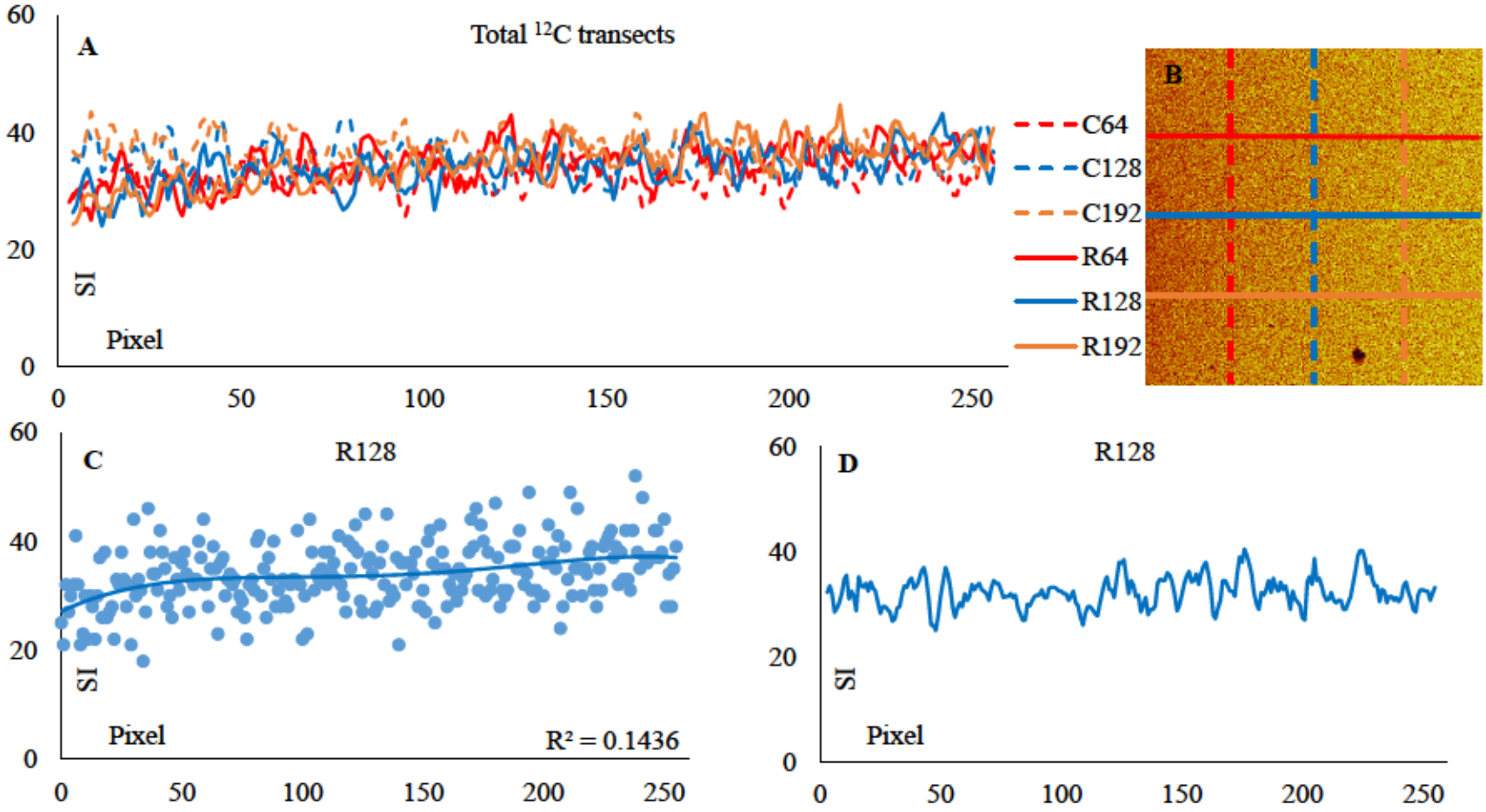


Figure 14. Diamond SL-1 window-6 $^{12}$C analysis. A shows 4$^{th}$ order moving average polylines of row and column transects. B shows the $^{12}$C element map with transects. C shows the raw data of row 128 transect with a 4$^{th}$ order polynomial best fit line and $R^2$ value. D shows the moving average polyline of data from row 128. Y-axis is Signal Intensity (SI).

of the anion analysis windows ranged from 7.9 to 9.5 million. Total cation counts ranged from 35.3 to 68.5 million.

Window-26. $^{12}C$ within window-26 shows multiple mineral inclusions with a concave-up linear feature above R64 (Figure 15b). This linear feature dominates the top section with mineral inclusions diffuse throughout the center portion of the element map. The main body of the diamond is homogenous with an average $^{12}C$ SI with 2σ error 33 ± 5.5. C192 intercepts the linear feature around pixel 55, however shows little change outside of the variation of the whole element map within C192 (Figure 15a). C128 also intercepts this feature around pixel 32 and shows a similar $^{12}C$ SI association (Figure 15a). No mineral inclusion is intercepted by the standard transect format. However, $^{12}C$ SI within data used to plot Figure 15b shows SI dropping to 0.

Window-28. $^{12}C$ within window-28 shows a 109 µm subhedral cubic mineral inclusion in the top left of the element map (Figure 16b). This window potentially has surficial polishing errors below R192 of the analysis window. Near the central portion of the analysis window appears to be a string of mineral inclusions or pockets in the diamond surface. The body of the analysis window shows gradational $^{12}C$ SI increase from left to right (Figure 16b). A transect of this cubic mineral shows zonation of $^{12}C$ (Figure 16a). Over 10 µm, a 90% increase from the first zone of depleted $^{12}C$ SI to a zone of high $^{12}C$ SI is observed. This zone of high $^{12}C$ SI plateaus with 2σ error 23 ± 1.1 for 23 µm before decreasing to 0 $^{12}C$ SI over 15.6 µm. $^{12}C$ SI within this inclusions 2$^{nd}$ zone of depleted $^{12}C$ increases to the homogenous $^{12}C$ SI after remaining at 0 for 22 µm (Figure 16a). The main body of $^{12}C$ generally increases from left to right in R transects. R128 4$^{th}$ order polynomial measures a gradual 29.6% increase over 342 µm in $^{12}C$ SI (Figure 16c). All linear features and mineral inclusion show SI highs in the $^{16}O$ element map.

Window-29. $^{12}C$ within window-29 shows a stepwise SI response in the $^{12}C$ element map (Figure 17b). This window includes diffuse multi-phase small mineral inclusions. 4$^{th}$ order polynomial line shows the SI stepwise change from left to right (Figure 17c). This stepwise change is shown by regions of rates of change to $^{12}C$ SI. These three regions can be seen in Figure 17c from pixel 0 to 88, 89 to 200 and 201 to 255. Within these regions, region 0 to 88 has a rate of change 0.32 $^{SI}/_{pixel}$, region 89 to 200 has a rate of change 0.23 $^{SI}/_{pixel}$ and region 201 to 255 has a rate of change 0.54 $^{SI}/_{pixel}$. The mineral inclusions are not intercepted by any standard transects. These inclusions are all $\leq$ 20 µm. Inclusions appear to be multi-phase with inclusions south of R128 showing highs in the Fe and Na element maps. While inclusions above R128 show highs in Al and Si element maps. Both populations appear as highs in $^{16}O$ maps.

Window-30. $^{12}C$ within window-30 shows systematic gradual increase from left to right with a jagged linear feature in the far left half the element map and multi-phase mineral inclusions. These mineral inclusions are intercepted by R64 and R192 (Figure 18a). The silicate mineral inclusion intercepted by R64 shows a 77% $^{12}C$ SI decrease over 7.8 µm (Figure 18a) with element maps for Al, Mg, Na and Si showing local highs in SI. The mineral inclusion intercepted by R192 shows a 34% $^{12}C$ SI decrease over 19.5 µm (Figure 18a) this inclusion has minor highs in the Ca, Fe and Mg element maps. Another mineral inclusion just below R128 in the right half of Figure 18b shows high SI in the $^{16}O$ map and a minor peak in the OH element map. However, this inclusion has no cation component in the cation maps. R128 shows the systematic $^{12}C$ SI from left to right (Figure 18c). The rate of change to $^{12}C$ SI is consistent in the 4$^{th}$ order polynomial with 11.6% increase from left to right in $^{12}C$ SI (Figure 18c).

Window-31. $^{12}C$ within window-31 shows systematic increase from left to right with multiple mineral inclusions and a linear feature below the R192 transect of the $^{12}C$ element map

(Figure 19b). This linear feature has multiple pockets of inclusions and was intercepted by C64, C128 and C192. The only inclusion intercepted was measured by R64. This inclusion shows little cation SI, but high SI in the oxygen and hydrogen element maps. R64 measured an 86.7% decrease over 13.6 μm of $^{12}C$ SI (Figure 19a). The main body of diamond in this window systemically increases from left to right (Figure 19c). R128 4$^{th}$ order polynomial measures this change as a slightly concave down trend with a 25.7% increase (Figure 19c). The linear feature measured by C64 and C192 shows little variation in $^{12}C$ SI (Figure 19a). C128 intercepted a thicker portion of this feature and measured 46.7% decrease over 15.6 μm within $^{12}C$ SI (Figure 19a). All cation element maps show SI highs for this feature.

Window-32. $^{12}C$ within window-32 is dominantly a homogenous SI response with multiple small inclusions and one large subhedral rectangular mineral (Figure 20b). A linear feature with potential inclusions dominates the $^{12}C$ element map below the R192 transect. The subhedral rectangular mineral inclusion is intercepted by R128. The linear feature is intersected by C64, C128 and C192. However, transects do not measure significant change in C64 and C192 as shown by little variation in their 4$^{th}$ order moving average polylines (Figure 20a). R128 intersects a mineral inclusion that has relative highs in Fe, Mg and O element maps. R128 measures a 50% decrease over 22 μm in $^{12}C$ SI (Figure 20d). C128 intersects the linear feature near its widest dimension. This linear feature has high SI response in O, Na, Al, Mg, Ca and Si. C128 measures a 64% decrease over 19.5 μm in $^{12}C$ SI (Figure 20a). The main body of this window shows a homogenous $^{12}C$ SI response (Figure 20b). R64 measures an average $^{12}C$ SI response with 2σ error of 31 ± 5.4.

Window-33. $^{12}C$ within window-33 shows a gradational increase from left to right with two mineral inclusions. One anhedral equant inclusion is intercepted by C128 (Figure 21b).

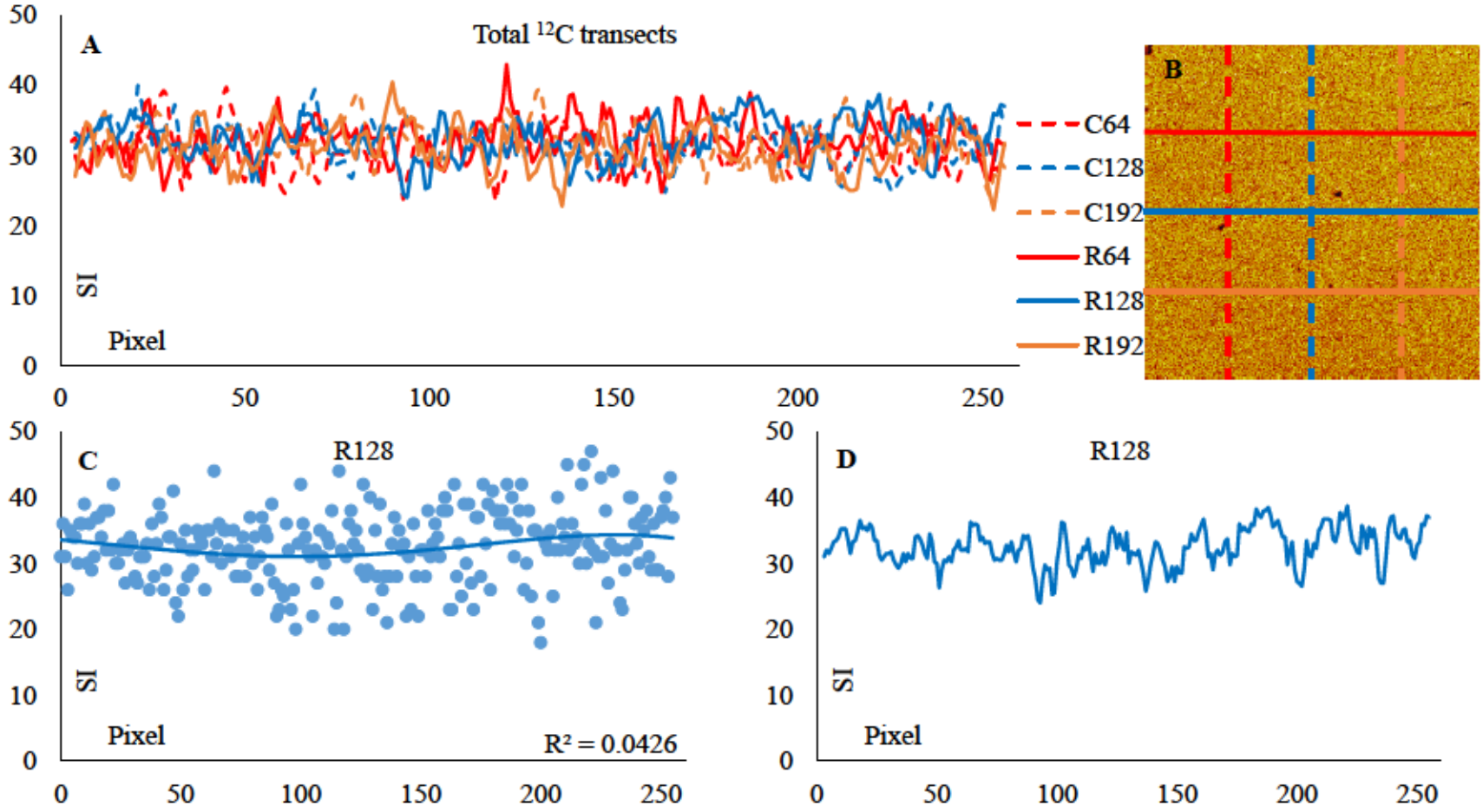


Figure 15. Diamond SL-2 window-26 $^{12}$C analysis. A shows 4$^{th}$ order moving average polylines of row and column transects. B shows the $^{12}$C element map with transects. C shows the raw data of row 128 transect with a 4$^{th}$ order polynomial best fit line and $R^2$ value. D shows the moving average polyline of data from row 128. Y-axis is Signal Intensity (SI).

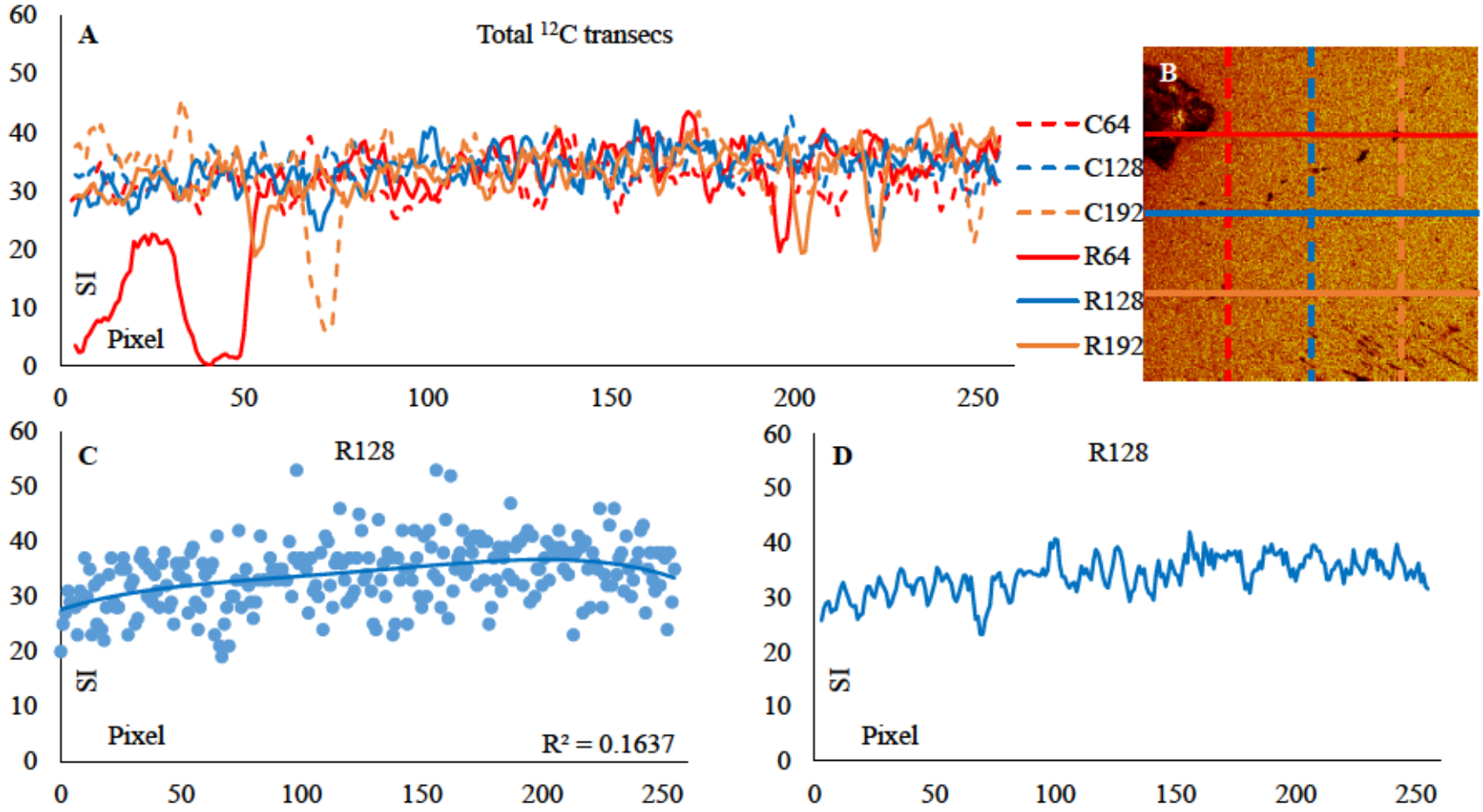


Figure 16. Diamond SL-2 window-28 $^{12}C$ analysis. A shows 4$^{th}$ order moving average polylines of row and column transects. B shows the $^{12}C$ element map with transects. C shows the raw data of row 128 transect with a 4$^{th}$ order polynomial best fit line and $R^2$ value. D shows the moving average polyline of data from row 128. Y-axis is Signal Intensity (SI).

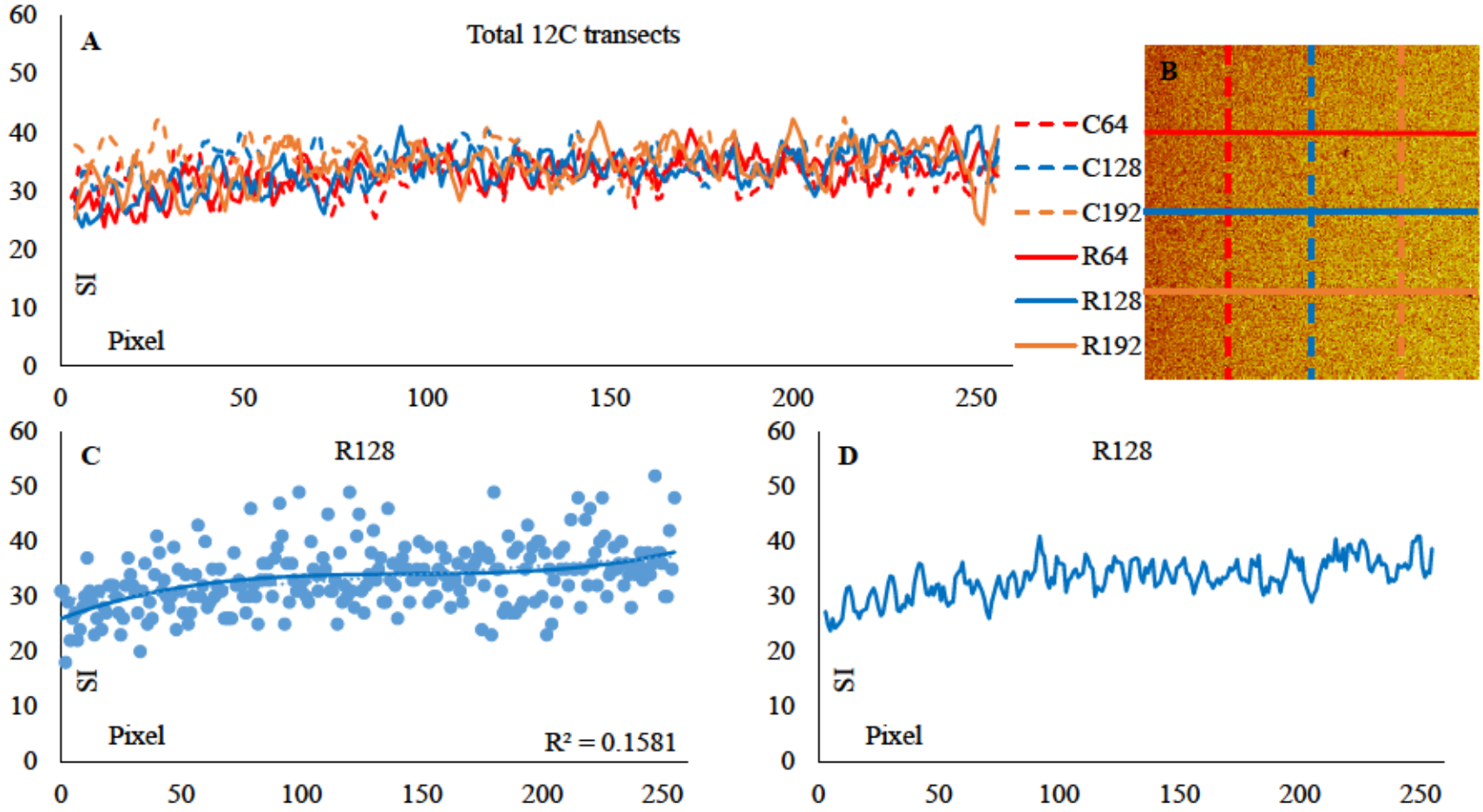


Figure 17. Diamond SL-2 window-29 $^{12}C$ analysis. A shows 4$^{th}$ order moving average polylines of row and column transects. B shows the $^{12}C$ element map with transects. C shows the raw data of row 128 transect with a 4$^{th}$ order polynomial best fit line and $R^2$ value. D shows the moving average polyline of data from row 128. Y-axis is Signal Intensity (SI).

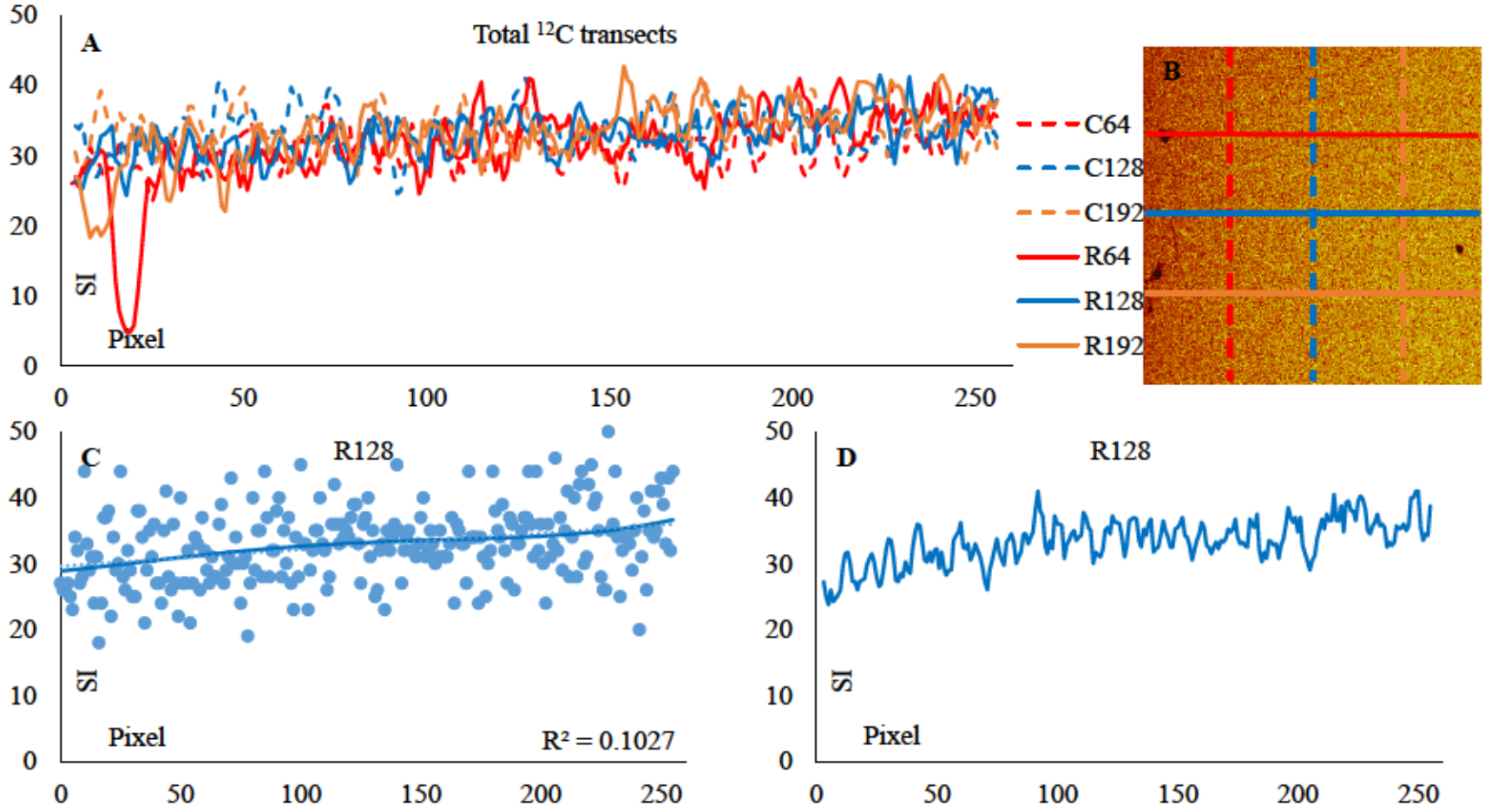


Figure 18. Diamond SL-2 window-30 $^{12}C$ analysis. A shows 4$^{th}$ order moving average polylines of row and column transects. B shows the $^{12}C$ element map with transects. C shows the raw data of row 128 transect with a 4$^{th}$ order polynomial best fit line and $R^2$ value. D shows the moving average polyline of data from row 128. Y-axis is Signal Intensity (SI).

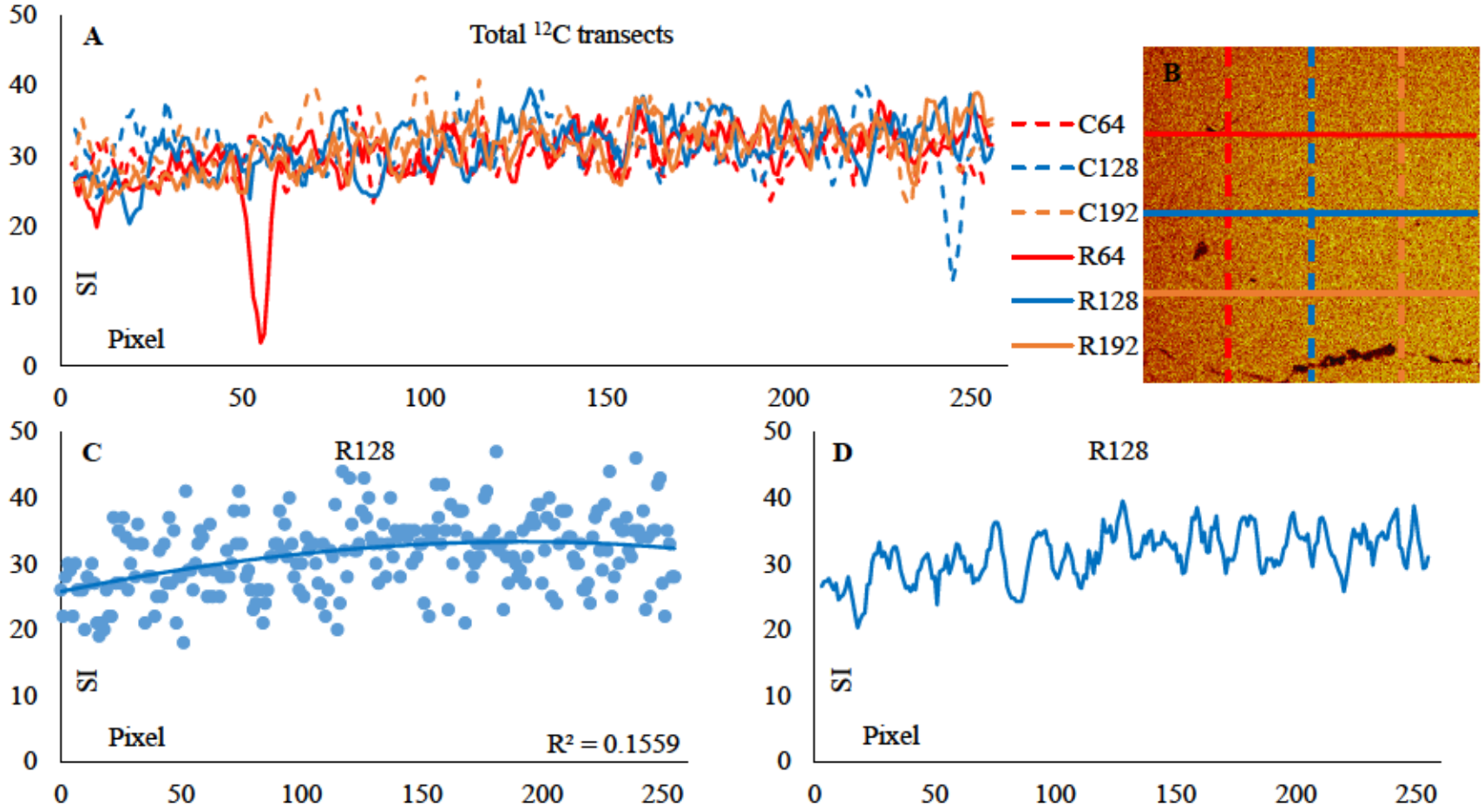


Figure 19. Diamond SL-2 window-31 $^{12}$C analysis. A shows 4$^{th}$ order moving average polylines of row and column transects. B shows the $^{12}$C element map with transects. C shows the raw data of row 128 transect with a 4$^{th}$ order polynomial best fit line and $R^2$ value. D shows the moving average polyline of data from row 128. Y-axis is Signal Intensity (SI).

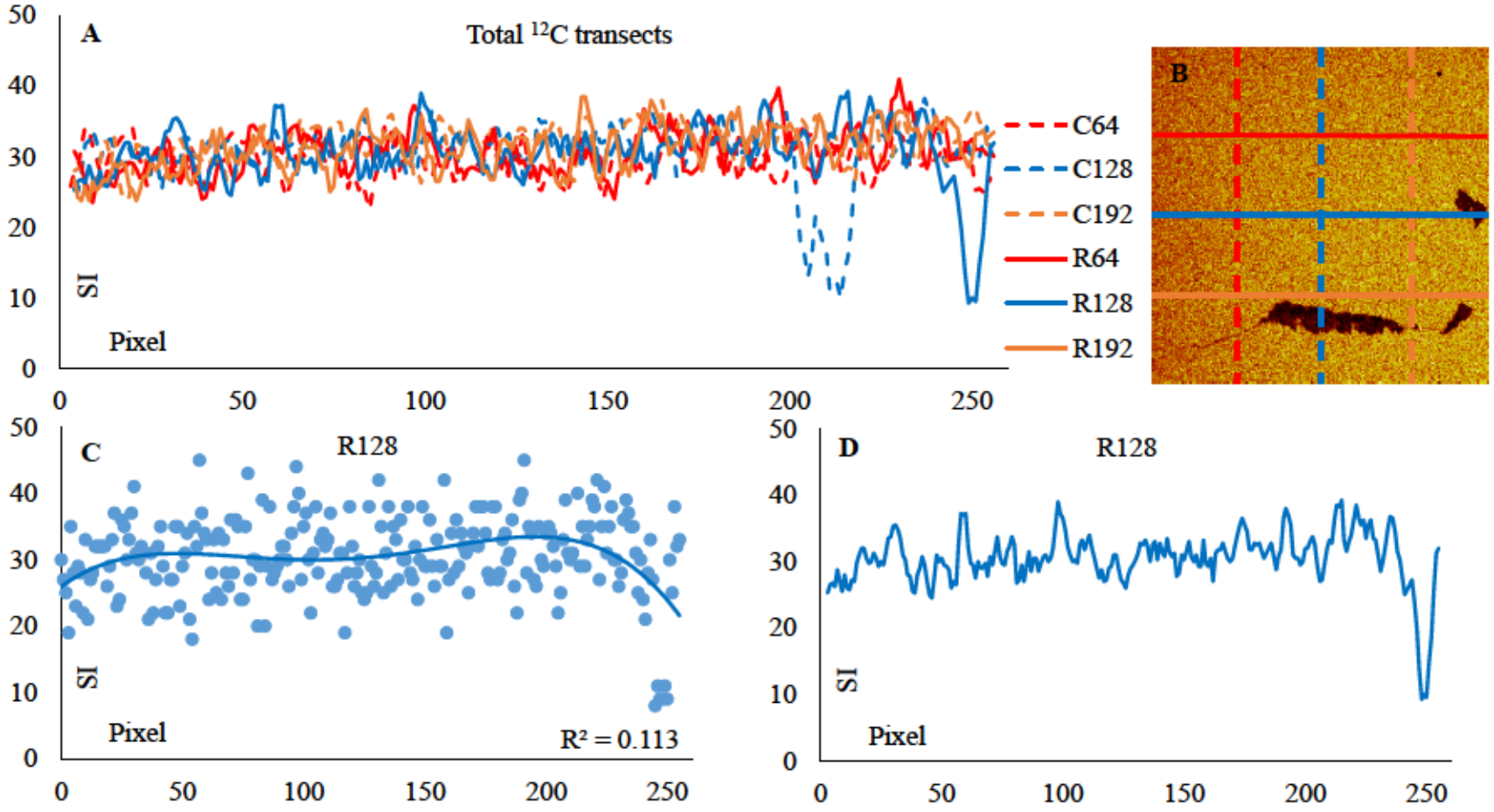


Figure 20. Diamond SL-2 window-32 $^{12}$C analysis. A shows 4$^{th}$ order moving average polylines of row and column transects. B shows the $^{12}$C element map with transects. C shows the raw data of row 128 transect with a 4$^{th}$ order polynomial best fit line and $R^2$ value. D shows the moving average polyline of data from row 128. Y-axis is Signal Intensity (SI).

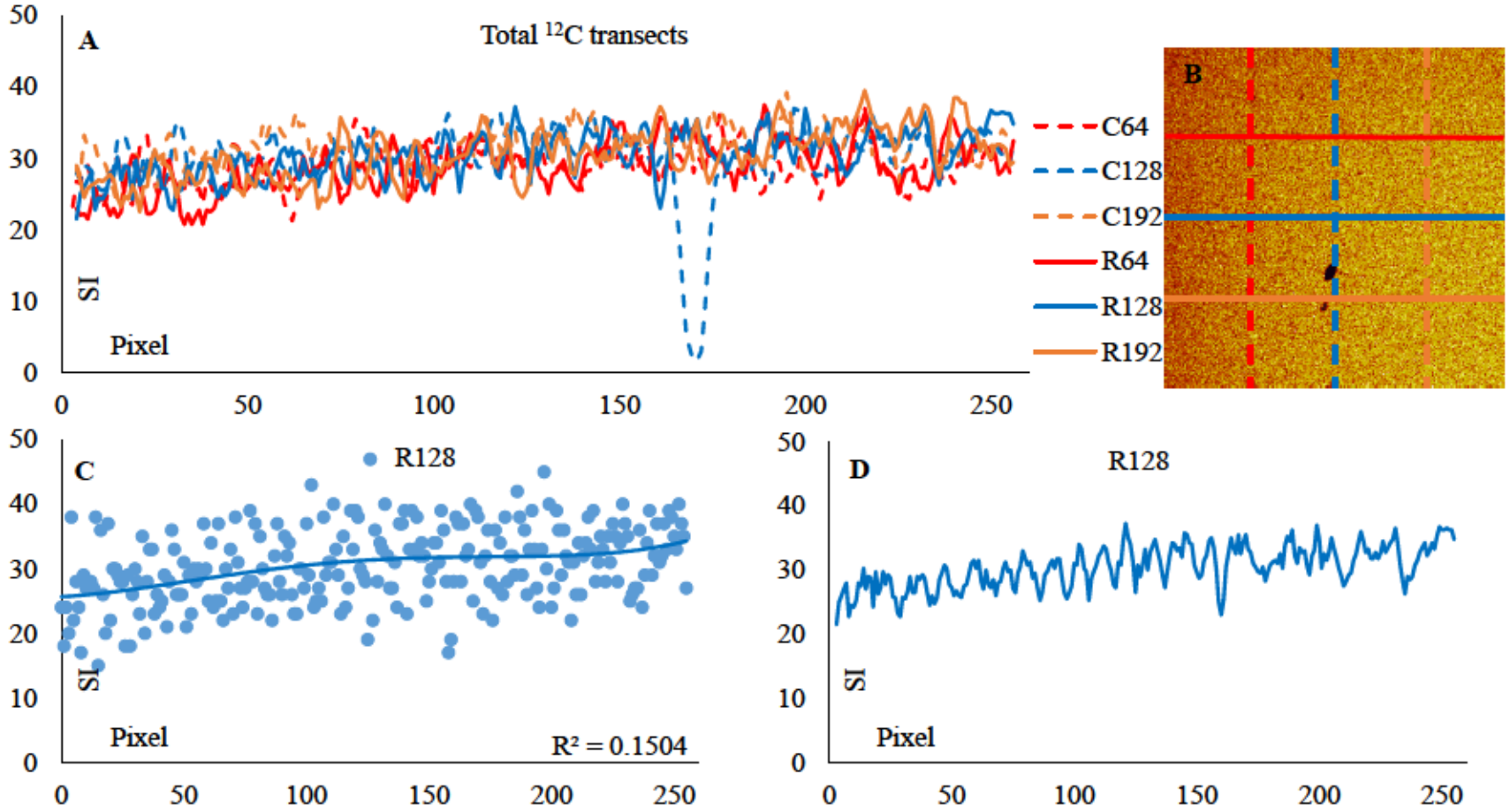


Figure 21. Diamond SL-2 window-33 $^{12}C$ analysis. A shows 4$^{th}$ order moving average polylines of row and column transects. B shows the $^{12}C$ element map with transects. C shows the raw data of row 128 transect with a 4$^{th}$ order polynomial best fit line and $R^2$ value. D shows the moving average polyline of data from row 128. Y-axis is Signal Intensity (SI).

Fourth order moving average polyline of C128 shows a 92.8% decrease over 13.7 μm in $^{12}C$ SI (Figure 21a). This mineral inclusion has minor highs in the Al, Fe, Mg and Si maps. Gradational increase from left to right is measured by R128 4$^{th}$ order polynomial (Figure 21c). R128 shows a 35.1% increase from left to right in $^{12}C$ SI.

**SL-4.** ToF-SIMS analysis of diamond SL-4 included six anion windows: window-0, window-1, window-2, window-3, window-4 and window-5 with analysis windows of 500 μm$^2$. Cation analysis was done on window-4 in the same analysis window. Anion analysis of each window took an average of 32.8 minutes with the cation analysis of window-4 taking 10 minutes. Total counts of anion analysis ranged from 10.0 to 0.6 million. Total counts of the window-4 cation analysis was 47.7 million.

Window-0. $^{12}C$ within window-0 shows a gradational decrease from left to right with multiple clusters of pockets void of $^{12}C$ SI (Figure 22b). These pockets show no $^{16}O$ SI. Instead, these pockets show minor highs in the H element maps. One of these pockets void of $^{12}C$ was intersected by R192 (Figure 22a and 22b). R192 measures a 69.2% decrease in $^{12}C$ SI over 13.7 μm (Figure 22a). R128 4$^{th}$ order polynomial measures a 20.6% decrease from left to right over the entire transect (Figure 22c). R128 shows an average value of $^{12}C$ SI with 2σ error 27 ± 5.6. The 4$^{th}$ order moving average plot shows the data is well constrained to the average value with a minimal decrease to $^{12}C$ SI (Figure 22d).

Window-1. $^{12}C$ within window-1 shows a homogenous SI with multiple voids (Figure 23b). These voids show little SI in the $^{16}O$ element map. However, these voids do show as local SI highs in the H element map. These voids are intersected by C64 and R128 (Figure 23a). C64 intersects one void measuring a 92.3% decrease over 15.6 μm (Figure 23a). R128 intersects two voids at pixel 27 and 180. The void at pixel 27 measures an 80% decrease over 11.7 μm and the

void at pixel 180 measures a 73.7% decrease over 9.8 µm (Figure 23c). R64 measures the main body of window-1 $^{12}C$ SI with an average value with 2σ error of 22 ± 4.1.

Window-2. $^{12}C$ within window-2 shows a homogenous SI with multiple inclusions (Figure 24b). Inclusions include two populations that show $^{16}O$ or H SI highs. An inclusion showing high $^{16}O$ is intersected by C128 and R192 (Figure 24a). C128 measures a 60% decrease in $^{12}C$ SI over 9.8 µm (Figure 24a). R192 measures a different portion of the same inclusion with a 25% decrease in $^{12}C$ SI over 7.8 µm (Figure 24a). The homogenous body is measured by R128 (Figure 24c). R128 measures the main body of window-2 $^{12}C$ SI with an average value 2σ error of 18 ± 4.1.

Window-3. $^{12}C$ within window-3 shows a homogenous SI with multiple inclusions (Figure 25b). These inclusions show minimal highs in SI for $^{16}O$ and H element maps. Inclusions are intersected by R64 and R128 (Figure 25a and 25d). R64 measures a 43.6% decrease in $^{12}C$ SI over 9.8 µm (Figure 25a). R128 measures a 93.7% decrease in $^{12}C$ SI over 19.5 µm (Figure 25d). R192 measures the main body of window-3 $^{12}C$ SI with an average value with 2σ error of 13 ± 3.4 (Figure 25c).

Window-4. $^{12}C$ within window-4 shows a homogenous SI with multiple pockets of inclusions (Figure 26b). One inclusion approximately 72.3 µm wide was intersected by R64 and C192 (Figure 26a). R64 measures a 90.9% decrease in $^{12}C$ SI over 15.6 µm (Figure 26a). C192 measures a 91.7% decrease in $^{12}C$ SI over 11.7 µm (Figure 26a). R128 measures the main body of window-4 $^{12}C$ SI with an average value with 2σ error of 13 ± 3.7 (Figure 26c).

Window-5. $^{12}C$ within window-5 shows a homogenous SI with minimal inclusions (Figure 27b). These inclusions are not intercepted by standard transects (Figure 27a). R128

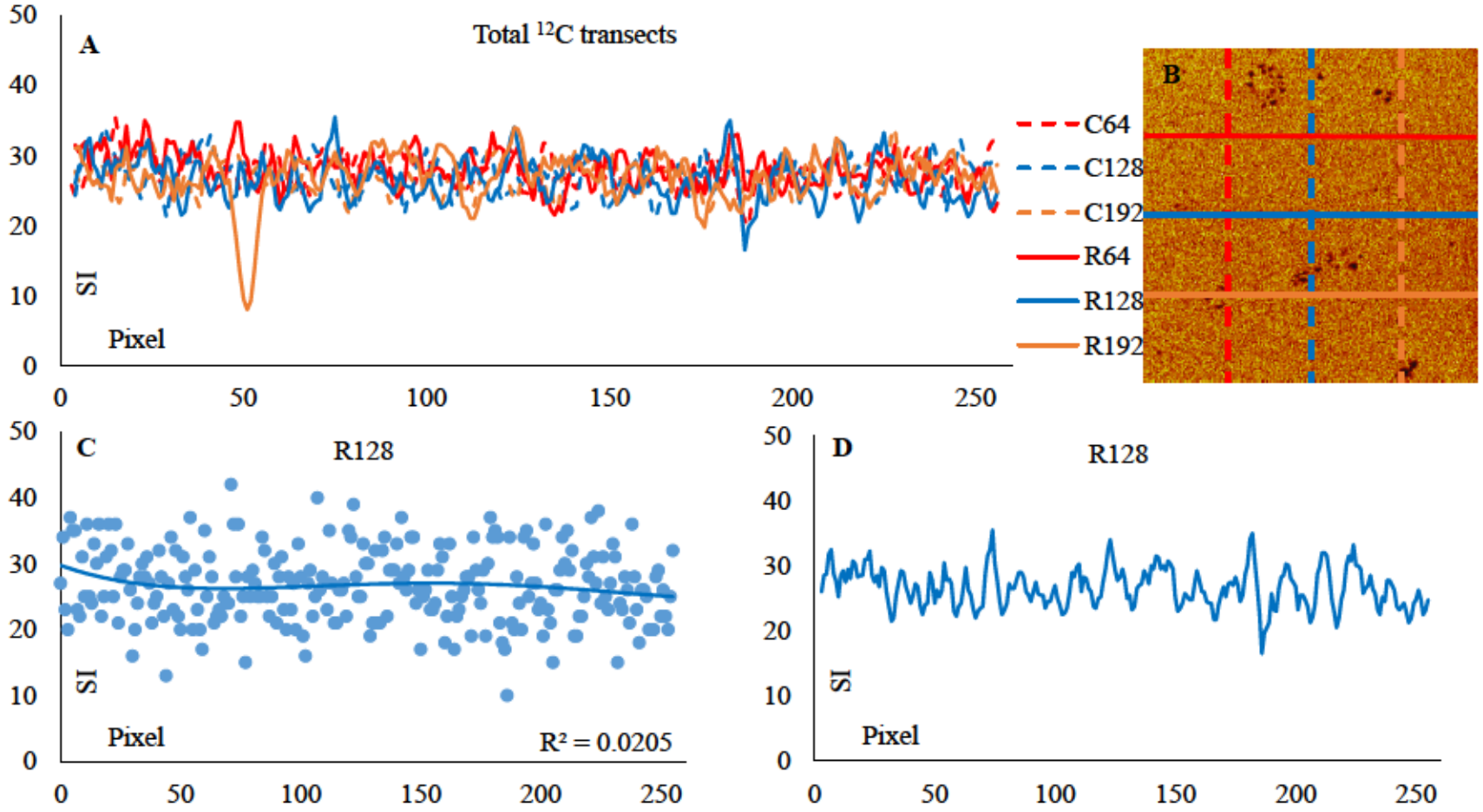


Figure 22. Diamond SL-4 window-0 $^{12}C$ analysis. A shows 4$^{th}$ order moving average polylines of row and column transects. B shows the $^{12}C$ element map with transects. C shows the raw data of row 128 transect with a 4$^{th}$ order polynomial best fit line and $R^2$ value. D shows the moving average polyline of data from row 128. Y-axis is Signal Intensity (SI).

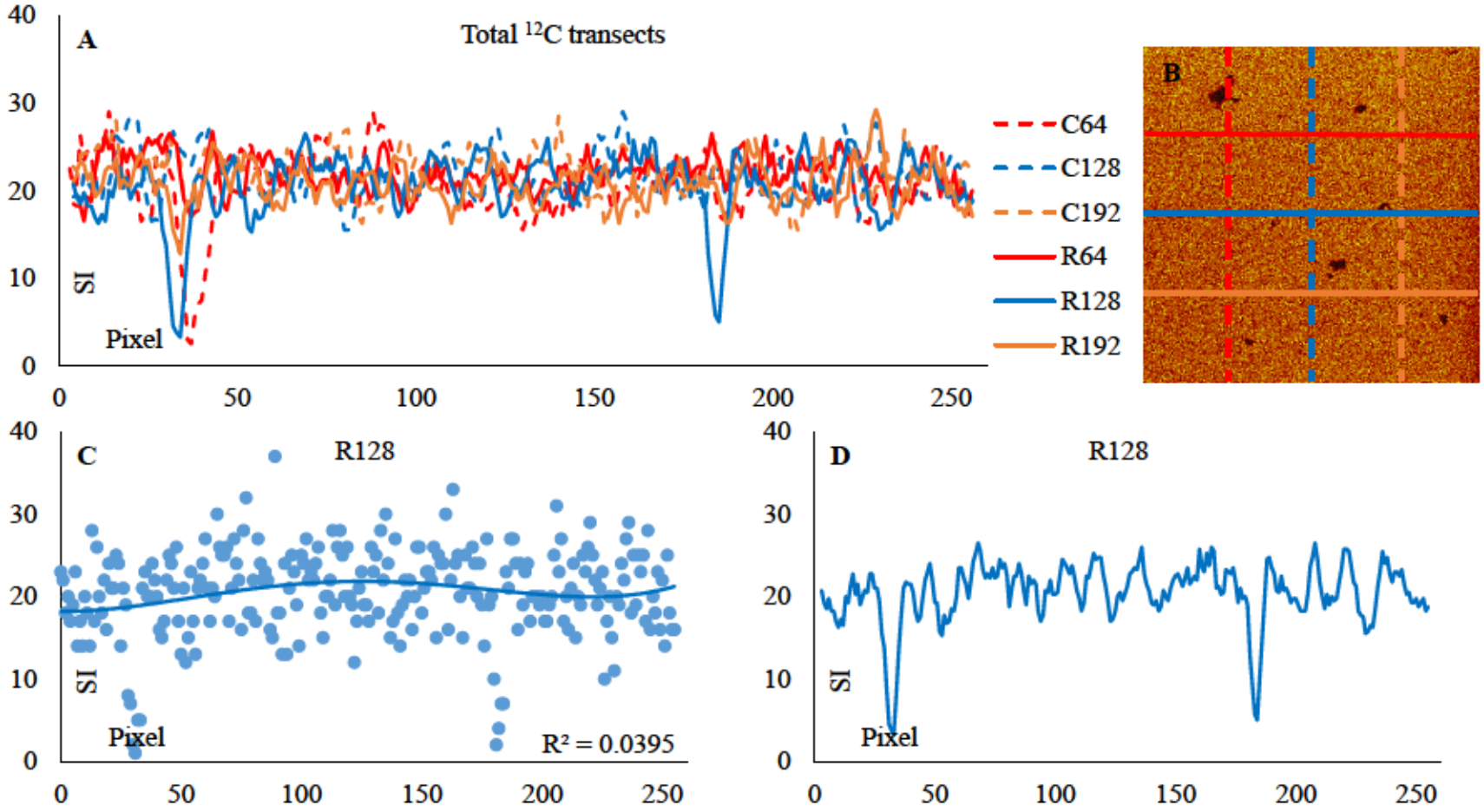


Figure 23. Diamond SL-4 window-1 $^{12}C$ analysis. A shows 4th order moving average polylines of row and column transects. B shows the $^{12}C$ element map with transects. C shows the raw data of row 128 transect with a 4th order polynomial best fit line and $R^2$ value. D shows the moving average polyline of data from row 128. Y-axis is Signal Intensity (SI).

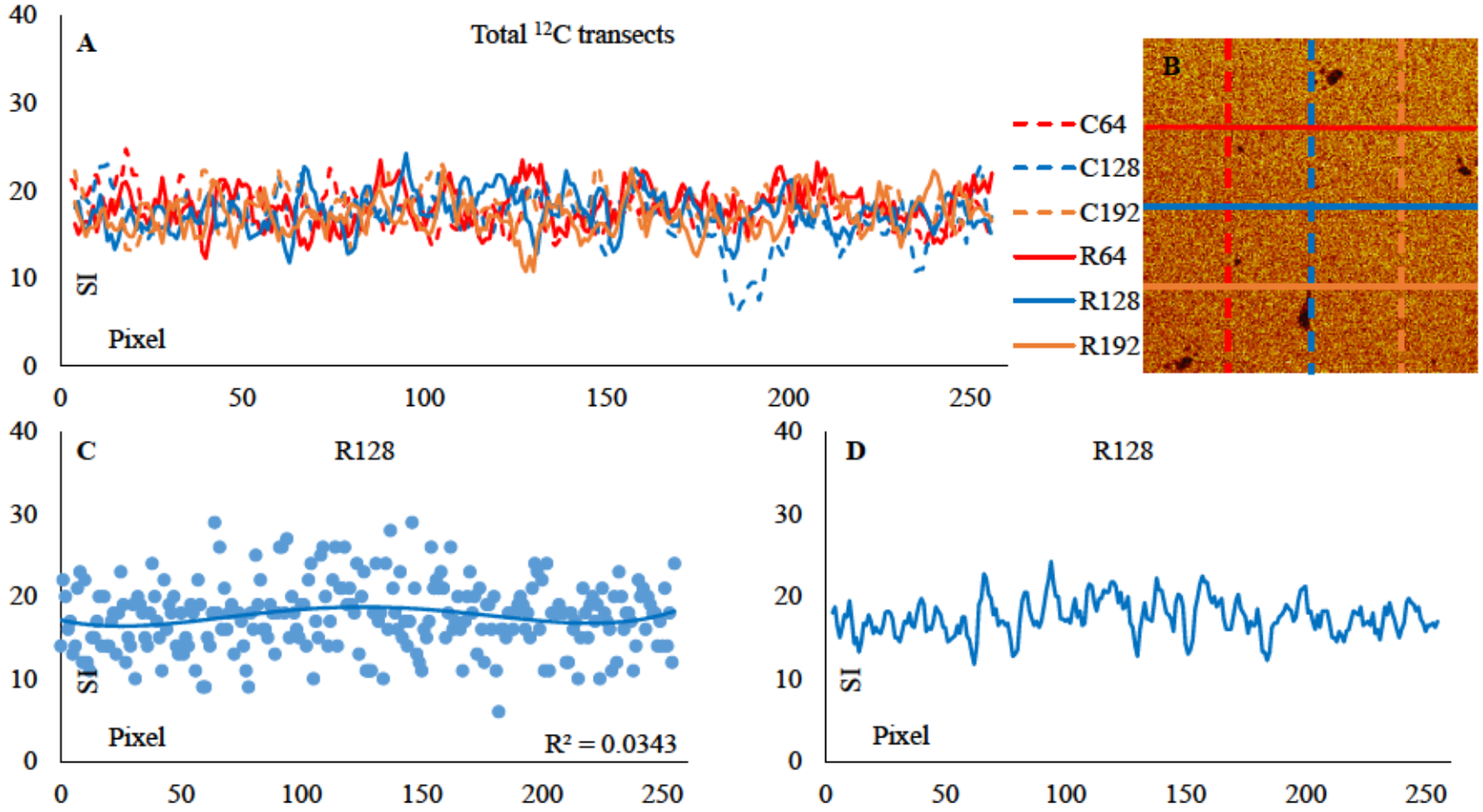


Figure 24. Diamond SL-4 window-2 $^{12}$C analysis. A shows 4$^{th}$ order moving average polylines of row and column transects. B shows the $^{12}$C element map with transects. C shows the raw data of row 128 transect with a 4$^{th}$ order polynomial best fit line and $R^2$ value. D shows the moving average polyline of data from row 128. Y-axis is Signal Intensity (SI).

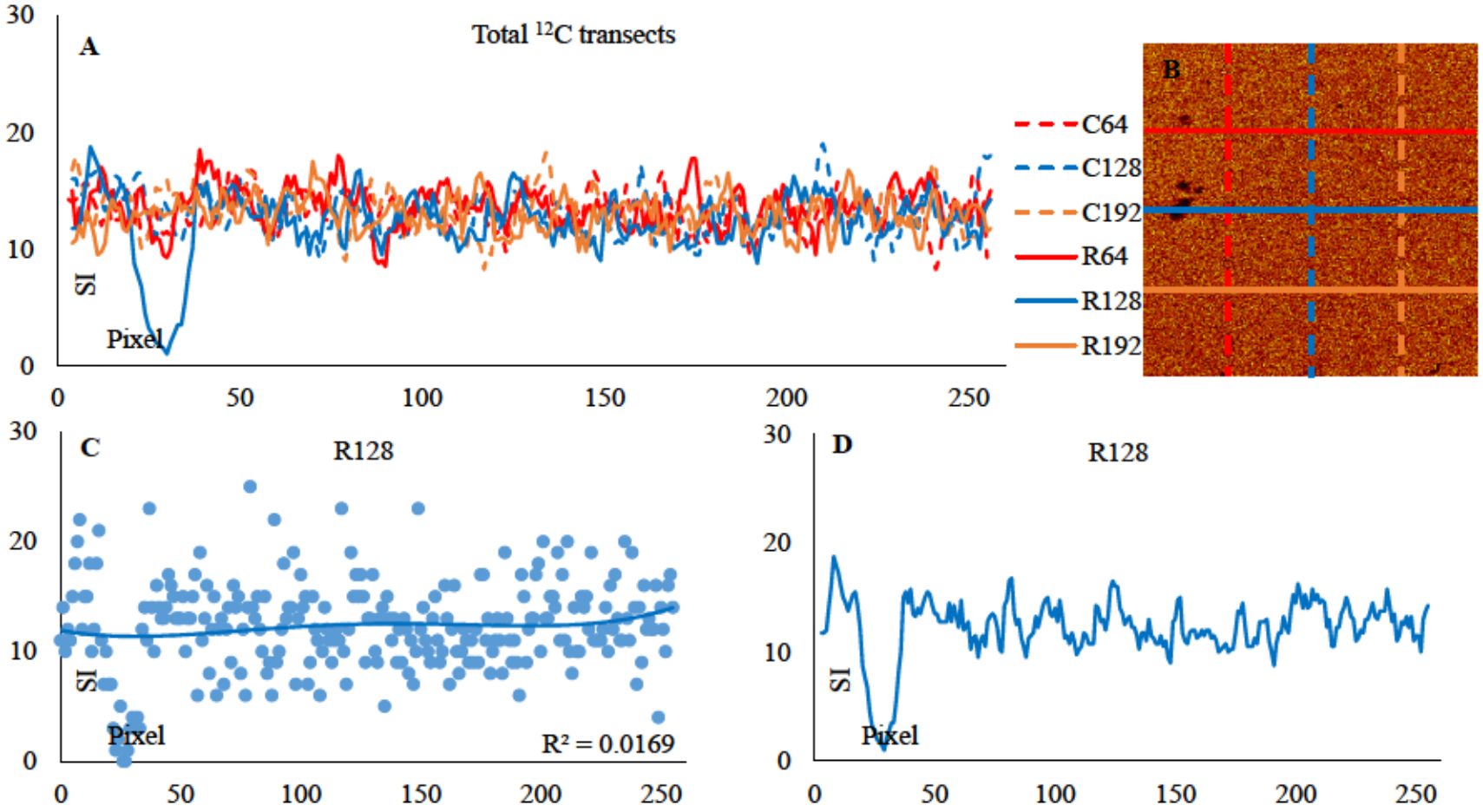


Figure 25. Diamond SL-4 window-3 $^{12}C$ analysis. A shows 4$^{th}$ order moving average polylines of row and column transects. B shows the $^{12}C$ element map with transects. C shows the raw data of row 128 transect with a 4$^{th}$ order polynomial best fit line and $R^2$ value. D shows the moving average polyline of data from row 128. Y-axis is Signal Intensity (SI).

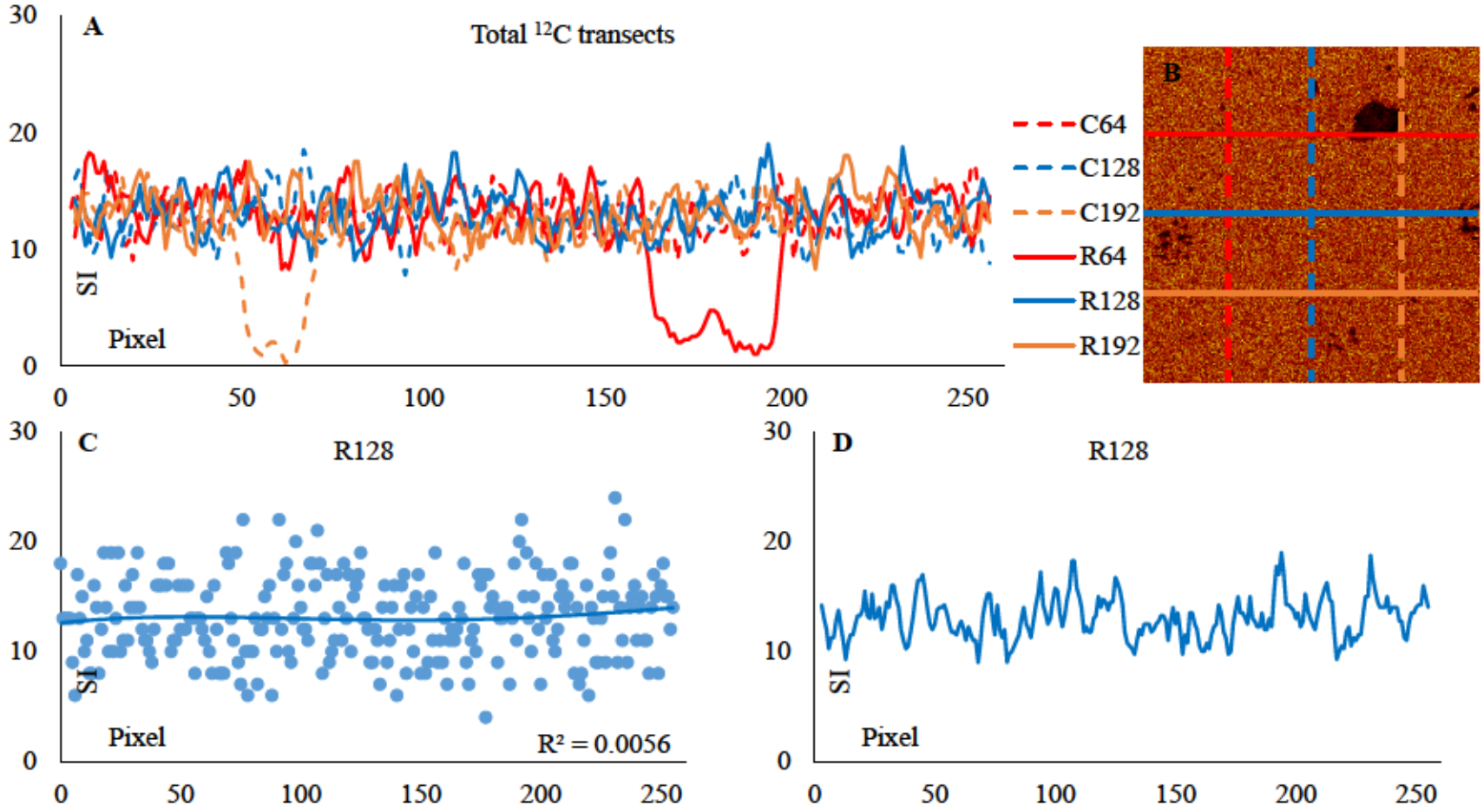


Figure 26. Diamond SL-4 window-4 $^{12}$C analysis. A shows 4$^{th}$ order moving average polylines of row and column transects. B shows the $^{12}$C element map with transects. C shows the raw data of row 128 transect with a 4$^{th}$ order polynomial best fit line and $R^2$ value. D shows the moving average polyline of data from row 128. Y-axis is Signal Intensity (SI).

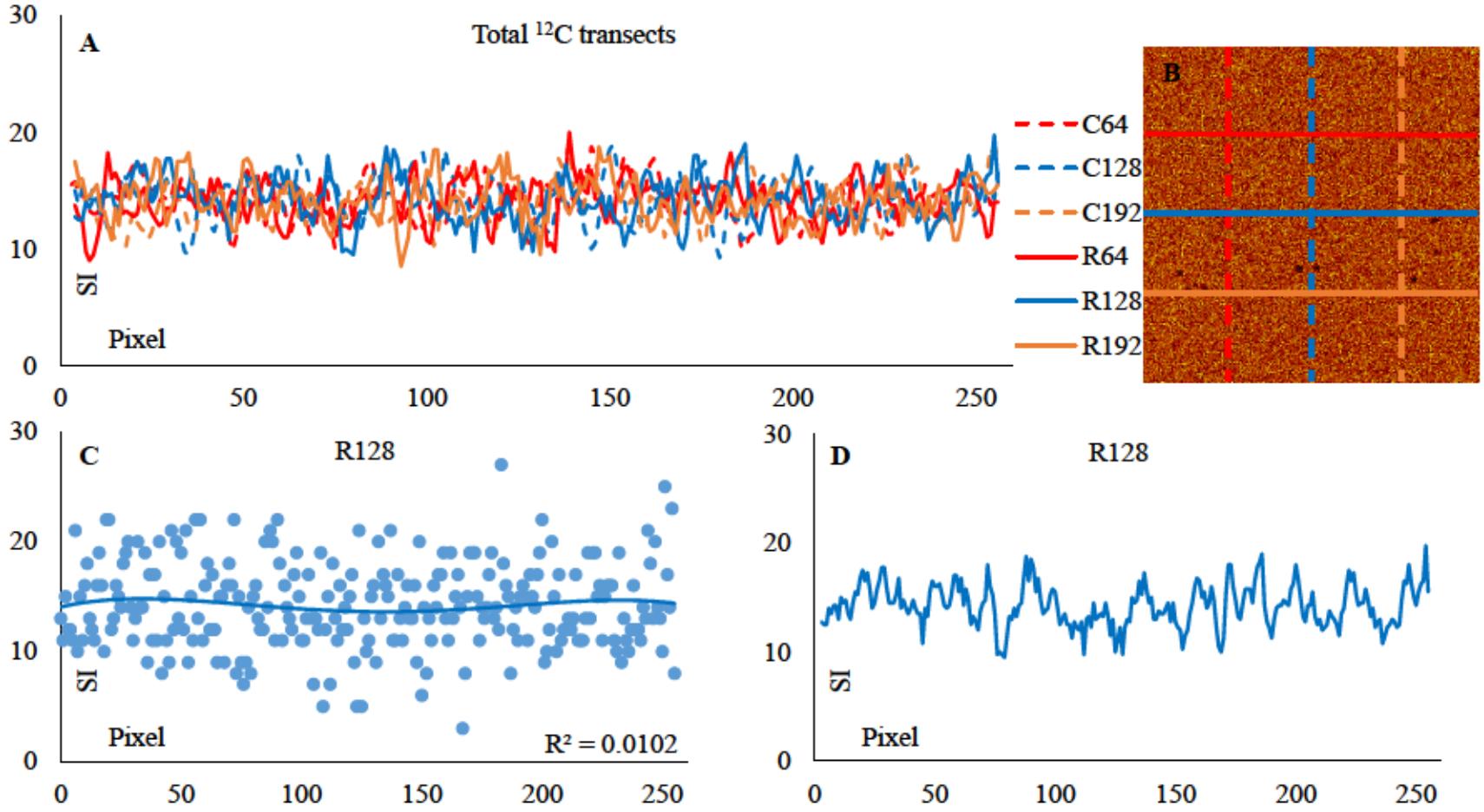


Figure 27. Diamond SL-4 window-5 $^{12}C$ analysis. A shows 4$^{th}$ order moving average polylines of row and column transects. B shows the $^{12}C$ element map with transects. C shows the raw data of row 128 transect with a 4$^{th}$ order polynomial best fit line and $R^2$ value. D shows the moving average polyline of data from row 128. Y-axis is Signal Intensity (SI).

measures the main body of window-4 $^{12}C$ SI with an average value with 2σ error of 14 ± 4.0 (Figure 27c).

**SL-3 and SL-5.** ToF-SIMS analysis of diamonds SL-3 and SL-5 proved to be trivial. Each diamond was imaged and showed linear or crack features spanning entire analysis windows (Figure 28). Diamond SL-3 showed significant affinity for these surficial errors. As such, the data was not post-processed after analysis. SL-5 is considered representative of these errors. ToF-SIMS analysis of diamond SL-5 included five anion windows: window-0, window-1, window-2, window-3 and window-4 with analysis windows of 500 $\mu m^2$. Anion analysis of each window took an average of 23.8 minutes. Total counts of anion analysis ranged from 8.5 to 8.8 million. Window-0, window-1, window-2 and window-4 all show significant linear features that are low or void in $^{12}C$ SI (Figure 28a, 28b, 28c and 28f). Linear features that are void in $^{12}C$ SI also show high $^{16}O$ SI (Figure 28e). This relationship is also true of window-3 (Figure 28d) where these linear features are not present but multiple dendritic cracks are observed. Zooming in on linear trends in window-1 and window-4 (Figure 28b and 28f) a 2$^{nd}$ set of lineations are observed. This 2$^{nd}$ set of lineations is marked by high $^{12}C$ SI. The intersection of these lineations makes rhombohedral shapes in $^{12}C$ SI element maps (Figure 28b - SE section).

**AR and SL-2 Additional ToF-SIMS Analysis**

General element mapping of AR and SL-2 showed the homogeneity of $^{12}C$ SI response in AR (Figure 3, 4, 5 and 6) also the large subhedral mineral inclusion in SL-2 window-28 (Figure 16). All windows of AR were analyzed for $^{13}C/^{12}C$ SI for each window along the same $^{12}C$ transects. SL-2 window-28 has three sets of additional transects for $^{12}C$, $^{13}C/^{12}C$ and $^{16}O$. Each set of transects were placed along R25, R45 and R65 and C15, C30 and C45.

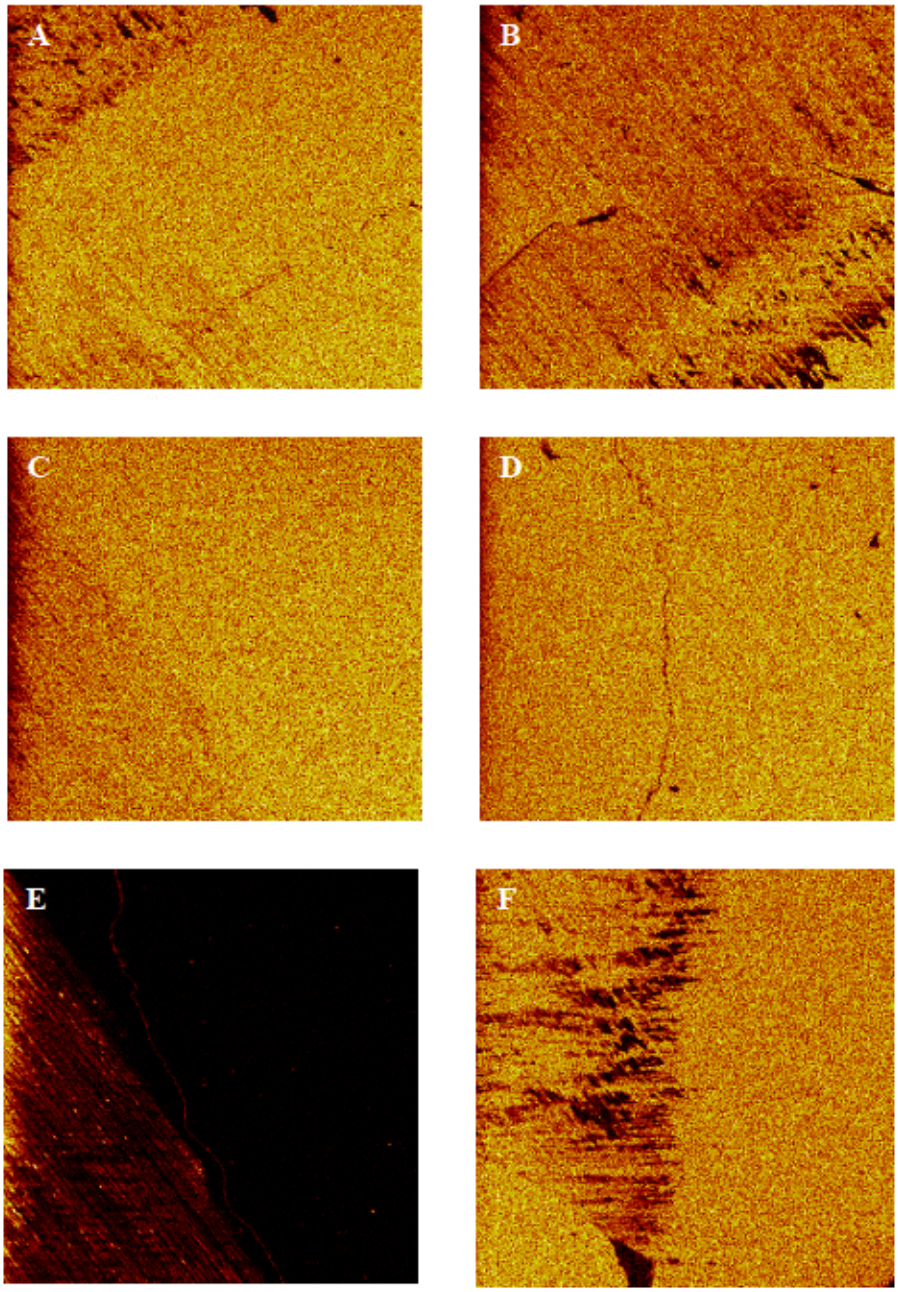


Figure 28. Diamond SL-5 window-0, window-1, window-2, window-3 and window-4 element maps. Element maps color scale is set as black is equal to 0 and yellow is relative to the highest value within a window. A is the $^{12}C$ signal intensity (SI) element map for window-0. B is the $^{12}C$ SI element map for window-1. C is the $^{12}C$ SI element map for window-2. D is the $^{12}C$ SI element map for window-3. E is the $^{16}O$ SI element map for window-2. F is the $^{12}C$ SI element map for window-4. Figure shows the linear and crack-like features marked by significant $^{12}C$ SI drops inherent to SL-3 and SL-5.

**AR.** The five analysis windows of AR showed homogenous $^{12}C$ SI response with minimal inclusions or linear features (Figure 3b, 4b, 5b and 6b). This set of 24 transects was processed for $^{13}C$ normalized to $^{12}C$. The resulting SI ratio of $^{13}C/^{12}C$ is represented in each figure as transects along the same R and C from $^{12}C$ transects. Element maps of the normalized SI ratio are presented for each window (Figure 29).

Window-1. $^{13}C/^{12}C$ transects of window-1 show regions of plateaus with highly variable SI response over short intervals (Figure 30). Window-1 has a linear feature that was void in the $^{12}C$ element map (Figure 3b). However, this same feature cannot be observed in the $^{13}C/^{12}C$ element map for window-1 (Figure 29a). R192 of the $^{13}C/^{12}C$ transect intercepts the linear feature that is void in $^{12}C$. The 4$^{th}$ order moving average polyline (Figure 30 - R192) shows no appreciable change in $^{13}C/^{12}C$ SI at the intercept with this $^{12}C$ linear feature near pixel 15. All transects show plateaus separated by regions of stark change (Figure 30 - R64 pixel 60) or gradual change (Figure 30 - C64 pixel 100).

Window-2. $^{13}C/^{12}C$ transects of window-2 show regions of plateaus and sharp cyclic SI response (Figure 31 - R64 and R192 respectively). The $^{12}C$ element map shows no sharp changes in $^{12}C$ SI (Figure 4b). The $^{13}C/^{12}C$ element map shows disseminated regions of high SI (Figure 29b). Transects that show plateaus separated by stark or gradual changes include C64, C128 and R128 (Figure 31). Transects that include regions of cyclic SI include portions of R64 and C192. While R192 only shows cyclic SI response (Figure 31).

Window-3. $^{13}C/^{12}C$ transects of window-3 dominantly show cyclic stark changes with transects R64 and R192 showing average decreases from left to right. While all other transects remain near a base level (Figure 32). R128 and C64 $^{13}C/^{12}C$ transects with cyclic change also have regions of plateaus bound by stark change (Figure 32 - R128 and C64). Transects that

decrease from left to right either have restricted regions of change or gradual change. R64 from pixel 20 to 75 appears to be the main decrease for the $^{13}C/^{12}C$ SI transect (Figure 32 - R64). R192 on average decrease across the entire transect (Figure 32 - R192).

Window-7. $^{13}C/^{12}C$ transects of window-7 have plateaus bound by stark change with transect C64 and R128 having gradual change. R64, R192, C128 and C192 all have plateaus in $^{13}C/^{12}C$ SI that are bound by changes as large as 20% over 9.8 µm (Figure 33 - R192 pixel 80 to 85). Transects C64 and R128 instead of plateaus show concave down gradual changes. Concave down form of the C64 transects dominates the plot (Figure 33 - C64). While R128 from pixel 0 to 175 is the concave down form with 175 to 255 shows cyclic change (Figure 33 - R128).

**SL-2 Window-28.** The subhedral mineral inclusion in Figure 16b shows zonation of $^{12}C$ SI (Figure 16a - R64). Diamond contiguous to this inclusion shows an increase of 26.7% in $^{12}C$ SI from the boundary of this inclusions 50.78 µm to the right along R64 (Figure 16a). Additional detailed transects where done for $^{12}C$, $^{13}C/^{12}C$ and $^{16}O$ along R25, R45 and R65 from pixel 0 to 55 and along C15, C30 and C45 from pixel 10 to 120. Element maps for each component are presented (Figure 34). Transects along these new rows and columns are presented.

$^{12}C$. $^{12}C$ zonation presented for C64 (Figure 16a) is further elucidated by detailed transects. Detailed transects can be seen intersecting multiple zones of high and low SI in the $^{12}C$ element map (Figure 34b). Each set of R and C transects show variable regions of high and low $^{12}C$ SI plateaus or peaks (Figure 35). R25 and C30 also show the gradual increase in $^{12}C$ from the inclusion and contiguous diamond (Figure 35 - R25 pixel 30 to 45, C30 pixel 74 to 90). C15 and R45 provide the longest transect of the mineral inclusion (Figure 34b). The inclusion is 146.5 µm long in C15 with multiple cycles of minima and maxima ranging from 2 to 18 $^{12}C$ SI. The inclusion is 91.8 µm wide in R45. The inclusion is R65 transits from a region of low into high

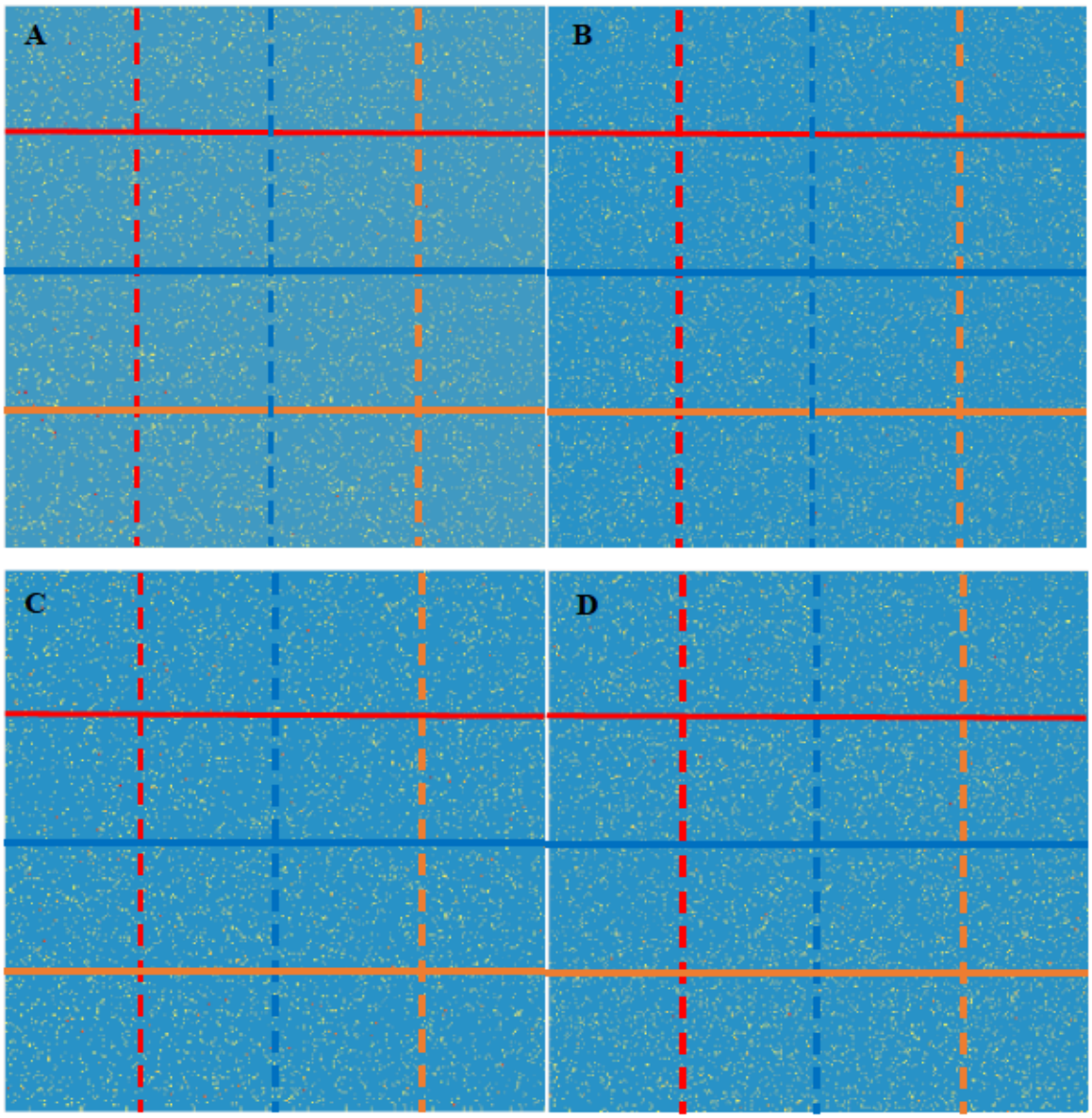


Figure 29. Diamond AR $^{13}C/^{12}C$ element maps with lines of $^{13}C/^{12}C$ transects. A is the element map for window-1. B is the element map for window-2, C is the element map for window-3. D is the element map for window-7. Pixel color corresponds to SI with blue pixels being zero and yellow/red pixels being high SI.

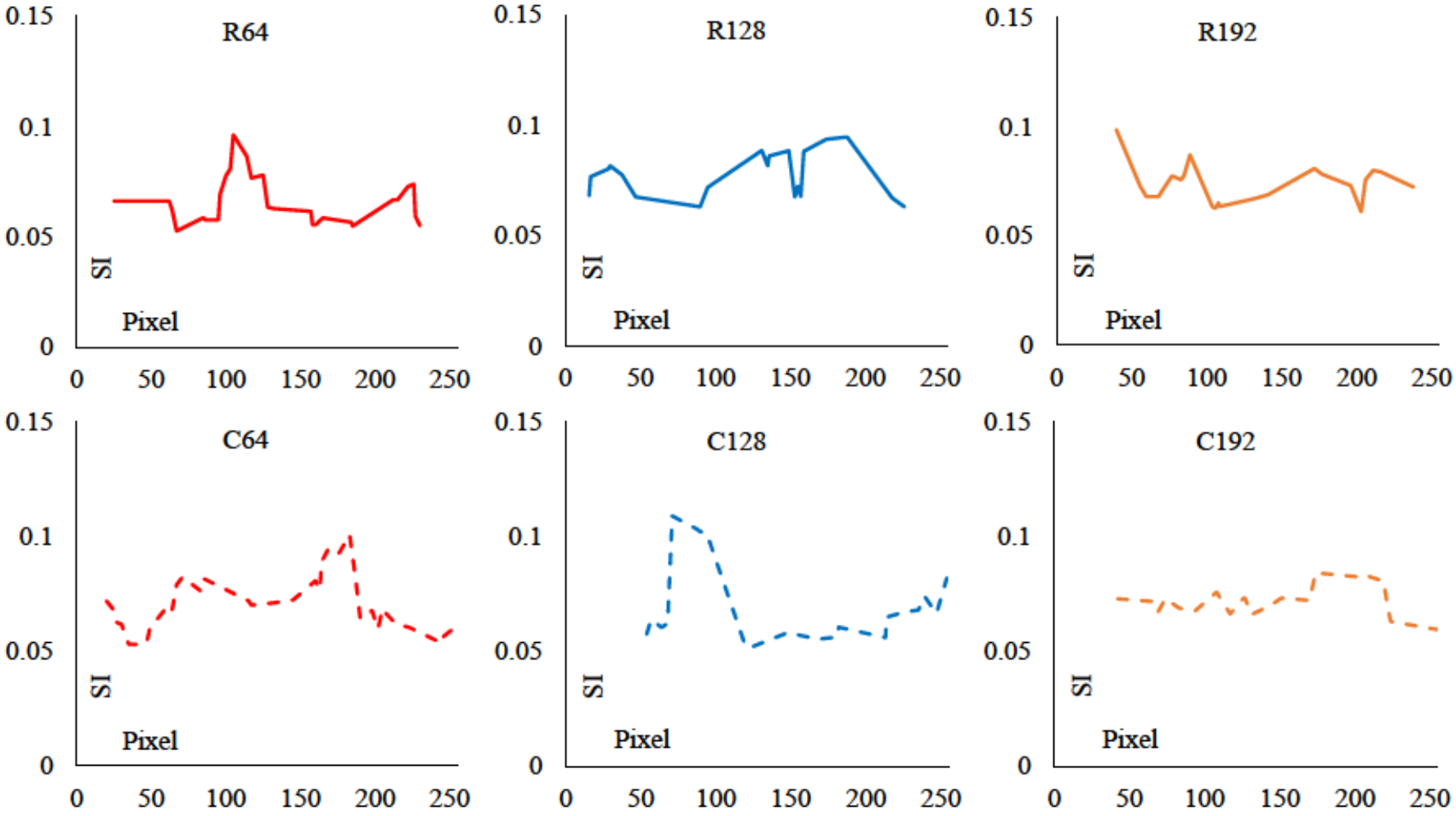


Figure 30. Diamond AR window-1 $^{13}C/^{12}C$ 4$^{th}$ order moving average polyline transects. Plot titles refer to each transects location on the element map with R being row and C being column transects. Y-axis is Signal Intensity (SI).

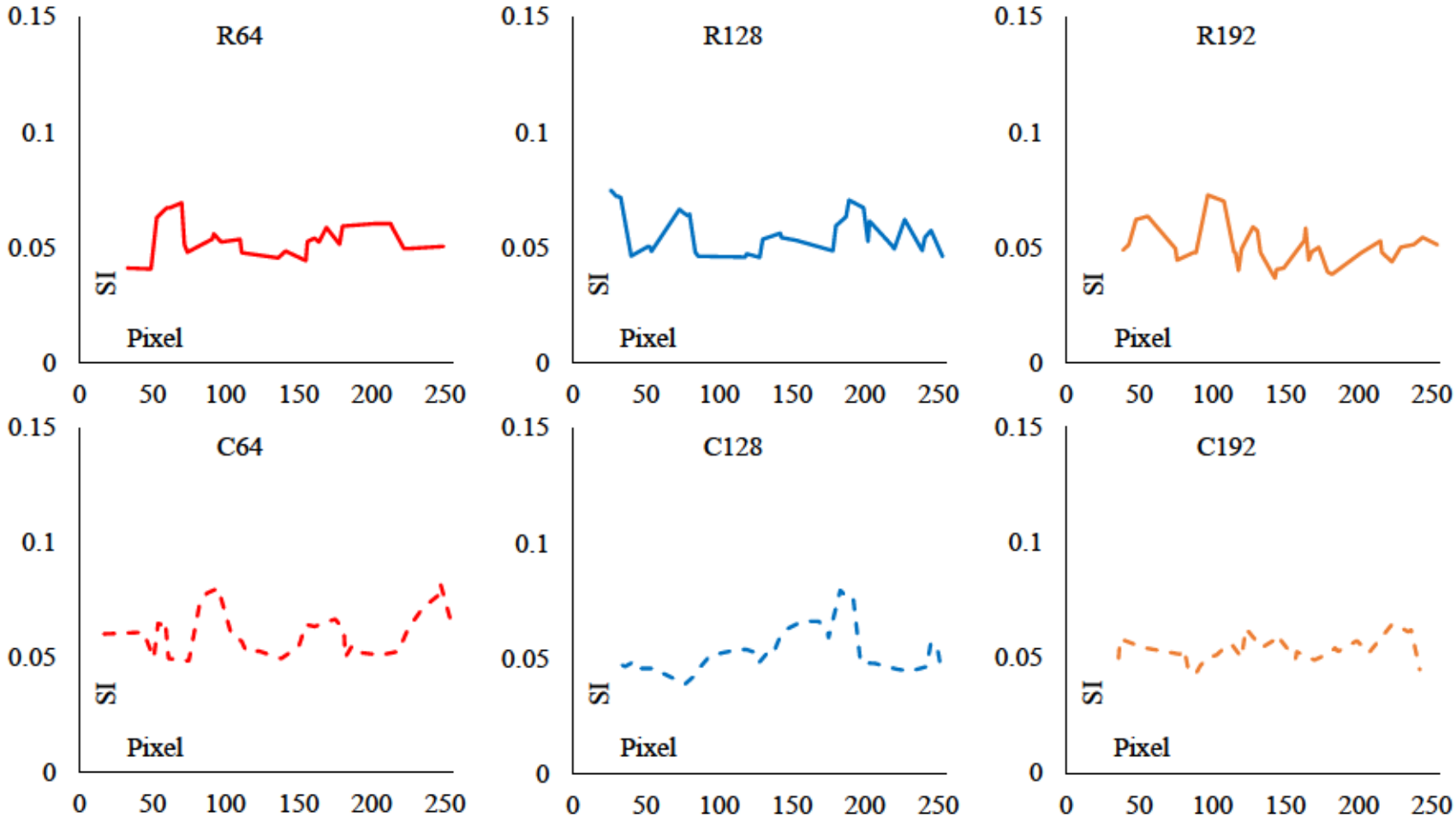


Figure 31. Diamond AR window-2 $^{13}C/^{12}C$ 4$^{th}$ order moving average polyline transects. Plot titles refer to each transects location on the element map with R being row and C being column transects. Y-axis is Signal Intensity (SI).

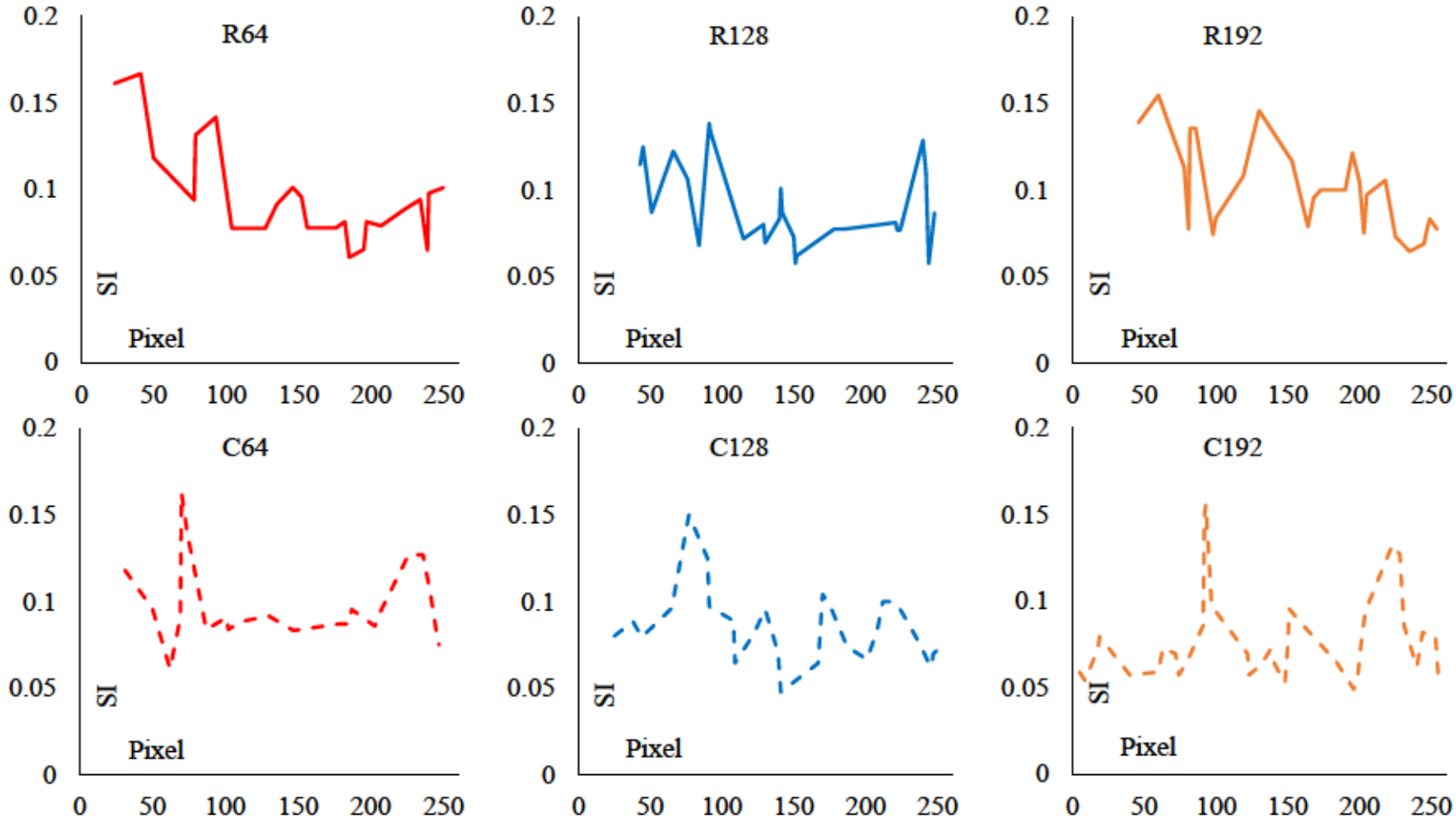


Figure 32. Diamond AR window-3 $^{13}C/^{12}C$ 4$^{th}$ order moving average polyline transects. Plot titles refer to each transects location on the element map with R being row and C being column transects. Y-axis is Signal Intensity (SI).

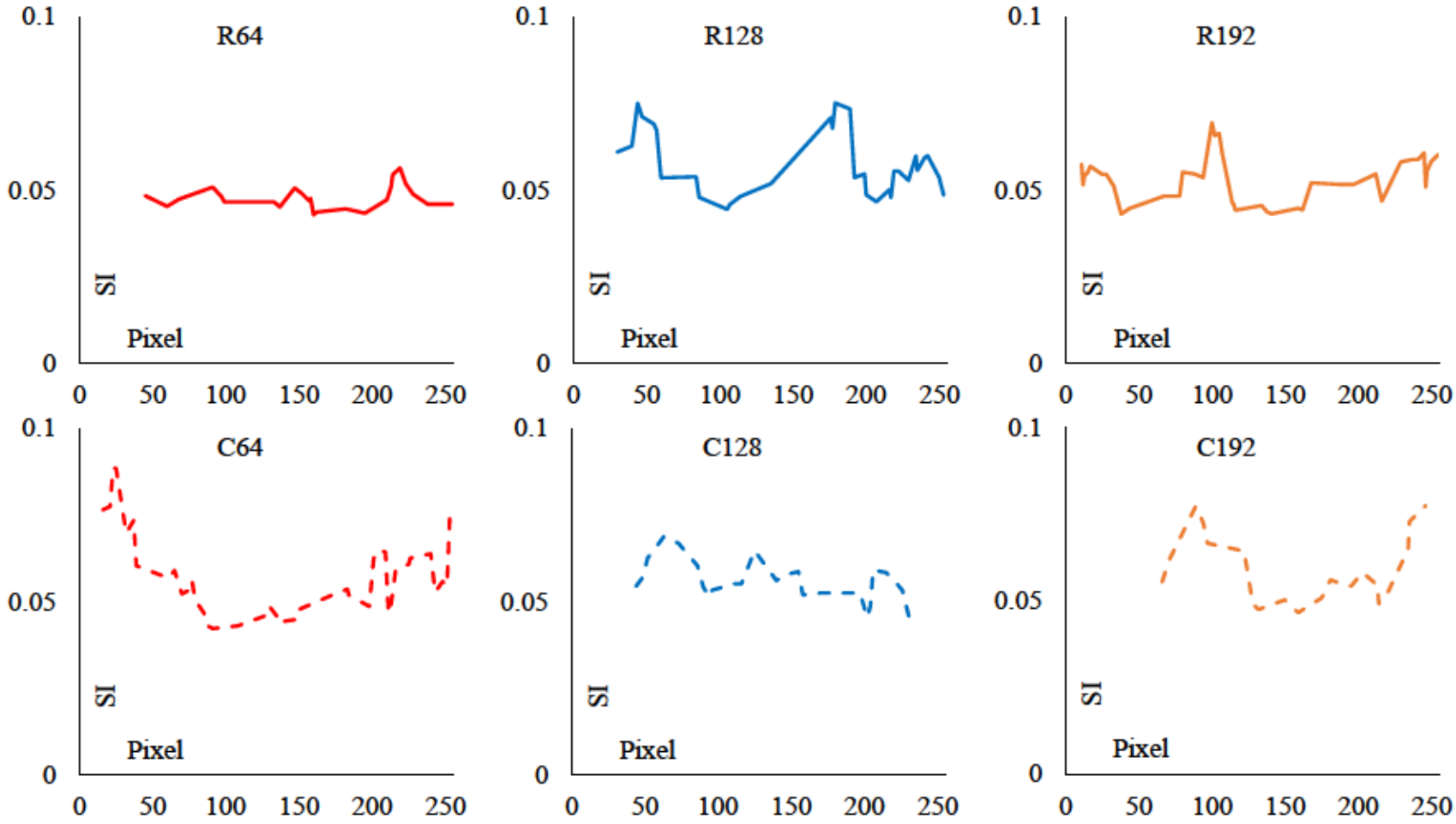


Figure 33. Diamond AR window-7 $^{13}C/^{12}C$ 4$^{th}$ order moving average polyline transects. Plot titles refer to each transects location on the element map with R being row and C being column transects. Y-axis is Signal Intensity (SI).

$^{12}C$ SI (Figure 34b). In R65 the transition of region is apparent with a saddle shape in the transect (Figure 35). The transect starts in a region of low SI and sharply increases at pixel 14 to the region of high $^{12}C$ SI before entering a new zone of low $^{12}C$ SI at pixel 32 (Figure 35 - R65).

$^{13}C/^{12}C$. $^{13}C/^{12}C$ zonation in the window-28 inclusion shows a different pattern than $^{12}C$ zonation. In Figure 34b, higher $^{12}C$ SI can be seen in the window-28 inclusion near the boundary between inclusion and diamond. This zone of high $^{12}C$ SI marks a void in the $^{13}C/^{12}C$ SI element map north of R45 (Figure 34d). While the region of lower $^{12}C$ SI further into the inclusion (Figure 34b) shows as a band of high $^{13}C/^{12}C$ SI (Figure 34d). The congruency between $^{12}C$ and $^{13}C/^{12}C$ SI appears in the internal zones of $^{12}C$ SI and all $^{12}C$ SI zones south of R45 (Figure 34b and 34d). Transects of $^{13}C/^{12}C$ SI for the inclusion show similar patterns as noted for diamond AR. R45, R65, C15 and C30 show plateaus bound by stark changes in SI (Figure 36). Of these transects, C15 shows the most conformable plateau at pixel 60 (Figure 36 - C15). The plateau at pixel 60 is 0.08 SI bound by planes at 0.03 SI. Plateaus in other transects show more gradual changes from plateau to plane such as R45 and R65 at pixel 28 and 24 respectively (Figure 36 - R45 and R65). Cyclic changes noted in $^{13}C/^{12}C$ SI for AR were tightly cycled (Figure 32 - R192). While SL-2 $^{13}C/^{12}C$ SI shows minimal cyclic changes in C30 and C45 at pixel 100 and 75 respectively (Figure 36 - C30 and C45).

$^{16}O$. $^{16}O$ transects of window-28 show similar patterns as described for $^{12}C$. In $^{12}C$ SI transects, zones of variable SI response are easily differentiated by dramatic changes to the SI over minimal distances. Within the $^{16}O$ transects, similar patterns are present (Figure 37). Morphologies measured by the $^{16}O$ transects include zones of high or low SI and well defined transition from inclusion to diamond. Instances of conformable boundaries between zones of SI response for $^{16}O$ include all detailed transects (Figure 37). Unlike the $^{12}C$ transects, $^{16}O$ transects

have defined boundaries between inclusion and diamond. The R25 and C30 transects show this gradual increase in the SI response of $^{12}C$ (Figure 35 - R25 pixel 30 to 45, C30 pixel 74 to 90). In $^{16}O$ R25 and C30 transects the boundaries of the inclusion are definite and after these bounds the SI remains at $1 \pm 1$ for the remainder of the transect (Figure 37 - R25 pixel 31, C30 pixel 74). R45 and C15 provide the longest dimensions of the inclusion. These transects of $^{12}C$ measured the inclusion to be 146.5 µm long and 91.8 µm wide (Figure 34b). These transects of $^{16}O$ measured the inclusion to be 158.2 µm long and 95.7 µm wide (Figure 34a).

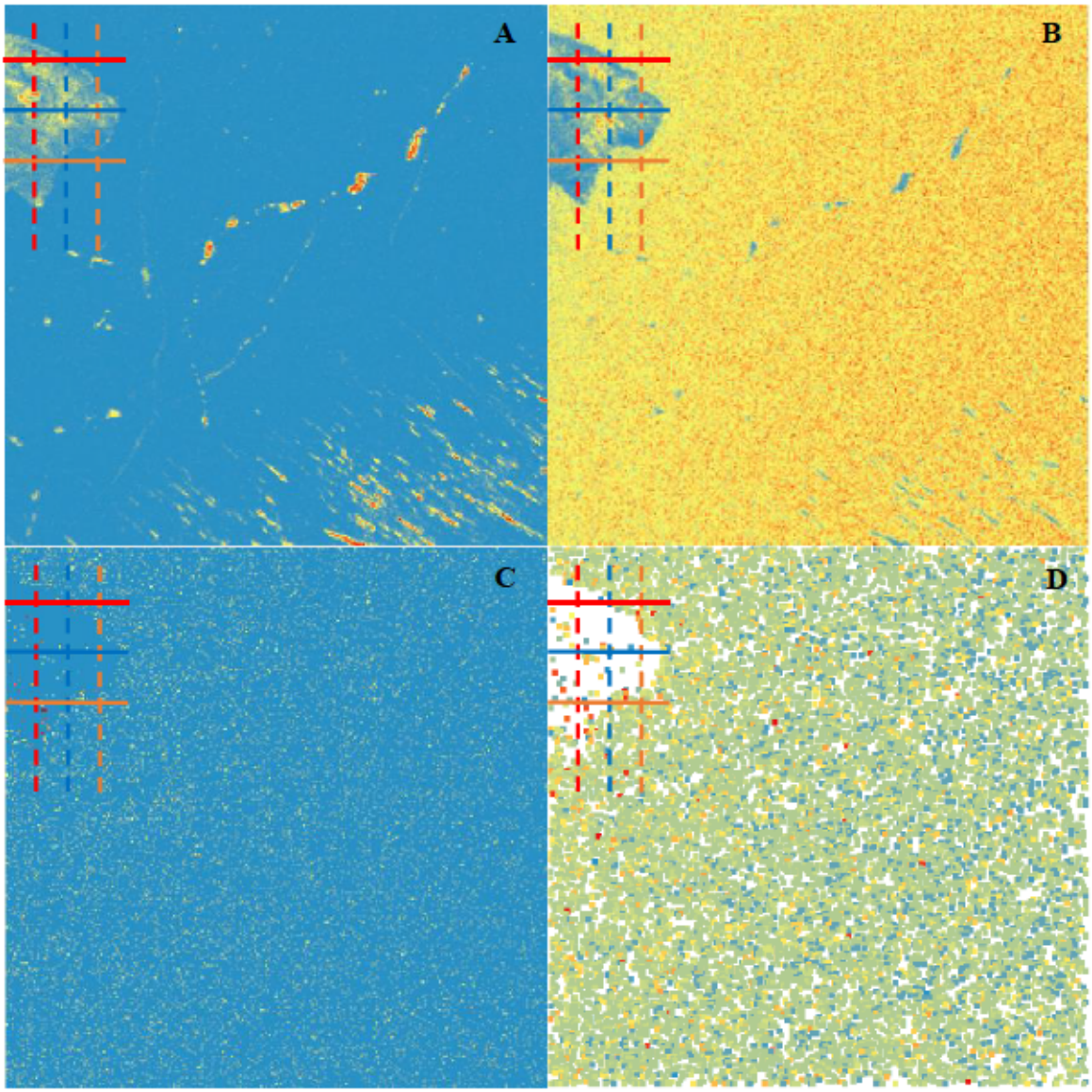


Figure 34. Diamond SL-2 window-28 $^{12}C$, $^{13}C/^{12}C$ and $^{16}O$ element maps with transects. A is the $^{16}O$ element map with transects. B is the $^{12}C$ element map with transects. C is the $^{13}C/^{12}C$ element map with all zero data points and transects. D is the $^{13}C/^{12}C$ element map with all zero data points removed and transects. Pixel color corresponds to SI with blue pixels being zero and yellow/red pixels being high SI.

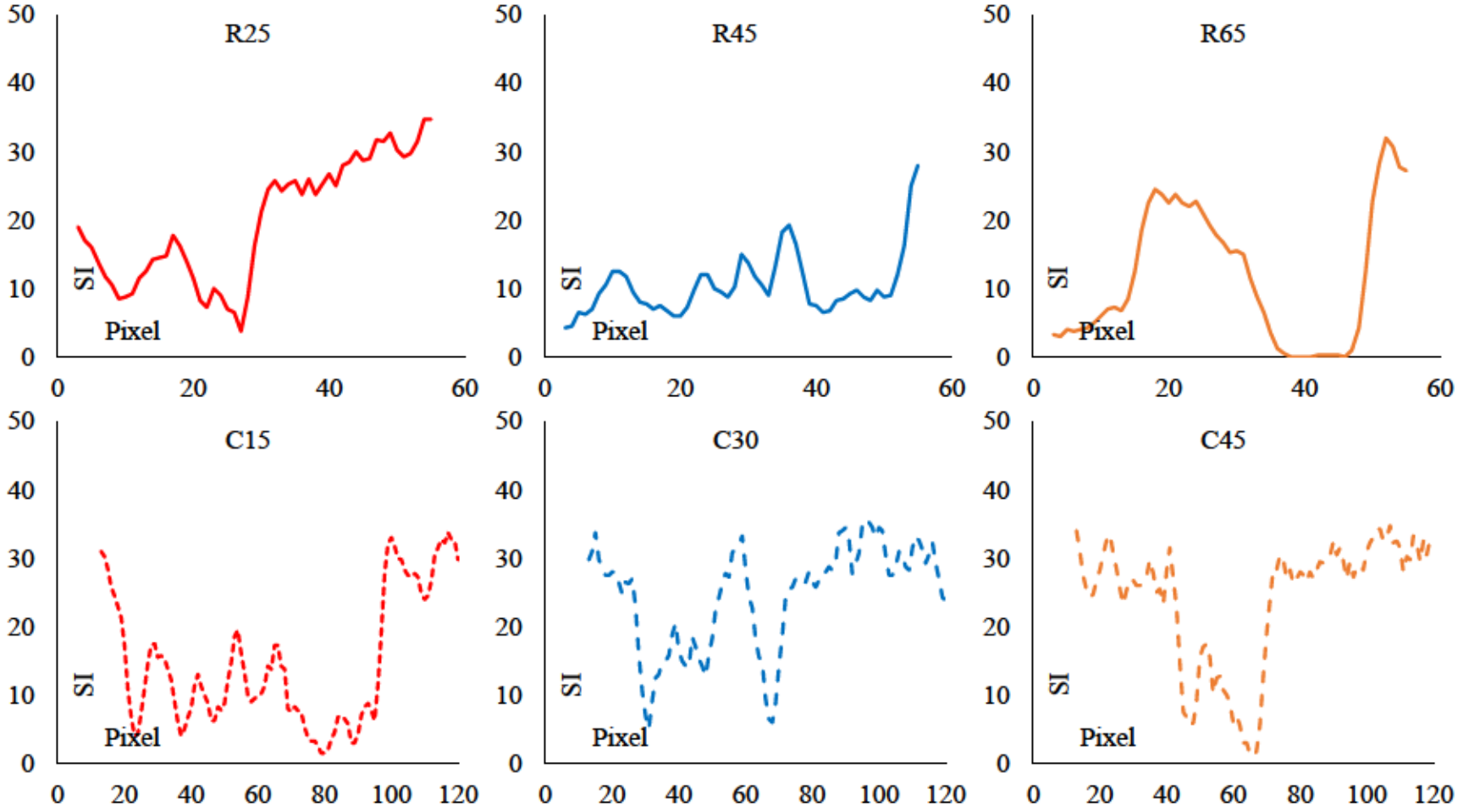


Figure 35. Diamond SL-2 window-28 $^{12}C$ 4$^{th}$ order moving average polyline transects. Plot titles refer to each transects location on the element map with R being row and C being column transects. Y-axis is Signal Intensity (SI).

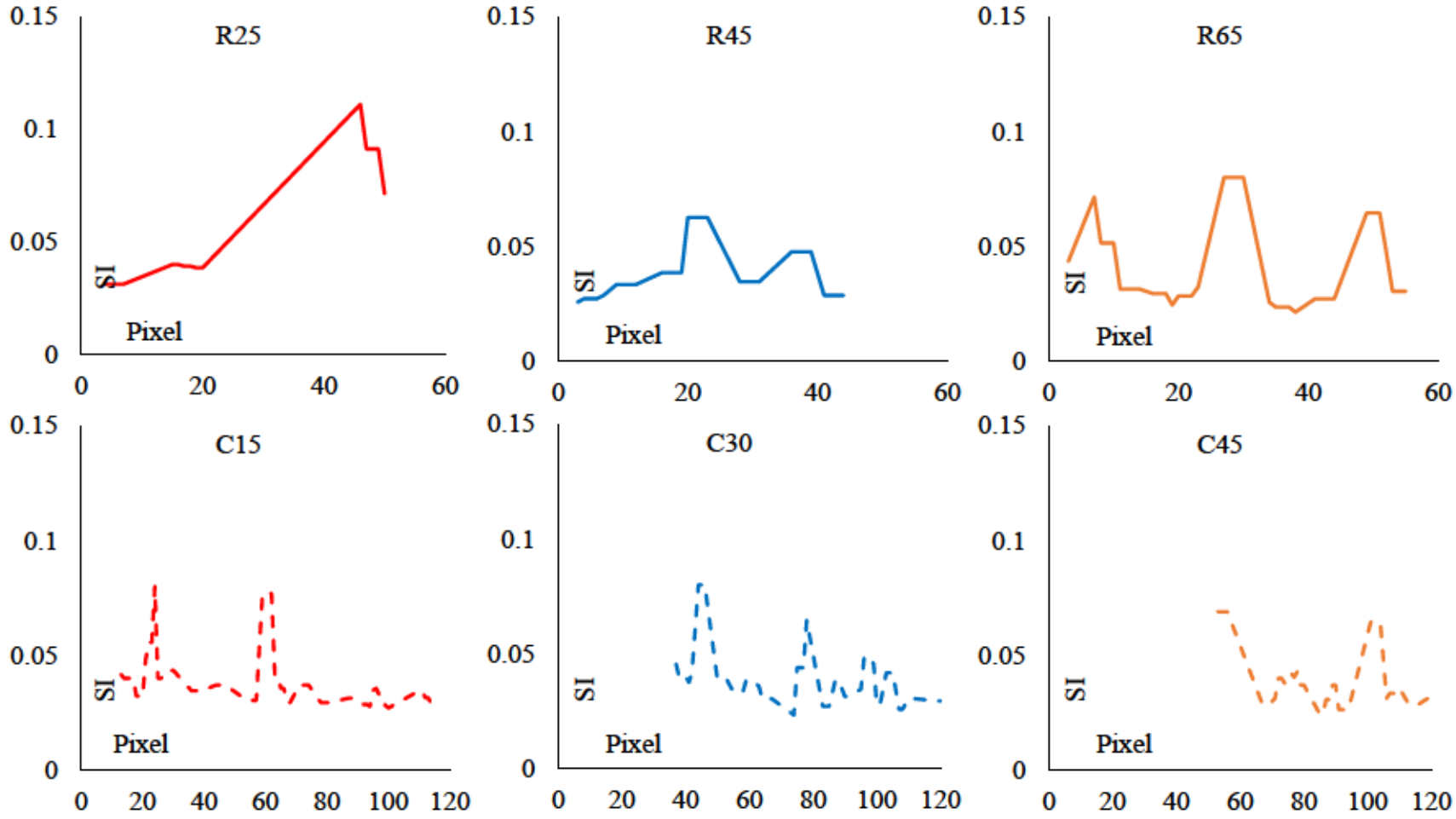


Figure 36. Diamond SL-2 window-28 $^{13}C/^{12}C$ 4$^{th}$ order moving average polyline transects. Plot titles refer to each transects location on the element map with R being row and C being column transects. Y-axis is Signal Intensity (SI).

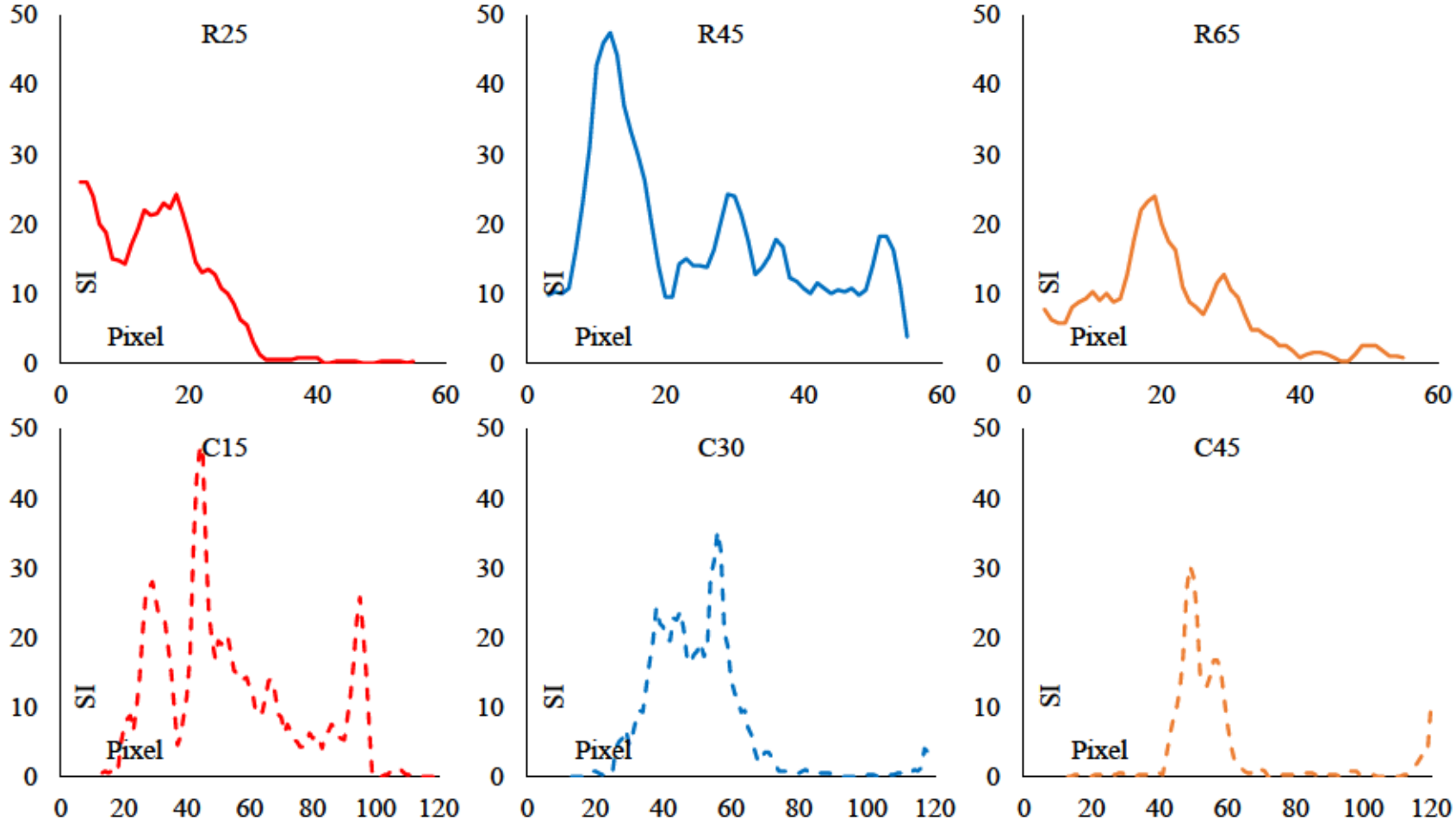


Figure 37. Diamond SL-2 window-28 $^{16}O$ 4$^{th}$ order moving average polyline transects. Plot titles refer to each transects location on the element map with R being row and C being column transects. Y-axis is Signal Intensity (SI).

## DISCUSSION

I hypothesized that Time of Flight Secondary Ionization Mass Spectrometry (ToF-SIMS) analyses would characterize stable isotope variation and trace element concentrations in diamond with high spatial resolution. Such a methodology would make chemical characterizations of diamond across geologic terranes more accessible. However, the conversion of signal intensity (SI) to chemical data have resulted in substantial errors when compared to known $\delta^{13}C$ values (Table 2). Complications and a myriad of unknowns when converting SI to chemical data led to these errors. Complications and unknowns such as the matrix effect, isotopic fractionation during analyses and establishing the settings of the ToF-SIMS ion guns may have influenced the accuracy and precision of SI conversions. Thus, this study considers what constraints need to be established or changes to the experimental design in order to accurately and precisely convert SI to chemical value using ToF-SIMS analysis windows or by individual pixel. Also, defining non-quantitative chemical characterizations made from ToF-SIMS element map transects for diamonds AR and SL-2.

### Signal Intensity Conversions

Establishing a process to convert SI to delta notation was the early goal of this project. However, direct calculations using equation 4 (Stephan, 2001) resulted in $\delta^{13}C$ values wildly outside of published naturally occurring calcite and diamond (Table 1; Van Rythoven, 2012; McCandless et al., 1991). $\delta^{13}C$ values calculated for seven analysis windows across three calcite crystals ranged from -662.88 to 1779.82 ‰ VPDB (Table 2). Calculated values for the seven analysis windows of SL-1 ranged from $\delta^{13}C$ -481.87 to -14.75 ‰ VPDB (Table 2). Calculated

values for the four analysis windows of AR ranged from $\delta^{13}C$ -83.85 to 72.36 ‰ VPDB (Table 2). Each group when compared to published values of diamonds or calcite resulted in extreme errors (Table 2). To address this inaccuracy, instrumental parameters that influence mass resolution accuracy such as the time resolution of the detector and electronics need to be factored (Stephan, 2001). Such analytical modeling proved to be outside the time constraints of this project. Future modeling of the dataset created in this thesis will need to address multiple chemical phenomena as well as the instrumental parameters detailed by Stephan (2001).

**ToF-SIMS Considerations**

Oak Ridge National Labs (ORNL) has a general use ToF-SIMS. Meaning, a ToF-SIMS used to determine qualitatively the presence of certain elements at different layers in motherboard chips and solar power cells. These analyses are done with the Atomic Force Microscope (AFM) tip attachment. AFM works by measuring the depth of the sputter pit of an analysis window. Allowing a researcher to determine the volume removed during analysis and potentially back calculate volumes of analyzed ions. Such a quantification could also be achieved by use of a ToF-SIMS that has electron multipliers built into the detector. Adding these components to ToF-SIMS SI conversions would improve accuracy.

Establishing the analytical settings at ORNL included adjusting the ion gun voltages to obtain sufficient ionization as determined by the laboratory manger and technician. During this process, less abundant isotopes or element impurities are drowned out by the abundance of $^{12}C$ at the detector. This signal loss was under constant monitoring by the laboratory technician and instrumental settings normalized before each analysis window. This standard practice led us to assume that signal loss is negligible between analysis windows.

Another consideration for ToF-SIMS analysis of diamond is ionization efficiency of carbon stable isotopes. The relationship between isotopic mass, vibrational frequency and bond stability is assumed relevant during secondary ionization. As a molecules isotopic mass decreases the vibrational frequency of that molecule increases and thus the molecule is relatively less stable than a similar molecule of heavier isotopic composition. During secondary ion generation, absorbance of the energies from the ion guns increases the potential energy in a molecular system. This increased energy pushes atoms apart and if the dissociation energy of that molecule is surpassed, the bond is broken. However, the potential energy curve of a molecule changes with isotopic composition (Figure 38). In Figure 38, three molecules with masses arbitrarily different have hypothetical Morse potential energy curves where the molecules with the heavier isotopic weight have higher dissociation energies. The difference between $^{12}C$ and $^{13}C$ bonds in a Morse potential energy curve are minimal and thus fractionation of carbon stable isotopes due to changes in dissociation energy is likely negligible for ToF-SIMS. However, systematic fractionation of $^{13}C$ and $^{12}C$ has not been investigated for ToF-SIMS and thus what, if any, influence is unknown.

Mass resolving capacity of $^{13}C$ versus $^{12}C^{1}H$ is another problem of stable isotope studies by ToF-SIMS. The generation of $^{12}C^{1}H$ ions is attributed to residual gases in the vacuum chamber (Stephan, 2001) while any $^{13}C$ ion can be assumed with relative confidence to be from the analyte. These ion species have the same atomic mass unit and thus the instrument will bin the two SI counts as the same ion. Separation of ion species is done through mathematical peak separations using multivariate statistics and by manual post processing. Under ideal conditions for a polished Teflon coating, modeling of peak separations was considered insufficient for high analytical accuracy (Stephan, 2001). This study considers all $^{13}C$ SI data unprocessed. In the

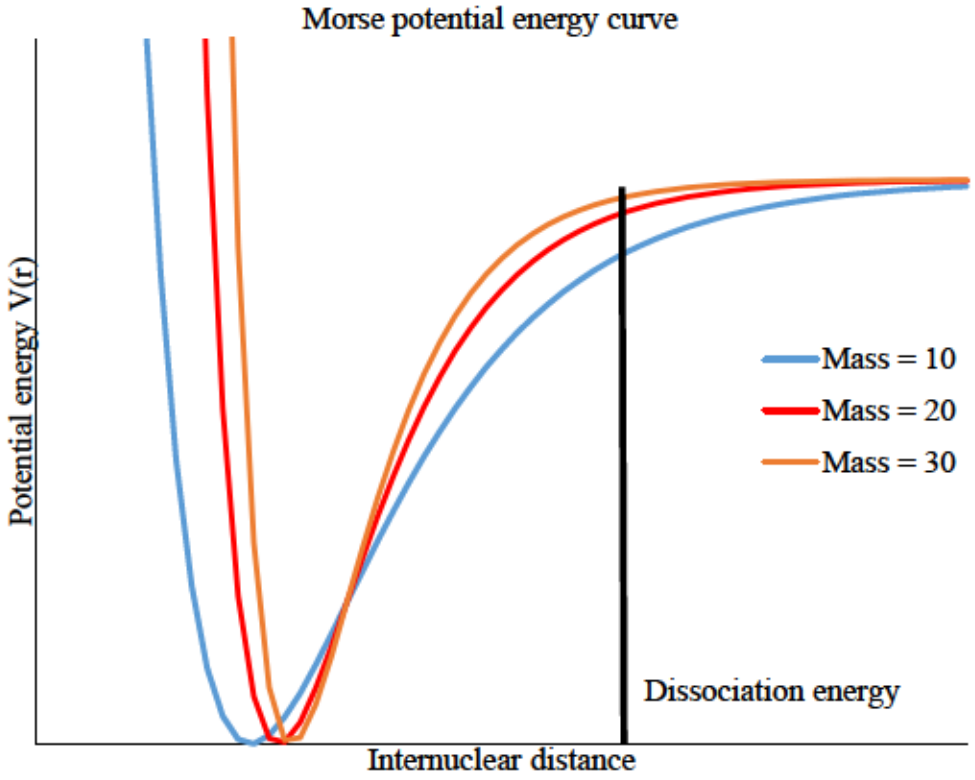


Figure 38. Morse potential energy plot showing the effect of increasing molecular weight on the quantum mechanical behavior of bond stability. The Morse potential used in this figure is $V(r) = De\left(1\text{-}e^{-\alpha(r-r_e)}\right)^2$. When De is the dissociation energy, α is proportional to the force constant k by $\alpha = \sqrt{\frac{k}{De}}$ when $k = m\omega^2$ for m is mass and ω is vibrational frequency, r is bond length and $r_e$ is equilibrium bond length. The internuclear distance is defined as the distance between two nuclei that are bound together. Equations and principles applied in this figure are from McQuarrie and Simon (1997).

spectra collect for each analysis window, a shoulder of $^{12}C^{1}H$ on the $^{13}C$ peak is observed. Through identification of ion species during post processing at ORNL, it is possible that $^{13}C$ ion counts within a window are miss identified as $^{12}C^{1}H$. The corollary is equally assumed, counts from the $^{12}C^{1}H$ SI can artificially boost the $^{13}C$ peak. This uncertainty in $^{13}C$ counts further skewed SI conversions.

Our ToF-SIMS element map characterizations for $^{12}C$, $^{13}C/^{12}C$ and $^{16}O$ used 0.038% of total data gathered. This analysis did not include additional ionized species that were measured such as molecular carbon $C_2^-$, $C_3^-$ and $C_4^-$ and other exotic phases that remain unprocessed in the original dataset. In order to analyze the full chemical suite of ions generated a statistical package such as the Sandia National Laboratories Automated eXpert Spectral Image Analysis (AXSIA) would be required (Smentkowski et al., 2005). AXSIA would allow a user to concatenate element maps from cation and anion analyses into a series of hyperspectral component maps as well as performing multivariate statistical calculations (Smentkowski et al., 2005). Such a program allows for the analysis of the spatial relationship between all ion species. Concatenated data also mitigates the computational load of working with potentially hundreds of element map arrays. The chemical characterizations here within are thus limited by simple statistical observations of single elements maps or element maps normalized to one ion species. As such, multi ion relationships are unknown.

The influence of the matrix effect on this study is unquantified and was unknown before analysis at ORNL. Stephan (2001) shows that usage of a standard medium that is crystallographically similar to the unknown crystal will mitigate skew due to the matrix effect. By establishing an internal standard of calcite for equation 4 to convert SI to chemical values for our diamonds, an experimental bias was unknowingly built into our results. This bias is shown in

Table 2 by the highly variable SI conversions of diamonds SL-1 and AR. Attempts to derive a matrix effect factor to correct for the skew of different crystal mediums was ineffective. Future studies of diamond with the intent of investigating stable isotope variation by ToF-SIMS will need to include isotopically characterized standards of diamond with similar internal crystal structures as unknown diamonds. Such a standard diamond may be difficult to establish. In Van Rythoven (2012) diamonds originating from the same pipe in the Diavik mine showed different diamond type and internal crystal structure. A majority of diamonds from the Diavik mine are of P-type and lesser amounts of E-type and Ultra deep-type (Cartigny et al., 2009; Van Rythoven, 2012). The best case scenario to mitigate the matrix effect would be to use diamonds from the same mine, of the same diamond type and internal structure as an internal standard. Though due to regional variation, each region in question would need a contemporary standard. These requirements bring about an issue of cost. To establish a reliable standard, the diamond isotopic variation, internal structure and diamond type would need to be determined. Such an effort would require ion microprobe systems to determine the isotopic variability and electron microprobe analyses to determine internal structure and diamond type. The costs associated with development of an internal standard for ToF-SIMS would likely double the analytical costs associated with any such study.

**Chemical Characterization**

High spatial resolution element mapping is the greatest advantage of ToF-SIMS analyses (Smentkowski et al., 2005). Through transects, element map topology is hypothesized to characterized chemical zones. Chemical zones of $^{13}C/^{12}C$ and $^{16}O$ for SL-2 and $^{13}C/^{12}C$ of AR are defined as regions in the 4$^{th}$ order moving average polylines with significant change to SI over a

small interval. Characterizations of these polylines include three cases: orthogonal, acute and sinusoidal. In orthogonal intersection, the transect shows significant changes in chemical behavior over short distances (Figure 39d). Acute intersections show gradual changes in chemical behavior over continuous distances (Figure 39c). While sinusoidal show sharp sporadic shifts and in some cases cyclic change to chemical behavior (Figure 40d). This study will define significant SI change as $\geq 25$ % over a distance of $\leq 20$ µm. While gradual SI change is defined as $\geq 25$ % over a continuous distance. Sinusoidal behavior is marked by non-continuous sharp changes in SI over distances $\leq 5$ µm with two or more troughs.

**SL-2 Characterization.** Seven windows in SL-2 show surficially clean surfaces (Figures 15 through 21). Meaning that the polishing and mounting process resulted in a level surface of SL-2 in the indium mount. Window-28 may have surficial errors in the SE section of the window. This region was excluded from detailed transects for this reason. The detailed transects of the mineral inclusion in window-28 show multiple regions of high and low SI for $^{13}C/^{12}C$ and $^{16}O$ (Figure 36 and 37). These variations are likely due to minerology and diffusion between mineral boundaries. Single phase mineral inclusions enclosed during diamond crystallization re-equilibrate throughout residence and ascension from the DSF (Walter et al., 2011). Along these grain boundaries and the boundary between the body of the diamond and inclusion, diffusivity would be higher (Cherniak, 2010). $^{13}C/^{12}C$ and $^{16}O$ transects both likely have characteristics of re-equilibrated minerology and diffusion.

<u>$^{16}O$ characterization.</u> The element map of $^{16}O$ shows five radially concentric zones (Figure 39a). Continuous lines in Figure 39A show chemically conformable zones while dashed lines show inferred boundaries. The detailed transects for SL-2 intersected all zones and the inferred section. R45 transect is the only transect to intersect all five zones and the polyline of

this transect shows orthogonal transitions (Figure 39 - R45 pixel 5 and pixel 19). R25 intersects two boundaries and C15 intersected four boundaries and the inferred section. These two transects display sections of acute transitions (Figure 39 - C15 pixel 67 to 78 and R25 pixel 18 to 32).

$^{16}O$ discussion. The radially concentric zones are curious. In Figure 39a, defined zones appear akin to crystal growth zones. However, such an association is irrelevant. The inclusion present in SL-2 window-28 is likely a re-equilibrated amalgam of a primary enclosed phase with significant diffusion. Boundaries between secondary phases would present embayed, crystal junction and or exsolution textures (Walter et al., 2011). The lack of these textures does not preclude re-equilibration. However, since primary inclusion phases in diamond are silicates, carbonates or sulfides these zones may be a coincidental separation of secondary high SI silicate or carbonate minerals from low SI sulfide or native minerals. Subsequent diffusion along these boundaries may explain the inferred section of the inclusion (Figure 39a) though this explanation does not address the concentric zones. Further analysis of this inclusion would require quantifiable methodologies such as Laser Ablation-Inductively Coupled Plasma Mass Spectrometer or Nano-SIMS to determine the nature of concentric zones in relation to crystal history.

$^{13}C/^{12}C$ characterization. Figures 34c and 34d present two element maps for $^{13}C/^{12}C$. In Figure 34d, all zero points of $^{13}C/^{12}C$ SI where removed to make trends in $^{13}C/^{12}C$ SI directly observable. This dataset of $^{13}C/^{12}C$ with zeros removed was used to create transects. Resulting transects of $^{13}C/^{12}C$ define similar zones as in $^{16}O$ (Figure 40a). Though the zones identified for $^{13}C/^{12}C$ (Figure 40a) appear to be shifted and have slightly different margins compared to $^{16}O$ (Figure 39a). R25 starts in the outer most zone before transitioning acutely into the $^{13}C/^{12}C$ SI of the diamond body (Figure 40b – pixel 22 to 46). C15 intersects three zones orthogonally before

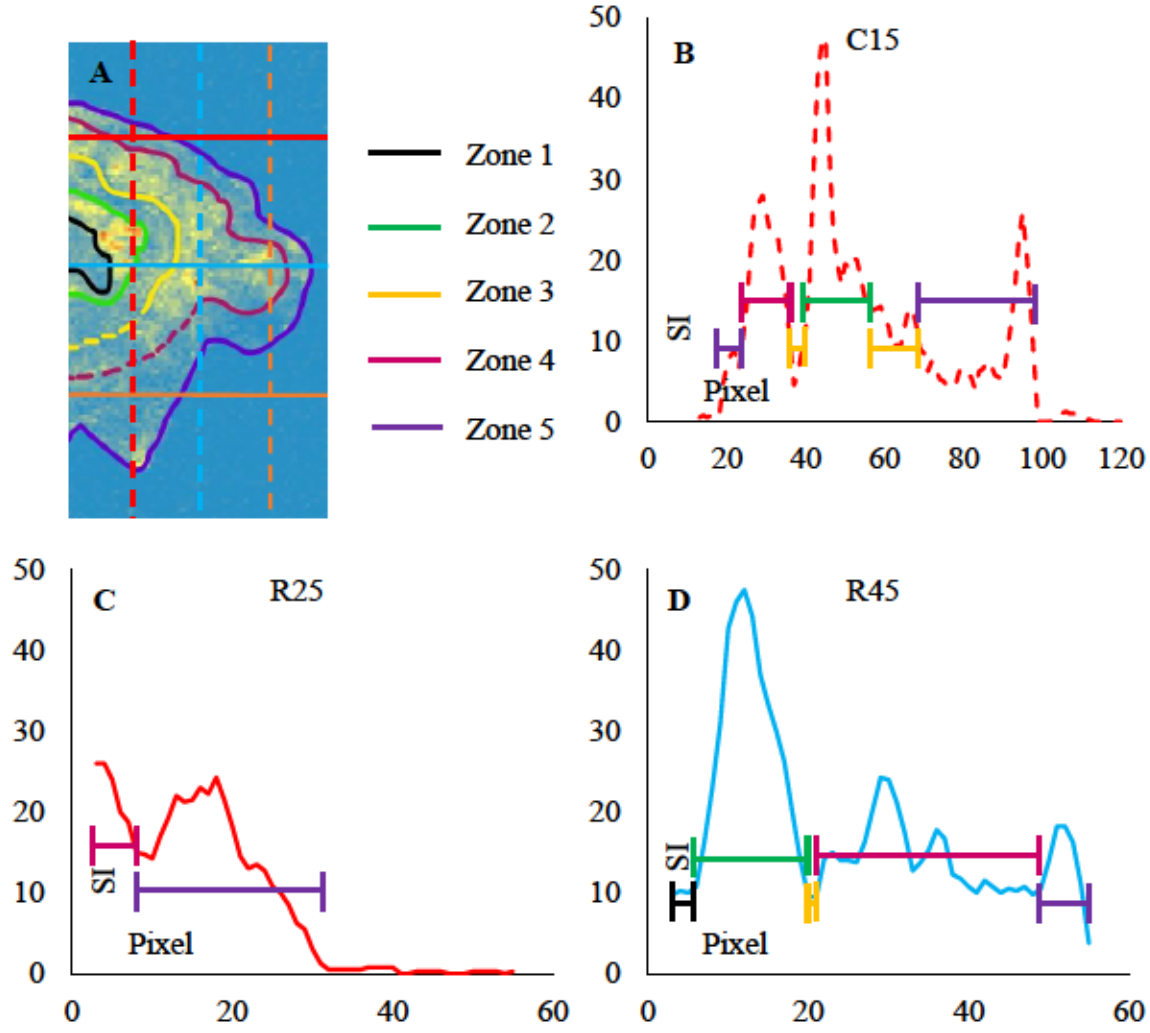


Figure 39. A SL-2 window-28 element map trimmed to show chemical zones as defined by $^{16}O$ SI variation. Each transect has the interpreted chemical zone color coordinated. Transects presented in this figure show examples of the orthogonal and acute boundary cases. In C15 at the first segment of zone 5, the orthogonal intercept at pixel 18 shows when the transect entered the first zone of the inclusion mineral. While along pixel 18 to 32 of R25, an acute intercept of gradually decreasing SI is present as the transect traverse zone 5 out into the body of the diamond.

reaching the acute edge of the inclusion. C30 similarly shows two zones orthogonally before showing a sinusoidal signature within the diamond (Figure 40d – pixel 83 to 110).

$^{13}C/^{12}C$ discussion. Moving average polylines of $^{13}C/^{12}C$ SI may not accurately represent the topology of element map transects. For example, in R25 the moving average polyline is averaging five data points for the whole transect. Another point to be made is the influence of blank space on moving average polylines. In C30 and C45, moving average polylines do not start at the beginning of each transect (Figure 41C and 41D). Instead, the polyline is shifted to where data points are more abundant. Using the data with all zeros removed made identifying chemical zones with direct observation simpler. However, Microsoft Excel calculations of the moving average polylines appear to skew the data by artificially increasing the SI (Figure 41A and 41B) and shifting the polylines (Figure 41C and 41D). These influences significantly decrease the accuracy of $^{13}C/^{12}C$ SI characterizations. In R65, the moving average polyline increases the average SI across the whole transect by 72%. In C45, the start of the moving average polyline starts at pixel 10 with all zero points included and pixel 50 with all zero points removed.

**AR Characterization.** Four analysis windows of diamond AR show homogeneous SI (Figure 3 through 6). Chemical characterization of this diamond will be determined by comparing trends in the horizontal and vertical transects for $^{13}C/^{12}C$ in a single analyses. Window-2 was selected due to the window showing minimal change in $^{12}C$ SI (Figure 4b). Minimal variation in the normalization factor used in $^{13}C/^{12}C$ element maps would mitigate change in $^{13}C/^{12}C$ due to $^{12}C$. This test is important because in order for ToF-SIMS to be a plausible methodology of stable isotope geochemistry, the analytical precision of $^{13}C$ SI variation needs to be maximized. Note, in order to make chemical characterizations possible, data characterized for AR will be for the dataset with zeros removed.

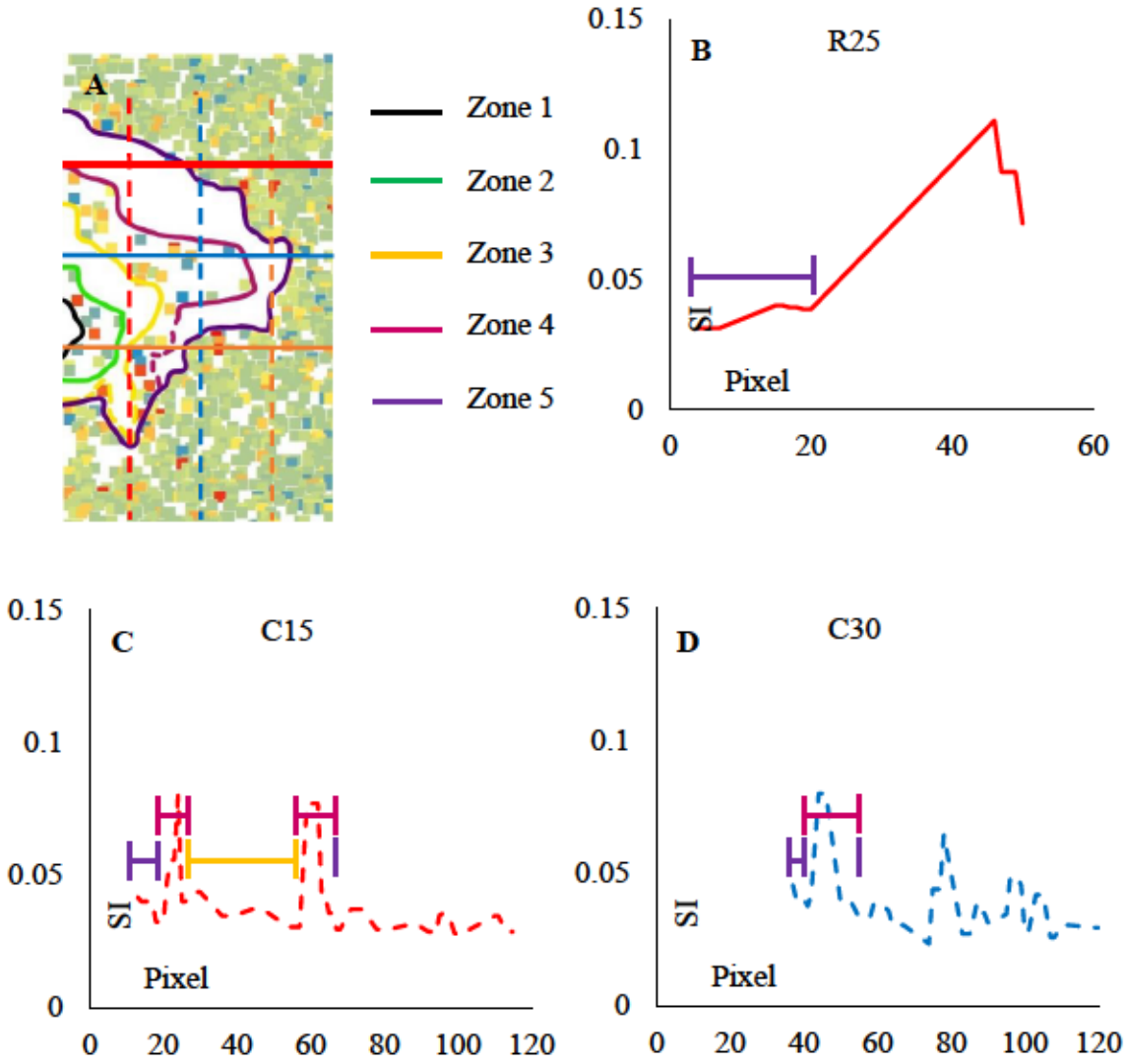


Figure 40. A SL-2 window-28 $^{13}C/^{12}C$ element map with zero points removed and remainder reclassified. Each transects intercept with a defined chemical zone are color coordinated. Single zone 5 bars represent inclusion to diamond transition. Each transect has the interpreted chemical zone color coordinated. Transects presented in this figure show examples of the orthogonal, acute and sinusoidal boundary cases. In C15 at the first segment of zone 5, the orthogonal intercept at pixel 18 shows when the transect entered zone four. C30 is an example of sinusoidal SI from pixel 83 to 110. R25 when the transect exits zone 5 shows an acute transition from inclusion into diamond.

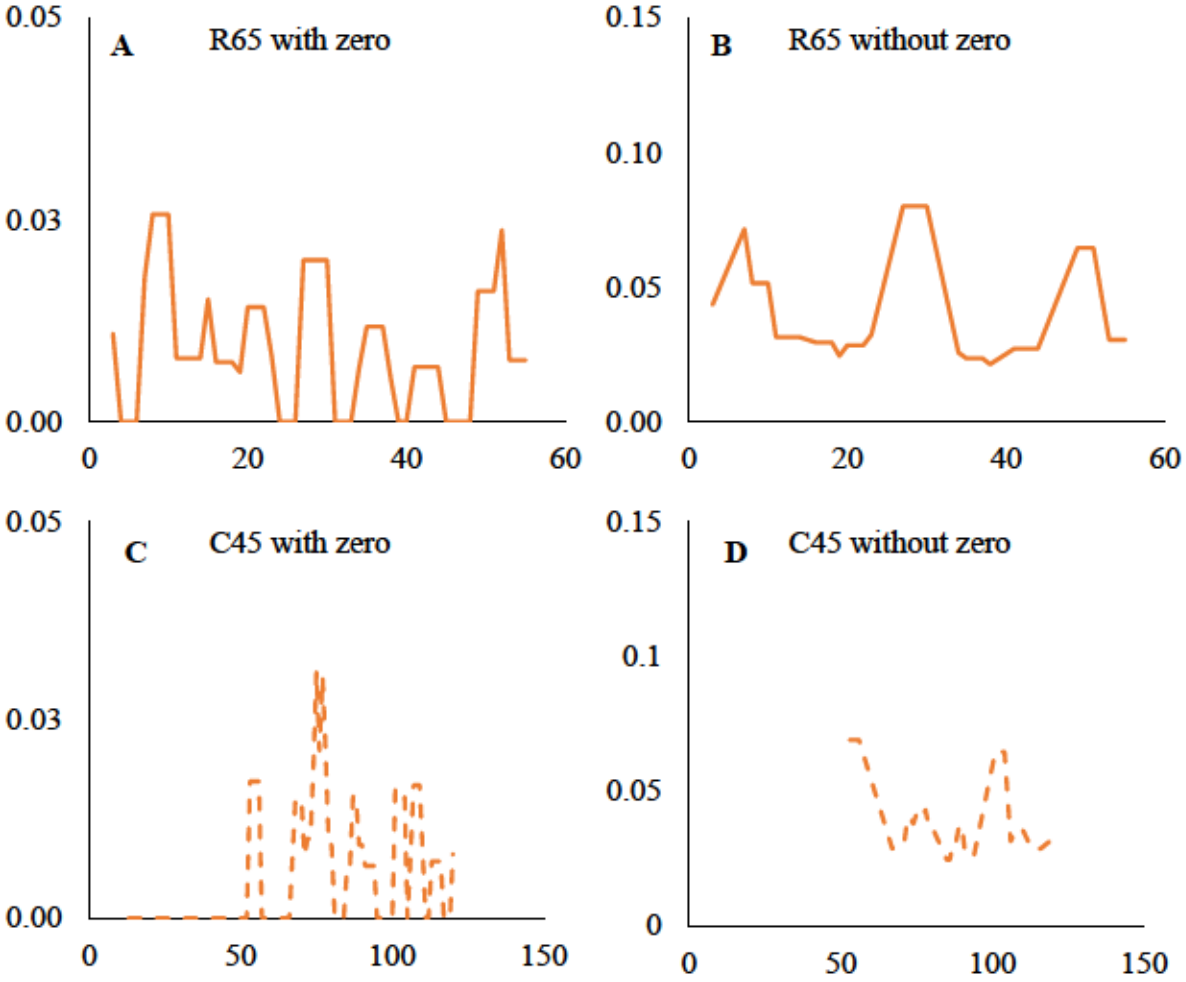


Figure 41. A SL-2 window-28 $^{13}C/^{12}C$ transect R65 with all zero data points included. B SL-2 window-28 $^{13}C/^{12}C$ transect R65 with all zero data points removed. C SL-2 window-28 $^{13}C/^{12}C$ transect C45 with all zero data points included. D SL-2 window-28 $^{13}C/^{12}C$ transect C45 with all zero data points removed. Plots A and B show that the 4$^{th}$ order moving average polylines calculated by Microsoft Excel artificially increase the SI. While plots C and D show that moving average calculations shift data due to zero values in the dataset.

$^{13}C/^{12}C$ characterization. Transects in window-2 show each case of intersection. For horizontal transects, each one starts at a different SI and exhibits a different habit. For R64, the transect displays two orthogonal intersections before showing sinusoidal behavior for the remainder of the transect (Figure 42). R128 starts with a series of orthogonal and acute intersections then transitions to sinusoidal from pixel 180 to 255 (Figure 42). R192 starts with two orthogonal intersects and is then sinusoidal from pixel 90 to 255. (Figure 42). The vertical transects also show different starting SI and habits. C64 is a series of orthogonal and acute intersects before transitioning to an acute intersect from pixel 220 to 240 (Figure 42). C128 starts with an acute intersect then sinusoidal from pixel 77 to 195 and ends with two orthogonal intersect (Figure 42). C192 is exclusively sinusoidal (Figure 42). Transition boundaries defined for all transects where then plotted on the $^{13}C/^{12}C$ SI element map for window-2 (Figure 43). Transects appear to have either complex correlation or none. Each row transects start with orthogonal boundaries near the same pixel. While some orthogonal boundaries do match past the first boundary (Figure 43, R64 and R128), other boundaries between pairs of orthogonal boundaries do not match (Figure 43, R64 and R192). Column transects have a similar correlation as horizontal. C64 and C128 share some similarities with orthogonal boundaries near R192 (Figure 43, C64 and C128). R192 and C192 share few characteristics to other transects within their group.

$^{13}C/^{12}C$ discussion. Usage of non-zero $^{13}C/^{12}C$ SI moving average calculations suggests that characterizations for AR window-2 are skewed. However, the dataset with zero points and the larger transects used have no small-scale systematic changes. Instead window-2 with zeros has non-continuous regions of high $^{13}C$ SI separated by zero SI. The lack of a metric to define zones within the zero $^{13}C/^{12}C$ transects suggests the use of the non-zero dataset for

characterizations is more effective. The element map including transect case boundaries (Figure 43) shows the difficulty associated with defining boundaries for large datasets. With minor correlation between transects, full window chemical characterizations would require more tightly spaced transects and an algorithm to calculate boundaries within transects. Ideally, calculated SI isopleths for the entire $^{13}C/^{12}C$ map would be the easiest method to group regions by SI across an entire window. Such calculations can be done in ArcMap by using element maps as point clouds and running Triangulated Irregular Network (TIN) software to generate a false topology image. From this TIN generated surface, topography lines can be calculated to connect regions in the TIN with the same SI.

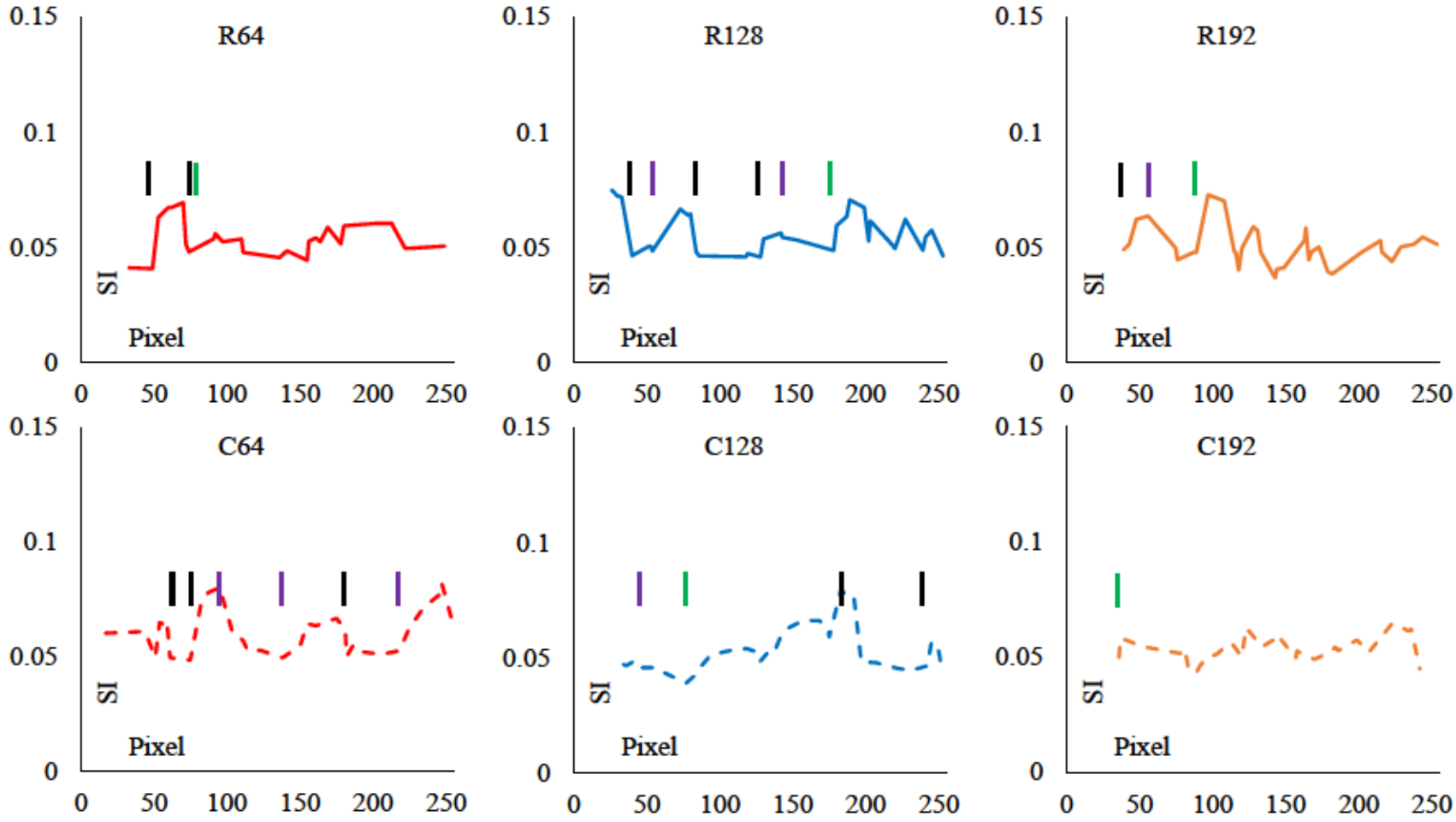


Figure 42. Diamond AR window-2 $^{13}C/^{12}C$ 4$^{th}$ order moving average polyline transects. Plot titles refer to each transects location on the element map with R being row and C being column transects. Y-axis is Signal Intensity (SI). Colored bars represent the different intercept cases identified in this study. Each vertical bar marks a new intercept. Black bars are orthogonal intercepts. Purple bars are acute intercepts. Green bars are sinusoidal intercepts.

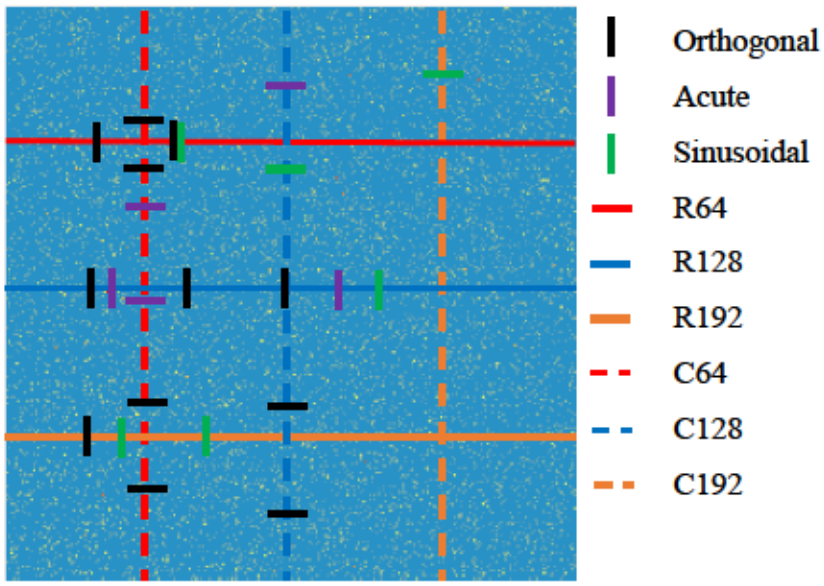


Figure 43. Diamond AR window-2 $^{13}C/^{12}C$ element map with zero data points. Element map SI color are that lower values are blue and higher values are yellow/red. Six transects of element map including each intersection cases for each transect identified in Figure 42.

# CONCLUSIONS

Diamond geochemistry is the primer analyte for determining fluxes in the sublithospheric mantle and deep mantle. Geochemical systems used in diamond studies include stable isotopes, radiogenic isotopes and trace element ratios. These studies are able to determine the contiguous mantle of crystalizing diamond, ages of growth zones and chemical fluxes through geologic time (Van Rythoven, 2012; Harte, 2010; Shirey and Richardson, 2011; Timmerman et al., 2017). Diamonds that have their histories characterized can then be used to determine mantle geochemical history across cratons (Schulze et al., 2008; Shirey and Richardson, 2011). This process is hindered by the availability of laboratories capable of high analytical and spatial resolution in-situ methodologies. Our study sought to test if the Time-of-Flight SIMS (ToF-SIMS) platform is a viable option for these types of studies. With two analyses of ToF-SIMS in the same analysis window able to characterize the entire periodic table for pixels of 2 $\mu m^2$, ToF-SIMS would dramatically reduce methodology difficulty, analytical time and improve availability of these studies.

I tested the viability of ToF-SIMS in two ways. First, through SI conversions, can ToF-SIMS analyses replicate known $\delta^{13}C$ values? Second, by ToF-SIMS element mapping, can I determine systematic chemical variations? SI conversion included calculation of $\delta^{13}C$ values using SI of analysis windows for three calcite and two diamond crystals using an internal standard of calcite. Element map chemical characterizations included defining variations in $^{12}C$, $^{13}C/^{12}C$ and $^{16}O$ transects. Results of our tests led us to conclude that ToF-SIMS with our experimental design is unable to replicate known $\delta^{13}C$ values. Without a control group, our chemical characterizations would require an established imaging technique to determine

accuracy. Necessary changes to our experimental methodologies to address these problems follow.

**Signal Intensity Conversion**

Isotope Ratio Mass Spectrometry (IRMS) of eleven calcite drill bores of the Magnet Cove carbonatite defined carbon and oxygen stable isotope variation (Table 1). These analyses were done in order to establish an internal standard $^{13}C/^{12}C$ ratio for use in converting ToF-SIMS SI into $\delta^{13}C$ values. Calculations were presented for three calcite crystals, SL-1 and AR (Table 2). These calculated $\delta^{13}C$ values for SI from analysis windows (Table 2) resulted in significant errors when comparing calcite crystals to IRMS data and SL-1 and AR to prior published data (Table 1; Van Rythoven, 2012; McCandless et al., 1991; Cartigny et al., 2009).

Recommended improvements to our analytical methods are extensive. This study recommends: using diamond of known isotopic variation as the internal standard for unknown diamonds; factoring what, if any, effect isotopic composition has on ionization efficiency in ToF-SIMS; gaining access to Automated eXpert Spectral Image Analysis (AXSIA) or a multivariate statistical software package designed for element map concatenating and spectral peak separations. Establishing an internal standard with a crystal structure as similar as possible to an unknown crystal will mitigate skew caused by the matrix effect (Stephan, 2001). While an analytical chemistry analysis of ionization potential for $^{13}C$ vs $^{12}C$ in a ToF-SIMS environment would determine what correction factors need to be applied to each isotopes SI to increase analytical precision. Use of a multivariate statistical package would allow users to efficiently implement the wealth of data generated by ToF-SIMS analyses and correcting for same atomic mass unit species (Stephan, 2001; Smentkowski et al., 2005). This study nominally generated

eleven ion species for every anion analysis and thirteen ion species in cation analysis. A dataset of this size being generated for every analysis window severely limited how much of the dataset could be analyzed in this study. Thus, a program such as AXSIA generating component maps of concatenated ion species would reduce time significantly and potentially increase significance of chemical characterizations. A program similar to AXSIA would also be able to run spectral peak separation calculations. The generation of $^{12}C^{1}H$ ions due to gases in the vacuum chamber (Stephan, 2001) has two effects on $^{13}C$ SI accuracy. First, by artificially increasing SI of $^{13}C$ by the post processing software adding counts of $^{12}C^{1}H$ to $^{13}C$. Secondly, by incorrectly identifying counts of $^{13}C$ by adding them to the $^{12}C^{1}H$ counts. Peak separation of these ions would be necessary for any high analytical precision stable isotope ToF-SIMS study (Stephan, 2001). Under ideal conditions, peak separation calculations of Teflon were inconsistent in removing the $^{12}C^{1}H$ SI peak from $^{13}C$ (Stephan, 2001).

**Chemical Characterization**

I hypothesized changes in SI of $^{12}C$, $^{13}C/^{12}C$ and $^{16}O$ transects could be used to define chemical zones. Due to each transect containing a large dataset (Figure 3c), I needed to reduce transects to a more manageable format (Figure 3d). Fourth order moving average polylines were selected due to their simplification of the data while keeping similar structure to polynomial trend lines. During our analysis of $^{13}C/^{12}C$ SI, it became clear that for datasets with fewer points, moving average functions would artificially increase the SI (Figure 41a and 41b) and in some cases shift the moving average polyline (Figure 41c and 41d). These effects of reducing the data with Microsoft Excel leads to us concluding that without a control chemical imaging technique to compare, our characterizations of $^{12}C$, $^{13}C/^{12}C$ and $^{16}O$ need to be approached with caution.

The size of our dataset limited how many transects could be made per window. This limitation made characterizations for analysis windows potentially impossible due to the amount of space between transects (Figure 43). To address this, SI isopleth maps of model surfaces for an element map could be used instead of transects. Isopleth maps would use all 65,500 element map data points instead of the 1,530 used for transects. Models could then be used with greater continuity to define chemical zones within analysis windows.

## REFERENCES


Bassett, D., MacLeod, K., Miller, J., and Ethington, R., 2007, Oxygen isotopic composition of biogenic phosphate and the temperature of early ordovician seawater: Palaios, v. 22, p. 98-103.

Bundy, F., 1989, Pressure-temperature phase diagram of elemental carbon: Physica a Statistical Mechanics and its Applications, v. 156, p. 169-178.

Cartigny, P., Farquhar, J., Thomassot, E., Harris, J., Bozwell, W., Masterson, A., McKeegan, K., and Stachel, T., 2009, A mantle origin for Paleoarchean periodtitic diamonds from the panda kimberlite, slave craton: evidence from $^{13}C$-, $^{15}N$- and $^{33,34}S$-stable isotope systematics: Lithos, v. 112S, p. 852-864.

Cartigny, P., 2005, Stable isotopes and the origin of diamond: Elements, v. 1, p. 79-84.

Chacko, T., Cole, D., and Horita, J., 2001, Equilibrium oxygen, hydrogen and carbon isotope fractionation factors applicable to geologic systems: Reviews in Mineralogy and Geochemistry, v. 43, p. 1-81.

Cherniak, D., 2010, Diffusion in carbonates, fluorite, sulfide minerals, and diamond, in Diffusion in Minerals and Melts: Reviews in Mineralogy & Geochemistry, v. 72, p. 871-894.

Clifford, T., 1966, Tectono-metallogenic units and metallogenic provinces of Africa: Earth and Planetary Science, v. 1, p. 421-434.

Dasgupta, R., 2013, Ingassing, storage, and outgassing of terrestrial carbon through geologic time, in Carbon in Earth: Reviews in Mineralogy & Geochemistry, v. 75, p. 109-138.

Davies, R., Griffin, W., Pearson, N., Andrew, A., Doyle, B. and O'Reilly, S., 1999, Diamonds from the deep: pipe DO-27, Slave craton, Canada: International kimberlite Conference, v. 7.

Davies, R., O'Reilly, S., and Griffin, W., 2002, Multiple origins of alluvial diamonds from New South Wales, Australia: Economic Geology, v. 97, p. 109-123.

Davies, R., Griffin, W., O'Reilly, S., and Andrew, A., 2003, Unusual mineral inclusions and carbon isotopes of alluvial diamonds from Bingara, eastern Australia: Lithos, v. 69, p. 51-66.

Deines, P., Gurney, J., and Harris, J., 1984, Associated chemical and carbon isotopic composition variations in diamonds from Finsch and Premier kimberlite South Africa: Geochimica et Cosmochimica Acta, v. 48, p. 325 - 342.

Deines, P., Harris, J., Spear, P., and Gurney, J., 1989, Nitrogen and 13C content of Finsch and Premier diamonds and their implications: Geochimica et Cosmochimica Acta v. 53, p. 1367-1378.

Deines, P., Harris, J., and Gurney, J., 1993, Depth-related carbon-isotope and nitrogen concentration variability in the mantle below the Orapa kimberlite, Botswana, Africa: Geochimica et Cosmochimica Acta, v. 57, p. 2781-2796.

Deines, P., 1980, The carbon isotopic composition of diamonds: relationship to diamond shape, color, occurrence and vapor compositon: Geochimica et Cosmochimica Acta, v. 44, p. 943-961.

Eaton-Magana, S., Breeding, C., and Shigley, J., 2018, Natural-color blue, gray, and violet diamonds: allure of the deep: Gems & Gemology, v. 54, p. 112-131.

Galimov, E., Sobolev, N., Efimova, E., Shiryaev, A., 1999, Carbon isotopic composition of Venezuela diamond: Doklady Akademii Nauk, v. 364, p. 101–106.

Haendel, D., Mühle, K., Nitzsche, H., Stiehl, G., and Wand, U., 1986, Isotopic variations of the fixed nitrogen in metamorphic rocks: Geochimica et Cosmochimica Acta, v. 50, p. 749-758.
Harte, B., 2010, Diamond formation in the deep mantle: the record of mineral inclusions and their distribution in relation to mantle dehydration zones: Mineralogical Magazine, v. 74, p. 189-215.
Hausel, D., 1998, Diamonds and mantle source rocks in the Wyoming craton, with a discussion of other US occurrences: Report of Investigations, v. 53, p. 1-82.
Hazen, R., Downs, R., Kah, L., and Sverjensky, D., 2013, Carbon mineral evolution, in Carbon in Earth: Reviews in Mineralogy & Geochemistry, v. 75, p. 79-97.
Helmstaedt, H., 1993 , Natural diamond occurrences and tectonic setting of primary diamond deposits: Prospectors and Developers Association of Canada, p. 3-74.
Howard, J., and Hanson, W., 2008, Geology of the crater of diamonds state park and Vicinity and Pike county, Arkansas: Arkansas Geological Survey State Park Series, v. 3, p. 1-13.
Jaques, A., Sheraton, J., Hall, A., Smith, C., Sun, S., and Drew, R., 1986, Composition of crystalline inclusions and C-isotopic composition of Argyle and Ellendale diamonds: International Kimberlite Conference: Extended Abstracts, v. 4, p. 426-428.
Kaminsky, F., Zakharchenko, O., Griffin, W., Channer, D., and Khachatryan-Blinova, G., 2000, Diamond from the Guaniamo area, Venezuela: The Canadian Mineralogist, v. 38, p. 1347-1370.
Kaminsky, F., Wirth, R., Matsyuk, S., Schreiber, A., and Thomas, R., 2009, Nyerereite and nahcolite inclusions in diamond: evidence for lower-mantle carbonatitic magmas: Mineral Magazine, v. 73, p. 797–816.
Kaminsky, F., Matzel, J., Jacobsen, B., Hutcheon, I., and Wirth, R., 2015, Isotopic fractionation of oxygen and carbon in decomposed lower-mantle inclusions in diamond: Mineralogy and Petrology, v. 110, p. 379-385.
Kirkley, M., Gurney, J., Otter, M., Hill, S., and Daniels, L., 1991, The application of C-isotope measurements to the identification of the sources of C in diamonds - a review: Applied Geochemistry, v. 6, p. 477–494.
Koeberl, C., Masaitis, G., Gilmour, I., Langenhorst, F., and Schrauder, M., 1997, Diamonds from the Popigai impact strucutre, Russia: Geology, v. 25, p. 967-970.
Koga, K., Van Orman, J., and Walter, M., 2003, Diffusive relaxation of carbon and nitrogen isotope heterogeneity in diamond: a new thermochronometer, Physics of the Earth and Planetary Interiors, v. 139, p. 35-43.
Lensky, N., Niebo, R., Holloway, J., Lyakhovksy, V., and Navon, O., 2006, Bubble nucleation as a trigger for xenolith entrapment in mantle melts: Earth Planet Science Letters, v. 245, p. 278-288.
Logvinova, A., Taylor, L., Fedorova, E., Yelisseyev, A., Wirth, R., Howarth, G., Reutsky, V., and Sobolev, N., 2015, A unique diamondiferous peridotite xenolith from the Udachnaya kimberlite pipe, Yakutia: role of subduction in diamond formation: Geology and Geophysics, v. 56, p. 306-320.
MacKenzie, J., and Canil, D., 1998, Composition and thermal evolution of cratonic mantle beneath the central Archean Slave Province, NWT, Canada: Contributions to Mineralogy and Petrology, v. 134, p. 313-324.
McCandless, T., Waldman, M., and Gurney, J., 1991, Macrodiamonds and microdiamonds from Murfreesboro Lamproites, Arkansas: morphology, mineral inclusions, and carbon isotope geochemistry: International Kimberlite Conference, v. 5, p. 78-97.

McQuarrie, D., and Simon, J., 1997, The harmonic oscillator and the rigid roator: two spectroscopic models: in Physical chemistry a molecular approach, University Science Books, p. 156-189.
Menand, T., and Tait, S., 2001, A phenomenological model for precursor volcanic eruptions: Nature, v. 411, p. 678-680.
Mendelsohn, M., and Milledge, H., 1995, Geologically significant information from routine analysis of the mid-infrared spectra of diamonds: International Geologic Review, v. 37, p. 95-110.
Palot, M., Cartigny, P., and Viljoen, F., 2009, Diamond origin and genesis: A C and N stable isotope study on diamonds from a single eclogitic xenolith (Kaalvallei, South Africa): Lithos, v. 112, p. 758-766.
Richardson, S., Pöml, P., Shirey, S., and Harris, J., 2009, Age and origin of peridotitc diamonds from Venetia, Limpopo belt, kaapvaal-zimbabwe craton: Lithos, v. 112, p. 785-792.
Russell, J., Porritt, L., Lavallée, Y., Dingwell, D., 2012, Kimberlite ascent by assimilation fuelled buoyancy: Nature, v. 481, p. 352-356.
Schertl, H., and Sobolev, N., 2013, The kokchetav massif, Kazakhstan: "Type locality" of diamond-bearing UHP metamorphic rocks: Journal of Asian Earth Sciences, v. 63, p. 5-38.
Schulze, D., Coopersmith, H., Harte, B., and Pizzolato, L., 2008, Mineral inclusions in diamonds from the Kelsey Lake Mine, Colorado, USA: depleted archean mantle beneath the proterozoic Yavapai province: Geochimica et Cosmochimica Acta, v. 72, p. 1685-1695.
Shirey, S., and Richardson, S., 2011, Start of the Wilson cycle at 3 Ga shown by diamonds from subcontinental mantle: Science, v. 333, p. 434-436
Shirey, S., and Shigley, J., 2013, Recent advances in understanding the geology of diamonds: Gems & Gemology, v. 49, no. 4.
Shirey, S., Harris, J., Richardson, S., Fouch, M., James, D., Cartigny, P., Deines, P., and Viljoen, F., 2002, Diamond gensis, seismic structure, and evolution of the kaapvaal-zimbabwe craton: Science, v. 297, p. 1683-1686.
Shirey, S., Cartigny, P., Frost, D., Keshav, S., Nestola, F., Nimis, P., Pearson, D., Sobolev, N., and Walter, M., 2013, Diamonds and the geology of mantle carbon: in Carbon in Earth, Reviews in Mineralogy & Geochemistry, v. 75, p. 355-406.
Siljeström, S., 2011, Single fluid inclusion analysis using ToF-SIMS: Implications for ancient earth biodiversity and paleoenrionment studies [Ph.D. Thesis]: Stockholm, Stockholm University, 29 p.
Smentkowski, V., Keenan, M., Ohlahusen, J., and Kotula, P., 2005, Multivariate statistical analysis of concatenated time-of-flight secondary ion mass spectrometry spectral images. Complete description of the sample with one analysis: Analytical Chemistry, v. 77, p. 1530-1536.
Sobolev, N., Logvinova, A., Efimova, E., 2009, Syngenetic phlogopite inclusions in kimberlite-hosted diamonds: implications for role of volatiles in diamond formation: Russian Geology Geophysics, v. 50, p. 1234-1248.
Sparks, R., 2013, Kimberlite volcanism: Annual review of Earth and Planetary Sciences, v. 41, p. 497-528.
Stachel, T, Brey, G., Harris, J., 2000a, Kankan diamonds (Guinea) I: from the lithosphere down to the transition zone: Contributions to Mineralogy and Petrology, v. 140, p. 1-15.
Stachel, T., Harris, J., Brey, G., and Joswig, W., 2000b, Kankan diamonds (Guinea) II: lower mantle inclusion parageneses: Contributions to Mineralogy and Petrology, v. 140, p. 16-27.

Stachel, T., Brey, G., and Harris, J., 2005, Inclusions in sublithospheric diamonds: Glimpses of deep earth: Elements, v. 1, p. 73-78.
Stachel, T., Harris, J., and Muehlenbachs, K., 2009, Sources of carbon in inclusion bearing diamonds: Lithos, v. 112, p. 625-637.
Stephan, T., 2001, ToF-SIMS in cosmochemistry: Planetary and Space Science, v. 49, p. 859-906.
Stern, R., Leybourne, M., and Tsujimori, T., 2016, Kimberlites and the start of plate tectonics: Geology, v. 44, p. 799-802.
Stern, R., 2009, An introduction to secondary ionization mass spectrometry (SIMS) in geology: Mineralogical Asssociation of Canada Short Course, v. 41, p. 1-18.
Tainton, K., and McKenzie, D., 1994, The generation of kimberlites, lamproites and their source rocks: Journal of Petrology, v. 35, v. 787-817.
Thomassot, E., Cartigny, P., Harris, J., and Viljoen, K., 2007, Methane-related diamond crystallization in the Earth's mantle: Earth and Planetary Science Letters, v. 257, v. 362-371.
Timmerman, S., Koornneef, J., Chinn, I., and Davies, G., 2017, Dated eclogitic diamond growth zones reveal variable recycling of crustal carbon through time: Earth and Planetary Science Letters, v. 463, p. 178-188.
Van Rythoven, A., 2012, Chemical, isotopic, and textural characteristics of diamond crystals and their mineral inclusions from A154 south (Northwest Territories), Lynx (Quebec), and Kelsey Lake (Colorado): Implications for growth histories and different mantle environments [Ph.D. thesis]: Toronto, University of Toronto, 247 p.
Verkouteren, M., and Klinedinst, D., 2004, Value assignment and uncertainty estimation of selected light stable isotope reference materials: RMs 8543-8545, RMs 9562-8564, and RM 8566: National Institute of Standards and Technology Special Publication, v. 260-149, p. 1-58.
Viljoen, K., Dobbe, R., Smit, B., Thomassot, E., and Cartigny, P., 2004, Petrology and geochemistry lherzolite from the premier diamond mine, South Africa: Lithos, v. 77, p. 539-552.
Walter, M., Kohn, S., Araujo, D., Bulanova, G., Smith, C., Gaillou, E., Wang, J., Steele, A., and Shirey, S., 2011, Deep mantle cycling of oceanic crust: Evidence from diamonds and their mineral inclusions: Science, v. 334, p. 54-57.
Wilson, L., and Head, J., 2007, An integrated model of kimberlite ascent and eruption: Nature, v. 447, p. 53-57.
Yuan, L., Dasgupta, R., Tsuno, K., Monteleone, B., and Shimizu, N., 2016, Carbon and sulfur budget of the silicate earth explained by accretion of differentiated planetary embryos: Nature Geoscience, v. 9, p. 781-785.